Luminescence Spectroscopy of Quantum Cutting Phosphors

Materials, Measurements and Mechanisms

Cover photograph taken by the author. Layout AV-dienst Chemie.

LUMINESCENCE SPECTROSCOPY OF QUANTUM CUTTING PHOSPHORS

MATERIALS, MEASUREMENTS AND MECHANISMS

LUMINESCENTIESPECTROSCOPIE VAN KWANTUMKNIPPENDE FOSFOREN MATERIALEN, METINGEN EN MECHANISMEN

(met een samenvatting in het Nederlands)

PROEFSCHRIFT

ter verkrijging van de graad van doctor aan de Universiteit Utrecht op gezag van de Rector Magnificus, prof. dr. W. H. Gispen, ingevolge het besluit van het College voor Promoties in het openbaar te verdedigen op maandag 7 november 2005 des middags te 16.15 uur

door

PETER VERGEER

geboren op 17 december 1976, te Leiden

Promotor: prof. dr. A. Meijerink

Debye Instituut
Universiteit Utrecht

The work described in this thesis was supported by the Technology Foundation STW, applied science division of NWO and the technology programme of the Ministry of Economic Affairs.

"I see your true colors
Shining through
I see your true colors
And that's why I love you
So don't be afraid to let them show
Your true colors
True colors are beautiful,
Like a rainbow"

-Cyndi Lauper

CIP-GEGEVENS KONINKLIJKE BIBLIOTHEEK, DEN HAAG

Vergeer, Peter

Luminescence Spectroscopy of Quantum Cutting Phosphors – Materials, Measurements and Mechanisms
(Luminescentiespectroscopie van Kwantumknippende Fosforen – Materialen, Metingen en Mechanismen)
Peter Vergeer. - Utrecht: Universiteit Utrecht, Faculteit Bètawetenschappen, Departement Scheikunde, Debye Instituut, Condensed Matter and Interfaces.
Proefschrift Universiteit Utrecht. Met samenvatting in het Nederlands.
ISBN 90-393-4052-8

Contents

Chapter 1

Introduction

Many lanthanides show efficient visible luminescence. This property has resulted in the extensive use of lanthanide ions in luminescent materials for color displays and fluorescent tubes. Fundamental research is the basis to explain and exploit the luminescence properties of lanthanide ions and this topic remains a challenging subject for many researchers. This thesis is focussed on research involving the conversion of one high-energy photon into two lower-energy (visible) photons, a process called 'quantum cutting', with the use of lanthanide ions. In this chapter an introduction to lanthanide luminescence is given, followed by a description of basic processes, like absorption and emission of radiation and energy transfer, which are important for finding and understanding quantum cutting. The introduction ends with a summary of the thesis.

1.1 Introduction

The first report on artificial luminescence was in 1669 due to an accidental discovery by the German alchemist Hennig Brand. In his quest to transform distilled salts from urine into gold he encountered a white powder that glowed 'spontaneously' in the dark. For this reason he called the compound "phosphorus" (Greek for "light bearer"). Nowadays we know that the glowing powder was elementary white phosphor, that was oxidized to phosphorus pentoxide under the emission of light. Nevertheless, luminescent materials that convert high energy radiation into visible light are called phosphors, even though they mostly do not contain the element phosphorus. The general term luminescence is nowadays used for the process where energy is converted into visible light by 'cold'* materials.

From a luminescence researchers' point of view, an important row of elements in the periodic system is the $4f$-block, where the lanthanides (atomic number 57 to 71) reside. Most of these elements show efficient luminescence and are generally used in applications related to light and lighting (e.g. fluorescent tubes, displays, X-ray imaging and lasers).

1.2 Applications of lanthanides

The two most common applications for luminescent materials are light generation in fluorescent tubes and in cathode ray tubes. In both devices, phosphors convert (invisible) radiation into visible light. A schematic layout of a mercury-discharge fluorescent tube is shown in figure 1.1. Accelerated electrons, emitted at the cathodes at the ends of the tube, collide with Hg atoms to create an excited Hg plasma (Hg^* in figure 1.1). The excited Hg atoms return to the ground state under emission of ultraviolet (UV) radiation of 254 nm. The phosphor coating at the inner wall of the tube converts the 254 nm photons into visible light.

Modern fluorescent lamps are based on the tricolor principle, in which UV radiation is converted into blue, green and red light. For blue, $BaMgAl_{10}O_{17}$ doped with Eu^{2+} is used, which gives emission around 450 nm. For green light, $LaPO_4$:Ce^{3+}, Tb^{3+} is commonly used. Ce^{3+} ions absorb the UV light and transfer the excitation energy to the Tb^{3+} ions which subsequently emit green light at mainly 545 nm. For red, Y_2O_3 doped with Eu^{3+} is used. This phosphor has its strongest emission at 611 nm. For humans, this particular combination of colors is perceived as white light. Other combinations of colors, for example the combination of blue and yellow light, are also perceived as white. However, this particular combination of three colors

*This is in contrast to 'black body radiators' [1] like the sun or a light bulb, that radiate visible light because they have elevated temperatures. Luminescence can therefore be regarded as 'cold' light. One can safely touch a working fluorescent tube, but it is recommended to wear gloves when you touch a glowing light bulb.

has the advantage that it combines a good eye sensitivity with a high color rendering index.

Mercury-discharge fluorescent tubes have been operational since before the 2nd world war and the technology has developed to a very mature status. In comparison with other applied white light sources, a fluorescent tube has the highest energy efficiency. A practical equation to analyze the energy efficiency is [2],

$$\eta_{\text{lamp}} = \eta_{\text{discharge}} \frac{\lambda_{\text{UV}}}{\lambda_{\text{VIS}}} QE. \tag{1.1}$$

Equation (1.1) splits the energy efficiency of the lamp (η_{lamp}) into three factors. The first one ($\eta_{\text{discharge}}$) is the conversion efficiency from electric energy to UV radiation in the plasma. Mercury is generally used as the discharge medium since it has the highest known discharge efficiency (75%). The second term, the fraction ($\frac{\lambda_{\text{UV}}}{\lambda_{\text{VIS}}}$) gives the energy loss due to the conversion of UV photons into visible photons. The 254 nm photons generated by the mercury discharge are converted by the phosphors into visible photons with an average wavelength of about 500 nm. Therefore, this factor reduces the energy efficiency by 50%. The last factor (the quantum efficiency, QE) is the ratio of visible photons that are emitted by the phosphors compared to the amount of UV photons that are absorbed. (It is assumed that all the UV light is absorbed by the phosphors.) The commercially used phosphors show efficient absorption and the quantum efficiency is about 90%. The 10% of UV radiation that is lost, is not converted into visible light but into heat. The overall energy (to light) efficiency of a fluorescent tube is therefore about 30%. As a comparison, the energy efficiency of an incandescent lamp is between 2 and 5%.

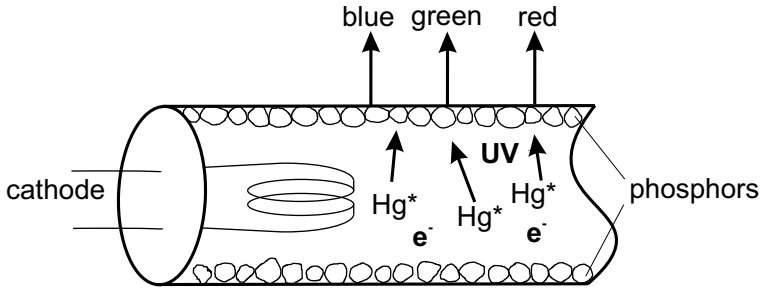

Figure 1.1: Schematic of a tricolor mercury-discharge fluorescent tube.

The other widespread application for lanthanides is light generation in displays. In the display market there is a shift from the 'bulky' cathode ray tube (CRT) televisions to the more modern flat panel displays.

The CRT televisions use the large extension behind the screen to generate and focus a beam of fast electrons to a specific point on the television screen. The inner side of the screen is coated with three different phosphors that generate blue, green

or red light. Depending on the position where the electron beam hits the phosphor layer, one of the three colors is generated. By rapid scanning of the electron beam, a picture is formed.

For flat panel displays multiple concepts are used. For monitors that require a small pixel size (such as computer monitors) liquid crystal technology is most commonly used. For larger displays, starting from about 100 cm diameter, pixel sizes can be larger and plasma technology becomes competitive due to smaller losses of energy at the surface of the plasma cell. A plasma display panel (PDP) consists of a matrix of cells filled with Xe gas and coated with phosphors (see figure 1.2). Each cell is a color-point on the screen, which can be addressed individually. When a voltage is applied over the cell, the Xe plasma discharge generates vacuum-ultraviolet (VUV, $\lambda < 200$ nm) radiation which is converted by the phosphor into green, red or blue light.

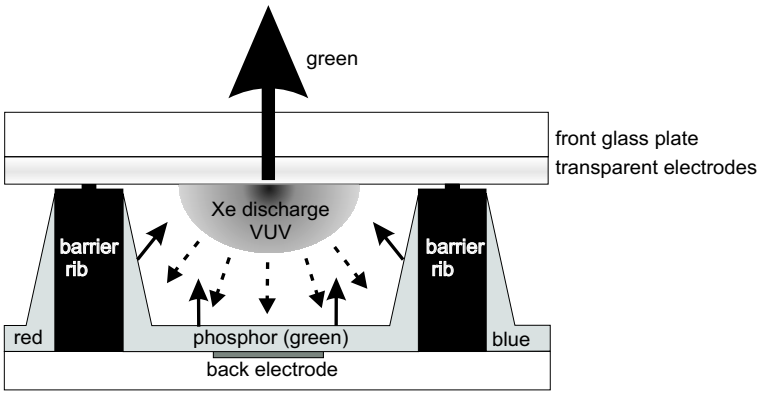

Figure 1.2: Schematic of a green color-point in a plasma display panel.

1.3 Spectral properties of lanthanides

Research on the luminescence of lanthanide-doped materials has developed during the last century. It started in 1908 when Becquerel observed characteristic sharp absorption lines when measuring spectra of lanthanide salts at low temperature [3]. The origin of the sharp lines was elucidated with the development of the atomic model, around 1930 by Becquerel, Bethe and Kramers [4–6]. The lines were attributed to transitions within the 4f shell (4f→4f transitions), which is partially filled for the lanthanide ions. The electrons in the 4f shell are shielded from the surroundings by the electrons in the filled 5s and 5p shells. This explains the sharpness of the transitions and the weak influence of the surroundings on the energy of the 4f→4f transitions. However, there was an unsolved problem: since 4f→4f transitions are intraconfigurational transitions, they are forbidden as electric dipole transitions (no

change in electric dipole moment) and should therefore be much weaker than observed. Van Vleck *et al.* explained this mystery in 1937 [7]: $4f^n$ states have small contributions from opposite parity states, like $4f^{n-1}5d$ or charge-transfer states, resulting in a small change in dipole moment during the transition. 5d states can mix with 4f states due to odd-parity crystal field components. Crystal-field theory is also the basis for the Judd-Ofelt theory [8,9], for the calculation of the intensities of 4f→4f transitions.

The first systematic experimental study of the 4f→4f transitions of the lanthanides in the infrared (IR), visible (VIS), and UV was published by coworkers of Dieke in the 50's and 60's. It resulted in an overview [10,11] of all the measured energy levels of the trivalent lanthanide ions (Ln^{3+}) doped into $LaCl_3$ up to 250 nm. The so-called Dieke diagrams (see figure 1.3) are often used as a reference for energy levels of lanthanide ions, regardless of the host lattice, since the energetic locations of the 4f energy levels of the lanthanides are hardly changed by the environment.

For a long time, no systematic effort was made to extend the Dieke diagrams to higher energies (shorter wavelengths). The absence of research activity in this area was due to a lack of commercial interest in energy levels at higher energies, and due to the absence of intense tunable excitation sources for shorter wavelengths. This situation changed during the last decade. New (future) applications such as plasma display panels and mercury free fluorescent tubes require phosphors that are suitable for excitation around 172 nm, the emission of a Xe discharge. In addition, the development of synchrotron radiation facilities has provided the intense VUV radiation sources needed for the new research area. Recently, using synchrotron radiation, Wegh *et al.* [12] have expanded the Dieke diagrams up to 68 000 cm^{-1} (included in figure 1.3).

The availability of strong VUV sources also stimulated research on $4f^n \rightarrow 4f^{n-1}5d$ (4f→5d) transitions [13–18]. These transitions are located at relatively high energies, extending deep into the VUV. Contrary to 4f→4f transitions they are parity allowed. Furthermore, since 5d electrons are outer-shell electrons they participate in the chemical bond. As a consequence, the absorption spectra show broad features of high intensity instead of the narrow weak lines characteristic for 4f→4f transitions. For 5d→4f emissions, a red shift (or Stokes shift) is observed compared to the absorption bands. This is due to vibrational relaxation.

The availability of high resolution 4f→5d excitation spectra and modern computer technology has resulted in an increased understanding of the interactions that determine the $4f^{n-1}5d$ energy-level structure of the lanthanide ions. A model [14,15] has been developed to explain the location of $4f^{n-1}5d$ energy levels and the transition rates between the $4f^n$ and $4f^{n-1}5d$ levels. The model is based on a parameterized Hamiltonian that describes the electronic interactions (Coulomb, spin-orbit and crystal-field interactions) as perturbations to the Hamiltonian for hydrogenic wave functions. The Hamiltonian acts on a basis set of orthonormal wave functions which are characterized by $^{2S+1}L_J$ term symbols. The Coulomb and spin-orbit interactions

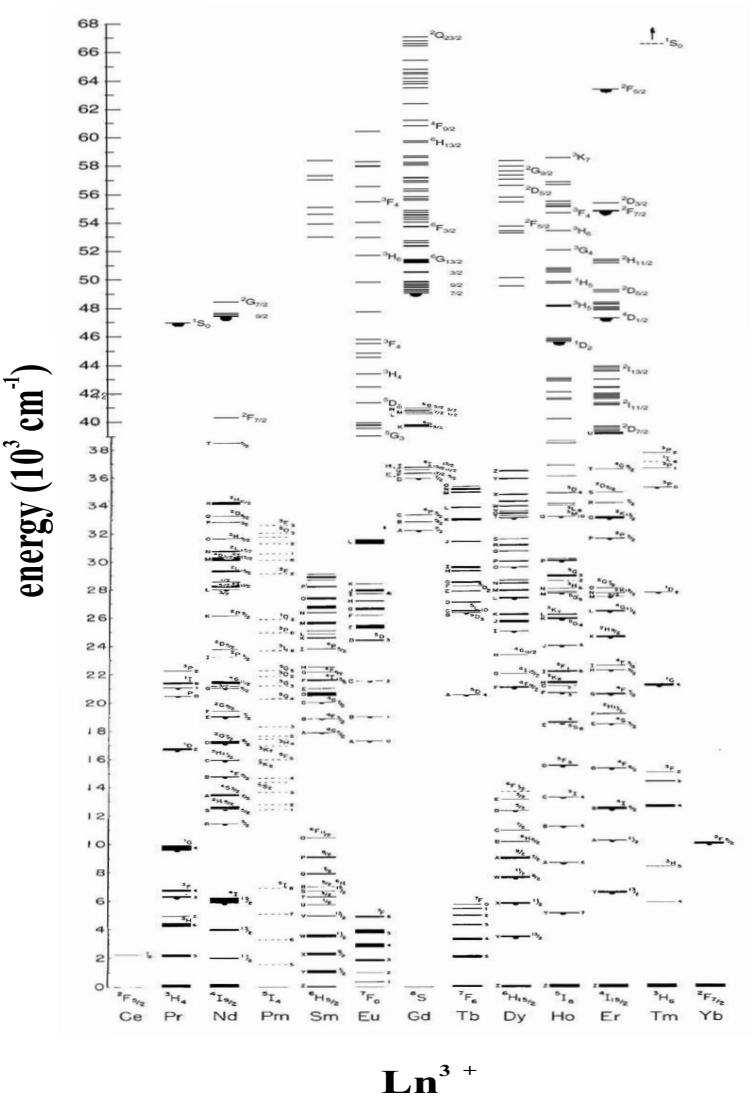

Figure 1.3: The Dieke diagrams including the extensions by Wegh *et al.* [12] (from 40 000 cm^{-1} up): an overview of the experimentally determined 4f→4f transitions of the trivalent lanthanide ions (Ln^{3+}).

act on the diagonal matrix elements only, while the crystal-field interaction parameters act on off-diagonal matrix elements. Diagonalization of the matrix yields the energies and the constitution of the crystal-field mixed orbitals. The constitution of the mixed orbitals determines the transition probabilities.

In addition, a start has been made with *ab initio* calculations. In these methods the molecular orbitals of the lanthanide and ligand wave functions are used, instead

of a crystal field perturbation theory. For Pr^{3+} in a number of model ligand clusters, the trends in transition energies and oscillator strengths are in line with experimental results [19].

1.4 Quantum cutting

As was mentioned above, in fluorescent lamps mercury is used for its high discharge efficiency. Unfortunately, the use of mercury has some serious drawbacks. First, mercury is toxic and it bio-accumulates [20]. Therefore the use of mercury should be minimized. Second, mercury is liquid at room temperature [21], while mercury vapor is needed for fluorescent lighting. Thus, it takes a few seconds to evaporate the mercury after the tube is turned on. This prevents the use of mercury fluorescent tubes in fast-responsive devices, for instance in the break lights of our cars.

The reduction of mercury is a big issue for lamp manufacturers. The three main manufacturers of fluorescent tubes (General Electric, Osram, and Philips) even joined forces in the ALITE (advanced lighting technology) program, a cooperation between industry and universities to find alternative discharge media with a high efficiency.

One of the more promising alternative discharge media is a Xe plasma. The highest reported discharge efficiency of 65% [22] approaches the value for the Hg discharge efficiency (75%). In the Xe plasma, VUV radiation with a wavelength of 147 nm and a broad band around 172 nm is generated in a ratio that depends on the Xe-pressure. The much shorter wavelength compared to the 254 nm of the mercury discharge leads to a lower value of (η_{lamp}) in equation (1.1), because the value of $\frac{\lambda_{\text{UV}}}{\lambda_{\text{VIS}}}$ is ~ 0.33 compared to ~ 0.5 for the mercury discharge. Following equation (1.1), the only possibility to compensate for the lower values for $\eta_{\text{discharge}}$ and $\frac{\lambda_{\text{UV}}}{\lambda_{\text{VIS}}}$ is by the use of phosphors with a quantum efficiency larger than one. This means that the phosphor materials should be able to transform the energy of one absorbed photon into two (or more) emitted photons, so-called quantum cutting. Not only the energy efficiency of Xe fluorescent tubes would increase by application of these phosphors; the energy efficiency of PDP's can be improved as well since these also rely on a Xe discharge as excitation source.

Apart from the industrial motivation, the creation of phosphors with a quantum efficiency larger than one also forms an interesting scientific challenge, since quantum cutters are a new class of materials. The possibility of creating phosphors with a quantum efficiency larger than one is the main topic of this thesis.

1.4.1 Concepts for quantum cutting

In theory, quantum cutting can be realized by a single luminescent center or a combination of luminescent centers. Three different concepts are illustrated in figure 1.4.

The first concept is based on one luminescent center with three energy levels. After a transition of the center to the highest energy level by absorption of one high-energy photon, a sequence of two emissions takes place. This sequence is depicted in figure 1.4. The intermediate level is shortly populated before the luminescent center returns to its ground state.

The second concept involves two luminescent centers. The two centers each play a role in the quantum-cutting process. The starting configuration in figure 1.4 is reached after absorption of light by the center with three energy levels. Then, part of the energy is transferred to the second center. In this non-radiative energy-transfer process the first center acts as a donor of energy while the second center acts as an acceptor of energy. Since the total amount of energy is unchanged in the energy-transfer process, the transitions of the donor and the acceptor that are involved must have the same frequency. This is known as the energy resonance condition for energy transfer. After energy transfer has occurred both centers can emit a (visible) photon.

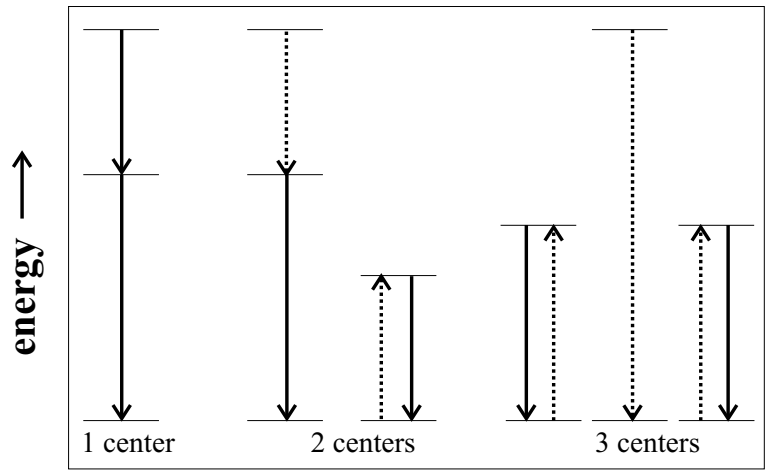

Figure 1.4: Three possibilities to obtain emission of 2 photons after absorption of 1 photon. Electronic states (or energy levels) are denoted by horizontal lines. Radiative emission is depicted by solid lines. Non-radiative energy transfer is depicted by broken lines. Note that during energy transfer the amount of energy is conserved.

The third possibility to obtain quantum cutting is non-radiative energy transfer of the excitation energy of the donor to two acceptors simultaneously, so-called co-operative energy transfer. Here, all centers are depicted as two-level systems again. In this case, the energy resonance condition implies that the sum of the transition frequencies of the two acceptors should match the transition frequency of the donor.

1.4.2 Quantum-cutting phosphors

To emit two visible photons, the photons from the excitation source must have a minimum amount of energy. Since the visible spectrum ranges from roughly 400 to 700 nm, in theory the UV light of the mercury discharge (254 nm) would suffice to create two green photons (2×550 nm) or one red (610 nm) and one blue (450 nm) photon. In practice, non-radiative relaxation results in energy losses (generation of heat) after absorption and makes the generation of two visible photons impossible for 254 nm UV excitation. VUV excitation sources (such as a Xe plasma) are needed to obtain quantum cutting.

At present, three quantum-cutting phosphors are known. One is based on the Pr^{3+} ion [23, 24] and is an example of the single center scheme in figure 1.4. It requires excitation wavelengths of 200 nm or shorter to populate the $^1S_0$ level around 210 nm. From the $^1S_0$ level a cascade emission of 405 nm for the $^1S_0 \rightarrow {}^1I_6$ transition followed by radiation of 480 nm for the $^3P_0 \rightarrow {}^3H_4$ transition or of 610 nm for the $^3P_0 \rightarrow {}^3H_6$ transition is possible. Unfortunately, the color rendering of 405 nm radiation is low which prevents use in commercial applications. The highest quantum efficiency (including the 405 nm radiation) reported is 161% for Pr^{3+} doped in LuF_3 [25].

The other two phosphors are based on energy transfer between two centers. Both consist of a $LiGdF_4$ host lattice, wherein the excitation energy is transported over the Gd^{3+} sublattice. When Eu^{3+} is incorporated as a dopant ion, red photons are obtained for every VUV photon absorbed with a quantum efficiency of 190% [26]. The minimum energy of the excitation photons corresponds to a wavelength of ~ 200 nm to populate the $^6G_{7/2}$ level of Gd^{3+}. This is the starting level for a two-step energy transfer process. In each step energy is transferred to a Eu^{3+} ion by two-center energy transfer, leading to (almost) two excited Eu^{3+} ions and 190% quantum efficiency. The main problem preventing application of this material is the low absorption strength of the Gd^{3+} ions in the VUV. In the second material Tb^{3+} and Er^{3+} are used as dopant ions [27] in the $LiGdF_4$ host lattice. The minimum energy required to obtain good absorption corresponds to 155 nm, which is the edge of the $4f^{10}5d$ excitation band of Er^{3+}. The quantum efficiency is rather low for a quantum-cutting phosphor (130% maximum).

1.5 Theory on electronic transitions and relation to experiments

In the previous section three different concepts for quantum cutting were introduced. They were all described by a number of consecutive steps, of which the most important ones are: absorption of radiation, non-radiative energy transfer, and emission of radiation. In this section it will be shown that there is a large similarity in the physical processes behind these elementary steps. Furthermore, equations for

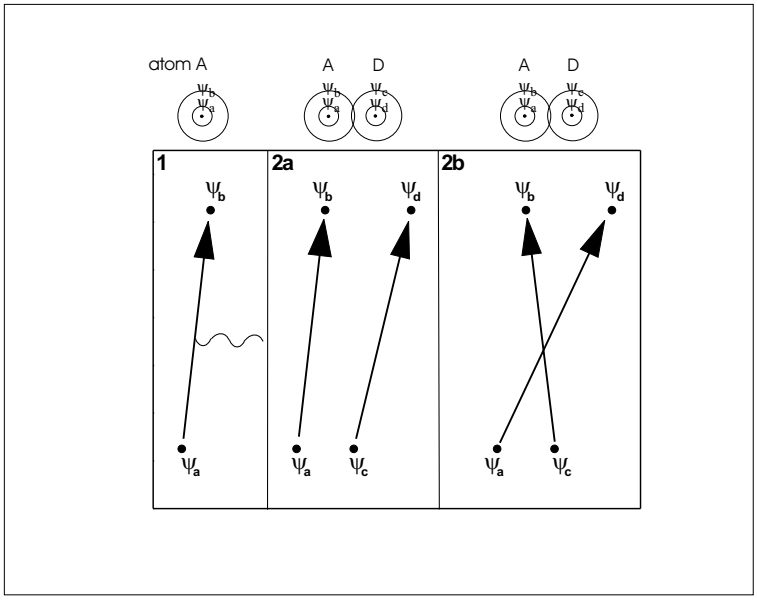

Figure 1.5: Schematics of transitions of electrons from one state to the other. Arrows denote a transition of an electron. The sinusoidal denotes radiation. Top: one or two atoms (A and D) with each two stationary states. States ψ_{a} and ψ_{b} are centered on atom A, ψ_{c} and ψ_{d} are centered on atom D.

the rate of absorption, emission, and energy transfer will be introduced.

Figure 1.5 shows the elementary steps. The top of this figure shows atoms A and D with each one electron and two stationary states, denoted by ψ_{a} to ψ_{d}. The diagram shows transitions of an electron from one state to the other. The left diagram shows a transition of an electron from state ψ_{a} to state ψ_{b} accompanied by emission or absorption of radiation. The diagrams 2a and 2b show simultaneous transitions of two electrons. The initial state of the electrons is one in ψ_{a} and one is ψ_{c}. The final state of the electrons is one in ψ_{b} and one in state ψ_{d}. Conservation of energy implies that $E(\psi_{\mathrm{a}}) + E(\psi_{\mathrm{c}}) = E(\psi_{\mathrm{b}}) + E(\psi_{\mathrm{d}})$. Therefore, by the transition of states of the electrons, energy is transferred between atom A and atom D.

Equations that give the transition rate (γ, units s^{-1}) for the transitions in diagram 1 and diagram 2a show a large degree of similarity. For absorption and emission of randomly polarized radiation (diagram 1.5.1) and electric-dipole allowed transitions the following equations can be derived [28],

$$\gamma_A \;=\; \frac{2\pi}{3\epsilon\epsilon_0\hbar^2}\vec{\mu}_{ab}^2 i(\omega) \tag{1.2a}$$

$$\gamma_{em} \;=\; \frac{2\pi}{3\epsilon\epsilon_0\hbar^2}\vec{\mu}_{ab}^2 (i(\omega) \;+\; \frac{\hbar n^3\omega^3}{2\pi^2c^3}) \tag{1.2b}$$

Equation (1.2a) gives the transition rate for absorption and equation (1.2b) gives the transition rate for emission of radiation. The symbols ϵ, ϵ_0, $\hbar$, ω, n, and c have their usual meaning. Both rates depend on the transition dipole moment $\vec{\mu}_{ab}$ between state ψ_a and ψ_b. The transition dipole moment between states ψ_a and ψ_b is defined as,

$$\vec{\mu}_{ab} \;=\; -e\int \psi_a\vec{r}\psi_b \mathrm{d}V, \tag{1.3}$$

where the integral is over all space V. The quantity $i(\omega)$ is the energy density of electromagnetic radiation with the frequency of the transition (units Js/m^3). Both the rate of absorption and the rate of emission are therefore linearly dependent on the intensity of the radiation from an external field. However, the rate of emission is enhanced by an extra factor, $\frac{\hbar n^3\omega^3}{2\pi^2c^3}$. This factor is the zero-point radiation energy density of vacuum, which existence is a manifestation of the Heisenberg uncertainty relation. Therefore, in the absence of external radiation an atom in an excited state will still decay to the ground state. The accompanying radiation is called spontaneous emission, while the radiation which is induced by an external field is called stimulated emission. For most luminescence experiments with a broad-band light source spontaneous decay is dominant. Stimulated emission is encountered in devices that use scattering to enhance the light intensity such as lasers.

For energy transfer processes that proceed according to diagram 1.5.2a the Coulomb interaction between the electrons is important. This interaction can be expanded in a $\frac{1}{R^n}$ series with n being an integer [28]. The first term in this expansion leads to an interaction between the two transition dipole moments. The rate for dipole-dipole energy transfer (γ_{dd}) can be written as [29],

$$\gamma_{dd} \;=\; \frac{4\pi}{\hbar^2}\Big(\frac{\vec{\mu}_A\cdot\vec{\mu}_D}{4\pi\epsilon\epsilon_0 R^3}\Big)^2 \int g_A(\omega)g_D(\omega)\mathrm{d}\omega. \tag{1.4}$$

The distance between both atoms is denoted by R. This energy transfer rate is characterized by a $\frac{1}{R^6}$ dependence on the distance between the atoms. The use of this equation is widespread. For example, in wet chemical and biological studies the typical $\frac{1}{R^6}$ dependence on the distance is used to probe distances by the use of fluorescent tags that show dipole-dipole energy transfer. [30] Dipole-dipole energy transfer is also known as FRET (fluorescent resonance energy transfer) or Förster energy transfer.

The integral in equation (1.4) is known as the spectral overlap integral. The quantity $g(\omega)$ is the lineshape function and expresses the fact that transitions are not

infinitely sharp but are spread out over a range in frequency, while energy transfer must occur resonantly. Figure 1.6 gives a visual representation of the lineshape functions and the spectral overlap integral.

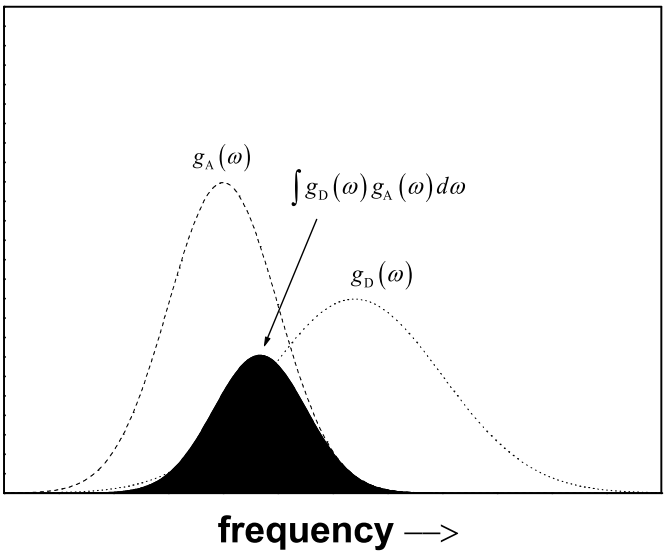

Figure 1.6: This diagram shows two hypothetical lineshape functions and their spectral overlap integral. The function g_D gives the lineshape function of the donor, g_A is the lineshape function of the acceptor. The colored surface is the spectral overlap integral $\int g_D(\omega) g_A(\omega) \mathrm{d}\omega$.

In equation (1.4) the dipole-dipole energy transfer rate depends on the transition dipole moments of both atoms. Since transition dipole moments are related to quantities that are experimentally accessible, such as emission rates and absorption strengths, it is possible to relate the dipole-dipole energy transfer rate to experimental observables. For example, the dipole-dipole energy-transfer rate can be expressed as a function of the spontaneous decay rate of the donor (γ_d) and the integrated absorption strength of the acceptor (Q_a, units Jm^2) [29, 31],

$$\gamma_{\mathrm{dd}} = \frac{3\hbar^4 c^4 \gamma_d}{4\pi n^4 R^6} Q_\mathrm{a} \int \frac{g_\mathrm{d}(E) g_\mathrm{a}(E)}{E^4} \mathrm{d}E. \tag{1.5}$$

This property allows for a quantitative analysis of energy transfer by dipole-dipole interaction.

There is another important energy-transfer mechanism. Due to the indistinguishability of electrons, the same transfer of energy as depicted in diagram 1.5.2a

can also proceed through the transition shown in diagram 1.5.2b. In this diagram, the atoms exchange electrons. The interaction that governs this energy transfer is dependent on wave function overlap of wavefunctions on different atoms and is called exchange interaction. The energy-transfer rate for exchange interaction has a very strong distance dependence. It is proportional to [31],

$$\gamma_{exch} \propto \exp(-2R/L), \tag{1.6}$$

where L is an effective average Bohr radius of the wavefunctions involved.

1.6 Summary of the thesis

The industrial drive for this research is to find new phosphors for application in mercury-free fluorescent lamps and plasma display panels. The vacuum-ultraviolet (VUV) excitation light which is used in these devices allows for the use of phosphors that show emission of more than one photon for each photon absorbed (quantum cutting). The fundamental challenges of this research are to explore the relatively new area of VUV spectroscopy and to design and study new quantum-cutting phosphors.

This thesis can be divided into three parts. First, the spectroscopic properties of lanthanide ions upon VUV excitation are studied. This work is presented in chapter 2. In the next three chapters the focus is shifted to the study of quantum cutting by two-ion systems upon VUV excitation. Third, in chapter 6 a new route for quantum cutting is investigated by the use of three-ion systems.

In chapter 2 emission spectra and luminescence decay measurements upon excitation with a VUV excimer laser are reported. The high-resolution $4f^{n-1}5d \rightarrow 4f^n$ emission spectra of Ce^{3+}, Pr^{3+}, Nd^{3+}, Er^{3+}, and Tm^{3+} in $LiYF_4$ and YPO_4 are compared to calculated emission spectra. A good agreement between the intensities and locations of the zero-phonon lines is found. Measurements of luminescence lifetimes are presented for the spin-forbidden $4f^{n-1}5d \rightarrow 4f^n$ emissions and compared to calculated lifetimes. The good agreement between experiment and theory demonstrates the correctness of the model developed for the $4f^{n-1}5d$ and $4f^n$ states of the lanthanide ions.

Chapters 3 to 5 deal with quantum-cutting phosphors based on two-ion systems upon VUV excitation. A well-known example for efficient quantum cutting upon VUV excitation is the Gd-Eu couple. For this couple, a model explaining the down conversion mechanism is mainly supported by emission spectra while the kinetics of the energy-transfer processes involved in quantum cutting have hardly been investigated. Chapter 3 deals with the temperature dependent dynamics and spectroscopic properties of the Gd-Eu couple in $LiGdF_4$:Eu^{3+} 0.5%. Decay curves measured at room temperature for the Eu^{3+} $^5D_1$ and $^5D_0$ emissions can be explained by a model based on the kinetics of the quantum-cutting mechanism. Temperature dependent

studies of the Eu^{3+} $^5D_1$, $^5D_0$, Gd^{3+} $^6G_{7/2}$, and $^6P_{7/2}$ emissions show a change in the energy-transfer kinetics that is consistent with the absence of quantum cutting at low temperatures ($T < 50$ K).

In chapters 4 and 5 energy transfer from the Pr^{3+} $^1S_0$ level to suitable co-activators is studied. In chapter 4 co-doping with Eu^{3+} is reinvestigated. Based on the theory for dipole-dipole energy transfer, efficient energy transfer is expected, although Zachau *et al.* [32] observed that energy transfer is absent for Pr-Eu pairs doped in YF_3. In the experiments presented in this chapter the result of Zachau *et al.* is confirmed, but additionally a strong quenching of the Pr^{3+} $^1S_0$ emission by Eu^{3+} is observed. A low-energy metal-to-metal charge-transfer state (Pr^{4+}-Eu^{2+}) for Pr-Eu pairs is proposed to explain the quenching. When Yb^{3+} is used as a co-dopant instead of Eu^{3+} quenching is observed as well. This observation supports the proposed quenching mechanism.

In chapter 5 energy transfer from the Pr^{3+} $^1S_0$ level to Mn^{2+} is studied in a number of fluoride host lattices. The Pr^{3+}-Mn^{2+} pair offers the possibility for cross relaxation: Pr^{3+} $^1S_0$, Mn^{2+} $^6A_1 \rightarrow Pr^{3+}$ $^1I_6$, Mn^{2+} $^4A_1$, ^4E. It is observed that energy transfer is not efficient, in spite of good spectral overlap between donor emissions and acceptor absorptions. To explain the absence of energy transfer, the transfer rates are calculated for cross relaxation through dipole-dipole and exchange interaction. The radiative decay rate of the $^1S_0$ level is indeed larger than the calculated energy-transfer rates, but the complete absence of energy transfer could not be explained. Possible explanations are discussed.

In chapter 6 the focus is shifted towards quantum cutting in three-ion systems via a new mechanism. For the system $Yb_xY_{1-x}PO_4$:Tb^{3+} 1% experimental evidence for cooperative energy transfer is presented. Excitation and emission measurements provide proof of energy transfer from Tb^{3+} to Yb^{3+}. The mechanism is investigated by comparison of luminescence decay measurements for the Tb^{3+} $^5D_4$ emission to Monte Carlo simulations based on theories for cooperative, accretive and phonon-assisted energy transfer. Based on the good agreement between experimental and simulated decay curves, it is concluded that energy transfer proceeds exclusively through cooperative dipole-dipole interaction. The energy-transfer rate to two nearest-neighbor Yb^{3+} ions is 0.26 ms^{-1}. This corresponds to an upper limit for the energy-transfer efficiency of 88% in $YbPO_4$:Tb^{3+} 1%.

The summary above highlights the scientific contributions of this thesis. The work also has important implications for applications. Due to the present work and the efforts of other research groups, it has become clear that the requirements for efficient quantum cutting for the realization of a competitive Xe fluorescent tube (compared to the Hg fluorescent tube) are not met. Due to the lack of good alternatives, lanthanide-based phosphors are still the most promising materials to obtain applicable quantum-cutting phosphors. Unfortunately, prospects for improvement are limited, since an extensive part of the spectroscopic properties of lanthanide ions after VUV excitation has been investigated and most opportunities to obtain

high quantum yields after VUV excitation have been explored by now. Therefore, chances for the development of a commercial Xe fluorescent tube are slim.

Contrary to research on quantum cutting after VUV excitation, little attention has been paid to quantum cutting after ultraviolet or visible excitation. One reason for this is the already extensive knowledge of the energy-level structure of luminescent ions in this spectral region, which limits attractiveness for fundamental researchers. From the application point of view however, interest has increased strongly in the past ten years due to the growing demand for sustainable energy sources. The energy conversion efficiency of solar cells with band edges in the infrared (such as crystalline Si) can be increased by the use of visible-to-infrared quantum-cutting phosphors that convert the visible part of the solar spectrum (without energy loss!) into infrared radiation. Absorption of the infrared radiation instead of the visible radiation by crystalline Si prevents large thermalization losses of hot electrons. A first attempt to realize a visible-to-infrared quantum-cutting phosphor is described in the last chapter of this thesis.

References

[1] M. Planck, Annalen der Physik **4**, 553 (1901).

[2] T. Justel, H. Nikol, and C. Ronda, Angewandte Chemie-International Edition **37**, 3085 (1998).

[3] J. Becquerel, Physikalische Zeitschrift **8**, 632 (1908).

[4] J. Becquerel, Zeitschrift fur Physik **58**, 205 (1929).

[5] H. Bethe, Zeitschrift fur Physik **60**, 218 (1930).

[6] H. A. Kramers, Proc. Acad. Sci. Amsterdam **32**, 1176 (1930).

[7] J. H. van Vleck, Journal of Chemical Physics **41**, 67 (1937).

[8] B. R. Judd, Physical Review **127**, 750 (1962).

[9] G. S. Ofelt, Journal of Chemical Physics **37**, 511 (1962).

[10] G. H. Dieke and H. M. Crosswhite, Applied Optics **2**, 675 (1963).

[11] G. H. Dieke, *Spectra and Energy Levels of Rare Earth Ions in Crystals* (Interscience, New York, 1968).

[12] R. T. Wegh, A. Meijerink, R. J. Lamminmaki, and J. Holsa, Journal of Luminescence **87-89**, 1002 (2000).

[13] J. C. Krupa and M. Queffelec, Journal of Alloys and Compounds **250**, 287 (1997).

[14] M. F. Reid, L. van Pieterson, R. T. Wegh, and A. Meijerink, Physical Review B **62**, 14744 (2000).

[15] L. van Pieterson, R. T. Wegh, A. Meijerink, and M. F. Reid, Journal of Chemical Physics **115**, 9382 (2001).

[16] V. N. Makhov *et al.*, Surface Review and Letters **9**, 271 (2002).

[17] N. Y. Kirikova *et al.*, Journal of Luminescence **110**, 135 (2004).

[18] M. True *et al.*, Journal of Alloys and Compounds **374**, 36 (2004).

[19] T. Ishii, M. G. Brik, and K. Ogasawara, Journal of Alloys and Compounds **380**, 136 (2004).

[20] N. I. of Occupational Safety and Health, International Chemical Safety Cards 56 (2004).

[21] D. R. Lide and ed., *"Physical Constants of Inorganic Compounds", in CRC Handbook of Chemistry and Physics, Internet Version 2005, http://www.hbcpnetbase.com* (CRC Press, Boca Raton, FL, 2005).

[22] F. Vollkommer and L. Hitzsche, *IEEE conf. Record of 23rd Int. Conf. on Plasma Science (ICOPS)* (IEEE, New York, 1996), p. 270.

[23] W. W. Piper, J. A. DeLuca, and F. S. Ham, Journal of Luminescence **8**, 344 (1974).

[24] J. L. Sommerdijk, A. Bril, and A. W. De Jager, Journal of Luminescence **8**, 341 (1974).

[25] S. Kuck *et al.*, Journal of Luminescence **102-103**, 176 (2003).

[26] R. T. Wegh, H. Donker, K. D. Oskam, and A. Meijerink, Science **283**, 663 (1999).

[27] R. T. Wegh, E. V. D. van Loef, and A. Meijerink, Journal of Luminescence **90**, 111 (2000).

[28] B. Henderson and G. F. Imbusch, *Optical Spectroscopy of Inorganic Solids* (Clarendon Press, Oxford, 1989).

[29] T. Forster, Annalen der Physik **2**, 55 (1948).

[30] G. D. Scholes, Annual Review of Physical Chemistry **54**, 57 (2003).

[31] D. L. Dexter, Journal of Chemical Physics **21**, 836 (1953).

[32] M. Zachau, F. Zwaschka, and F. Kummer, Proceedings - Electrochemical Society **97-29**, 314 (1998).

Chapter 2

$4f^{n-1}5d \rightarrow 4f^n$ emission of Ce^{3+}, Pr^{3+}, Nd^{3+}, Er^{3+}, and Tm^{3+} in $LiYF_4$ and YPO_4

This chapter describes the experimental and calculated $4f^{n-1}5d \rightarrow 4f^n$ emission spectra of Ce^{3+}, Pr^{3+}, Nd^{3+}, Er^{3+}, and Tm^{3+} in $LiYF_4$ and YPO_4 host lattices. The positions and intensities of the zero-phonon lines were calculated and compared to the high-resolution emission spectra. For the thulium samples gated detection was used to distinguish between the spin-forbidden and spin-allowed $4f^{n-1}5d \rightarrow 4f^n$ emissions. Luminescence lifetimes for the spin-forbidden $4f^{n-1}5d \rightarrow 4f^n$ emissions were calculated and compared with experimentally observed lifetimes. A good agreement between experiment and theory is found, demonstrating the correctness of the model developed for the $4f^{n-1}5d$ and $4f^n$ states of lanthanide ions.

2.1 Introduction

The recent discovery of efficient quantum cutting in the Gd-Eu system [1] has been an important breakthrough in the search for efficient phosphors upon vacuum ultraviolet (VUV) excitation. After absorption of a VUV photon by Gd-Eu quantum-cutting phosphors, red photons are emitted with a quantum efficiency which is higher than 100%. In combination with a Xe-plasma as a VUV radiation source, Gd-Eu quantum-cutting materials have promising properties for application, for instance in mercury free fluorescent tubes or in plasma display panels.

Gd-Eu quantum cutting has been found in a number of lattices [1–4], with reported quantum efficiencies up to 190% [1]. The quantum-cutting process proceeds by a sequence of two energy-transfer steps. The first step is a Gd^{3+} $^6G_J \rightarrow {}^6P_J$ transition, inducing a transition on a Eu^{3+} ion from $^7F_1$ to $^5D_0$. This leads to one red photon from the Eu^{3+} $^5D_0 \rightarrow {}^7F_J$ transition. The Gd^{3+} $^6P_{7/2} \rightarrow {}^8S$ energy is transported over the Gd^{3+} sublattice and transferred in the second step to another Eu^{3+} ion, leading to ^5D_J emission with J = 0, 1, 2, or 3.

The two major problems for the application of these phosphors are a poor absorption of VUV radiation and degradation under VUV illumination. The 157 nm radiation of the Xe monomer and 172 nm radiation of the Xe dimer are poorly absorbed by the Gd^{3+} ions since the transitions involved are parity and spin forbidden.

A possibility to reduce both problems is the incorporation of a good VUV absorbing ion which subsequently transfers its energy to Gd^{3+}, populating the Gd^{3+} ^6G_J levels. Such a species is generally known as a sensitizer. Not only does sensitization increase the absorption cross section for the desired process, it also reduces the probability for undesired processes like VUV radiation induced degradation.

The search for a good sensitizer has been focussed on s^2 ions such as Pb^{2+}. Experimental studies have shown that the requirement of a Gd^{3+} sublattice in combination with VUV emission of Pb^{2+} above 202 nm (Gd^{3+} $^8S \rightarrow {}^6G_{7/2}$ transition) is not possible [5]. For lanthanide ions this requirement can be fulfilled more easily. In numerous host lattices, $4f^{n-1}5d \rightarrow 4f^n$ (5d-4f) transitions have been reported in the UV region [6], but for lanthanide ions such as Nd^{3+}, Tm^{3+}, and Er^{3+} VUV emission is expected when these ions are doped in fluoride lattices and these ions may be used as sensitizers for the Gd-Eu couple.

VUV 5d-4f emission spectroscopy has received little attention, but due to more powerful high-energy excitation sources research activity is increasing rapidly. Low-resolution VUV emission spectra have been reported for Nd^{3+} [7, 8], Tm^{3+} [7–10], and Er^{3+} [7, 8, 10–14] in a number of fluoride lattices. Recently, Zimmerer *et al.* reported a high-resolution 5d-4f emission band for Er^{3+} doped in $LiYF_4$ [15].

Next to the interest for applications, 5d-4f transitions also provide a fundamental challenge. The level of understanding of the 5d-4f emissions is poor in comparison to the understanding of the 4f-4f transitions. In recent work on 4f-5d absorptions for lanthanide ions a well-established parameter model to describe 4f-4f transitions was

extended to describe the 4f-5d absorption properties [16, 17]. This parameter model now includes the important interactions between the 4f electrons, the 5d electron, and the crystal lattice, and is also suitable to calculate the 5d-4f emission characteristics.

5d-4f emission is expected for Ce^{3+}, Pr^{3+}, Nd^{3+}, Er^{3+}, and Tm^{3+} in various host lattices. The other lanthanide ions do not show 5d-4f emission due to the presence of $4f^n$ levels just below the lowest $4f^{n-1}5d$ state which allows for fast non-radiative decay to the $4f^n$ levels.

In this chapter results are presented on low temperature, high resolution 5d-4f emission spectra of Ce^{3+}, Pr^{3+}, Nd^{3+}, Er^{3+}, and Tm^{3+} in $LiYF_4$ and YPO_4 (except for YPO_4:Tm^{3+} where the charge-transfer band is situated below the $4f^{11}5d$ band). This allows for a more detailed study of the positions and intensities of the zero-phonon lines, together with the fine structure caused by vibronic transitions in the emission spectra. High resolution emission spectra are reported and compared with calculated spectra.

2.2 Theory

The $4f^{n-1}5d$ energy levels can be calculated by using an extended version of the model for the $4f^n$ configurations described in references [18–20]. The $4f^n$ energy levels are calculated using a parameterized Hamiltonian that contains parameters for the electron interactions and crystal-field parameters which describe the interaction of the ion and its ligands.

In short, the Hamiltonian is written as

$$\mathcal{H}(\mathrm{ff}) \;=\; \mathcal{H}_{\mathrm{A}}(\mathrm{ff}) \;+\; \mathcal{H}_{\mathrm{CF}}(\mathrm{ff}) \tag{2.1}$$

where the atomic part $\mathcal{H}_{\mathrm{A}}(\mathrm{ff})$ contains electronic interactions (Coulomb and spin-orbit). The crystal field interactions are represented by $\mathcal{H}_{\mathrm{CF}}(\mathrm{ff})$.

The full expression for $\mathcal{H}_{\mathrm{A}}(\mathrm{ff})$ is:

$$\begin{aligned}\mathcal{H}_{\mathrm{A}}(\mathrm{ff}) \;=\; & \sum_k F^k(\mathrm{ff}) f_k(\mathrm{ff}) \;+\; \zeta(\mathrm{ff}) A_{\mathrm{SO}}(\mathrm{ff}) \\ & + \alpha(\mathrm{ff}) L(L+1) \;+\; \beta(\mathrm{ff}) G(G_2) \;+\; \gamma(\mathrm{ff}) G(R_7) \\ & + \sum_i T^i(\mathrm{ff}) t_i(\mathrm{ff}) \;+\; \sum_k P^k(\mathrm{ff}) p_k(\mathrm{ff}) \\ & + \sum_j M^j(\mathrm{ff}) m_j(\mathrm{ff})\end{aligned} \tag{2.2}$$

with k = 2, 4, 6; i = 2, 3, 4, 6, 7, 8 and j = 0, 2, 4. The Coulomb interaction is parameterized by the F^k parameters. $\zeta(\mathrm{ff})$ defines the spin-orbit interaction. The two- and three-body correlations are parameterized by $\alpha(\mathrm{ff})$, $\beta(\mathrm{ff})$, $\gamma(\mathrm{ff})$ and $\mathrm{T}^i(\mathrm{ff})$. Higher order magnetic interactions are parameterized by $\mathrm{M}^j(\mathrm{ff})$ and $\mathrm{P}^k(\mathrm{ff})$.

The crystal-field splitting of the $4f^n$ states is determined by

$$\mathcal{H}_{\mathrm{CF}}(\mathrm{ff}) \;=\; \sum_{k,q} B_q^k(\mathrm{ff}) C_q^{(k)}(\mathrm{ff}), \tag{2.3}$$

where the $B_q^k(\mathrm{ff})$ parameters define the radially dependent part of the one-electron crystal-field interaction, and $C_q^{(k)}(\mathrm{ff})$ are the many-electron spherical tensor operators for the $4f^n$ configuration. For configurations concerning 4f-electrons the values of k are restricted to 2, 4 and 6. The applicable values of q depend on the site-symmetry of the lanthanide ion in the host lattice. Rare earth ions in $LiYF_4$ occupy sites with S_4 symmetry with only a small deviation from D_{2d} symmetry. D_{2d} is the exact site-symmetry for rare earth ions in YPO_4. For D_{2d} symmetry the allowed values for q are 0 and ± 4 [19].

To expand the well-known model for the calculation of $4f^n$ energy levels to $4f^{n-1}5d$ configurations the contributions of the d-electron have to be included [16]. These are the spin-orbit interaction for the d-electron, the crystal-field interactions of the d-electron and the Coulomb interaction between the 4f-electron and the 5d-electron. The addition to the Hamiltonian is:

$$\mathcal{H}(\mathrm{fd}) \;=\; \mathcal{H}_A(\mathrm{fd}) \;+\; \mathcal{H}_{\mathrm{A}}(\mathrm{dd}) \;+\; \mathcal{H}_{\mathrm{CF}}(\mathrm{dd}) \tag{2.4}$$

The atomic Hamiltonian is written as:

$$\mathcal{H}_{\mathrm{A}}(\mathrm{fd}) \;=\; \Delta_{\mathrm{E}}(\mathrm{fd}) \;+\; \sum_k F^k(\mathrm{fd}) f_k(\mathrm{fd}) + \sum_j G^j(\mathrm{fd}) g_j(\mathrm{fd}) \tag{2.5}$$

$$\mathcal{H}_{\mathrm{A}}(\mathrm{dd}) \;=\; \zeta_{\mathrm{SO}}(\mathrm{dd}) A_{\mathrm{SO}}(\mathrm{dd}) \tag{2.6}$$

with k = 2 and 4, j = 1, 3 and 5. $F^k(\mathrm{fd})$ and $G^i(\mathrm{fd})$ are the direct and exchange Slater parameters for the Coulomb interaction between the d-electron and the 4f-electrons. $\zeta_{\mathrm{SO}}(\mathrm{dd})$ represents the spin-orbit interaction for the 5d-electron.

The 5d-levels are also split by the crystal field. This is parameterized by $\mathcal{H}_{\mathrm{CF}}(\mathrm{dd})$:

$$\mathcal{H}_{\mathrm{CF}}(\mathrm{dd}) \;=\; \sum_{k,q} B_q^k(\mathrm{dd}) C_q^{(k)}(\mathrm{dd}) \tag{2.7}$$

where k is limited to 2 and 4, while q can be 0 or ± 4 for D_{2d} symmetry.

The term $\Delta_{\mathrm{E}}(\mathrm{fd})$ defines the energy difference between the $4f^n$ ground state and the barycenter of the $4f^{n-1}5d$ excited state. Adjusting this value does not influence the splitting of the 5d-levels, it shifts them all by the same energy.

Emissions from the $4f^{n-1}5d$ excited state to the $4f^n$ ground states are allowed electric dipole transitions and it is possible to calculate the matrix elements of the electric dipole operator for these transitions. Electrons in 5d-orbitals do participate in the chemical bond between the lanthanide ion and its ligands. As a result,

$4f^n \leftrightarrow 4f^{n-1}5d$ transitions are characterized by a much stronger electron-phonon coupling than $4f^n \leftrightarrow 4f^n$ transitions. Typical Huang-Rhys factors for $4f^n \leftrightarrow 4f^{n-1}5d$ transitions range from 1.5 to 5. This causes most of the intensity to show up in the vibronic bands of the emission spectra. In our model a Gaussian shape of the vibronic band is assumed, due to the superposition of coupling with several vibrational modes. The energy level calculations provide the positions of the zero-phonon lines of the emissions and Gaussian shaped bands are superimposed on those lines. The energy difference between the zero-phonon line and the maximum of the Gaussian band can be estimated from the cerium excitation spectrum [16].

The radiative transition probability from the initial state $\nu\Gamma_{\mathrm{fd}}$ to the final state $\nu'\Gamma_{\mathrm{f}}$ is given by [21]

$$A(\mathrm{ED}) \;=\; \frac{1}{4\pi\epsilon_0}\,\frac{4n\omega^3}{3\hbar c^3}\,\left(\frac{E_{\mathrm{loc}}}{E}\right)^2\,\frac{1}{g_{\mathrm{fd}}}\,S_{\mathrm{tot}}(\nu\Gamma_{\mathrm{fd}}\nu'\Gamma_{\mathrm{f}}). \tag{2.8}$$

In this equation ϵ_0 is the vacuum permittivity, n is the refractive index, ω is the angular frequency of the emission, $(E_{\mathrm{loc}}/E)^2$ is the local field correction and g_{fd} is the degeneracy of the excited state. We used a refractive index of 1.46 for $LiYF_4$ and 1.75 for YPO_4 which is a good approximation for the average value of n in the wavelength region of the emissions studied [22]. The local field correction is given by $\left((n^2+2)/3\right)^2$ [23]. The total electric dipole strength S_{tot} is the sum of its components:

$$S_{\mathrm{tot}} \;=\; S_x + S_y + S_z, \tag{2.9}$$

where

$$\begin{aligned} S_{x,y} \;&=\; \sum_{\gamma_{\mathrm{f}},\gamma_{\mathrm{fd}}} \frac{1}{2}\big|\,\langle \nu'\Gamma_{\mathrm{f}}\gamma_{\mathrm{f}}|erC^1_{-1}|\nu\Gamma_{\mathrm{fd}}\gamma_{\mathrm{fd}}\rangle \\ &\quad \pm\,\langle \nu'\Gamma_{\mathrm{f}}\gamma_{\mathrm{f}}|erC^1_{1}|\nu\Gamma_{\mathrm{fd}}\gamma_{\mathrm{fd}}\rangle\,\big|^2, \end{aligned} \tag{2.10}$$

$$S_z \;=\; \sum_{\gamma_f,\gamma_{\mathrm{fd}}} \left|\langle \nu'\Gamma_{\mathrm{f}}\gamma_{\mathrm{f}}|erC^1_{0}|\nu\Gamma_{\mathrm{fd}}\gamma_{\mathrm{fd}}\rangle\right|^2. \tag{2.11}$$

The summation in equations (2.10) and (2.11) is over the squared transition-dipole moments from the excited states $\nu\Gamma_{\mathrm{fd}}$ to the final states $\nu'\Gamma_{\mathrm{f}}$. C^1_q is a spherical tensor operator as defined in Refs [24] and [25]. The lifetime of the emissions was calculated by taking the inverse of the spontaneous transition probability $A(\mathrm{ED})$. Radial integrals $\langle 5\mathrm{d}|r|4\mathrm{f}\rangle$ were calculated using Cowans program [25] and are included in table 2.3.

2.3 Experimental

Microcrystalline powders of YPO_4 doped with 1% RE^{3+} (RE = Ce, Pr, Nd, Er, Tm) were prepared by firing a mixture of Y_2O_3 (4N), the corresponding RE_2O_3 (4N) and

$(NH_4)_2HPO_4$ in air at 1350°C for three hours. A YPO_4 crystal doped with 2% of Nd^{3+} was kindly provided by dr. L. Boatner from Oak Ridge National Laboratory. A microcrystalline powder of $LiYF_4$ doped with 0.1% Pr^{3+} was prepared by firing a mixture of YF_3, LiF and PrF_3 in stoichiometric ratios (with a 10% excess of LiF) in a flow of ultrapure nitrogen at 600°C.

$LiYF_4$ single crystals containing 1 to 4% of RE ions were grown in a Philips PH 1006/13 high frequency furnace with YF_3, REF_3 and LiF (15% excess) as the starting compounds. The reactants were mixed and transferred to a vitreous carbon crucible. In order to remove water and oxygen the sample was heated overnight at 300°C in a flow of ultrapure nitrogen. Subsequently the temperature was raised to 550°C and SF_6 was introduced in the reaction chamber for 30 minutes to remove the last traces of water and oxygen. During the rest of the synthesis a nitrogen atmosphere was maintained. The sample was heated until melting was observed. Next, the sample was cooled to room temperature in 10 hours.

Both the $LiYF_4$ and YPO_4 samples were checked for phase purity by recording a powder diffractogram using a Philips PW1729 X-ray diffractometer using CuK_α radiation. All samples were single phase.

Emission measurements were performed at liquid-helium temperatures using a cold-finger type Oxford Instruments Optistat$^{CF\text{-}V}$ liquid-helium flow cryostat, equipped with MgF_2 windows. The excitation source consisted of a TuiLaser ExciStar S-200 F_2 laser producing 1 mJ pulses of approximately 10 nanoseconds at 157 nm using fluorine and 2 mJ pulses at 193 nm using an argon/fluorine mixture, both with a repetition rate of 100 Hz. Emission spectra were recorded using a 0.550 m Jobin Yvon TRIAX 550 monochromator with a 3600 lines/mm grating blazed for the VUV/UV. The emission was detected using a Hamamatsu R166UHP or R7154 solar blind photo multiplier tube for the VUV and UV emissions up to 300 nm. Emission between 300 and 700 nm was detected using a Hamamatsu R928 photomultiplier tube, in combination with a 1200 lines/mm grating blazed at 400 nm. For the emission spectra of thulium-doped samples gated detection was performed using a Stanford Research SR400 boxcar averager. Luminescence lifetime measurements were performed using a Tectronix 2440 digital oscilloscope.

2.4 Results and Discussion

2.4.1 Parameter values

The zero-phonon lines in the $4f^{n-1}5d \rightarrow 4f^n$ emission spectra originate from transitions from the lowest $4f^{n-1}5d$ state to the different crystal field levels of the $4f^n$ final levels. For every zero-phonon line a vibronic side band with fine structure is present. In order to have a better agreement between the measured and calculated splitting of the $4f^n$ multiplets, we refitted the parameter values for the calculation of the $4f^n$ levels to the experimental values for the energy levels reported for

Pr^{3+} [26,27], Nd^{3+} [27,28], Er^{3+} [29,30] ,and Tm^{3+} [31] in $LiYF_4$ and YPO_4. Due to the continuous improvements in the model and computer programs for the energy level calculations it is possible to obtain a significantly better agreement between the calculated and observed energy levels than with the parameter values reported previously [26–31]. Since the positions of the zero-phonon lines depend strongly on the positions of the $4f^n$ final states, the use of better parameter values gives a better agreement between the calculated and experimentally observed $4f^{n-1}5d \rightarrow 4f^n$ emission spectra. The improved values for the fitting parameters are summarized in table 2.1. Parameters that were kept fixed in the fitting procedure are indicated in brackets. For Pr^{3+} and Nd^{3+} in $LiYF_4$ and Er^{3+} in both $LiYF_4$ and YPO_4 correlated crystal field interaction was also taken into account since it helped to improve the quality of the fit. For other cases the inclusion of correlated crystal-field parameters did not help and no values for the correlated crystal-field parameters are included in table 2.1.

As far as we know, the crystal field levels of the $^2F_{5/2}$ and $^2F_{7/2}$ states of Ce^{3+} in $LiYF_4$ are not reported in the literature. Using the high resolution $4f^{n-1}5d \rightarrow 4f^n$ emission spectrum (see next section), five of the seven crystal field levels could be determined and were used to fit new parameter values. In this fit the value of ζ(dd) was kept fixed at the free-ion value of 1082 and the crystal field splitting of the d-levels was taken from the excitation spectrum reported by Van Pieterson [32].

The parameter values for the calculation of the excited $4f^{n-1}5d$ configurations are listed in table 2.2. The f-d Coulomb interaction parameters F^k(fd) and G^j(fd) are the values reported by Cowan [25] reduced to 75% for Pr^{3+} and Nd^{3+} and reduced to 67% for Er^{3+} and Tm^{3+} [16, 17]. For Ce^{3+} doped in the $LiYF_4$ host lattice the spin-orbit coupling represented by ζ(dd) and the crystal-field parameters B_q^k(dd) were obtained from the fit performed by Van Pieterson [16]. For Ce^{3+} doped in the YPO_4 host lattice the ground-state levels of Ce^{3+} reported for $LuPO_4$ [33] and the 5d-excited state energies reported for YPO_4 [16] were used to obtain an 'exact' fit, since the number of energy levels is equal to the number of parameters varied. The 4f parameters found are similar to those reported for $LuPO_4$. The 5d parameter values are similar to the values obtained by Van Pieterson, except ζ(dd) which was kept fixed at the free-ion value of 1149 cm^{-1}, whereas we obtained a ζ(dd) of 1188 cm^{-1}.

The spin-orbit coupling and crystal-field parameters used for the calculation of the $4f^{n-1}5d$ configurations for Pr^{3+}, Nd^{3+}, Er^{3+}, and Tm^{3+} in $LiYF_4$ were taken from the report by Van Pieterson [7]. The parameter values for the same ions in YPO_4 were set to the ratios of the corresponding parameter values for Ce^{3+} in $LiYF_4$ and YPO_4.

The Δ_E(fd) values were adjusted to set the calculated energy of the zero-phonon line for the lowest $4f^{n-1}5d \rightarrow 4f^n$ emission equal to the experimentally observed zero-phonon line in the emission spectrum.

Table 2.1: Parameter values (in cm^{-1}) used for the $4f^n$ energy level calculation of Ce^{3+}, Pr^{3+}, Nd^{3+}, Er^{3+}, and Tm^{3+} in $LiYF_4$ and YPO_4. Parameters that were not varied are listed in brackets.

	Ce^{3+}	Pr^{3+}		Nd^{3+}		Er^{3+}		Tm^{3+}
	$LiYF_4$	$LiYF_4$	YPO_4	$LiYF_4$	YPO_4	$LiYF_4$	YPO_4	$LiYF_4$
E_{AVG}	1517	10204	9999	24413	24105	35806	35569	18022
F^2(ff)		69025	67991	72667	71872	97449	96567	102215
F^4(ff)		50580	50031	52737	51793	68539	68144	72060
F^6(ff)		33326	32961	35817	35591	56051	53393	51366
α(ff)		[23.00]	21.30	21.49	19.87	18.27	19.97	18.20
β(ff)		–649	–683	–585	–606	[–580]	[–632]	–686
γ(ff)		[1371]	[1371]	1424	1445	[1416]	[1800]	[1820]
T^2(ff)				331	[298]	[486]	[400]	[400]*
T^3(ff)				43	[35]	[43]	[43]	[43]*
T^4(ff)				84	[59]	[81]	[73]	[73]*
T^6(ff)				–324	[–285]	[–327]	[–271]	[–271]*
T^7(ff)				387	[332]	[300]	[308]	[308]*
T^8(ff)				322	[305]	[346]	[299]	[299]*
ζ(ff)	628	750.1	742.1	870.1	876.3	2374	2364	2633
B_0^2(ff)	316	541	73	400	329	306	210	354
B_0^4(ff)	[–1150]	–1093	324	–1122	273	–581	81	–631
B_4^4(ff)	–1264	–1327	–856	–1272	–758	–917	–670	–851
B_0^6(ff)	[–89]	–45	–1278	–28	–1226	–6	–704	–171
B_4^6(ff)	–821	–1165	7	–1093	–89	–637	–61	–627
M_0(ff)†		[2.00]	0.99	0.66	2.11	3.91	5.48	4.67
P_2(ff)‡		215	220	162	284	579	802	720
D^2(ff)		–15.9		4.9		5.3		
D^4(ff)		8.8		10.1		4.0	–1.02	

* Only for the excited $4f^{11}5d$ configuration

† M_2 and M_4 parameter values were included with the ratios $M_2/M_0 = 0.56$ and $M_4/M_0 = 0.31$

‡ P_4 and P_6 parameter values were included with the ratios $P_4/P_2 = 0.5$ and $P_6/P_2 = 0.1$

2.4.2 Emission spectra

Cerium

The high resolution 5d→4f emission spectrum of $LiYF_4$:Ce^{3+} 1% upon 193 nm excitation at 10 K is shown in figure 2.1. The spectrum shows two broad emission bands with the highest energy zero-phonon lines at 298.94 and 320.20 nm which corresponds to emission from the 5d level to the lowest energy crystal field components of the $^2F_{5/2}$ and $^2F_{7/2}$ states of cerium. The energy difference observed between the $^2F_{5/2}$ and $^2F_{7/2}$ levels is 2221 cm^{-1}. Figure 2.1 also shows the simulated 5d→4f emission spectrum of $LiYF_4$:Ce^{3+} based on the 5d parameters reported by Van Pieterson *et al.* [16] and the 4f parameters obtained from a fit to the positions of the $^2F_{5/2}$ and

Table 2.2: Parameter values (in cm^{-1}) used for the $4f^{n-1}5d$ energy level calculation of Ce^{3+}, Pr^{3+}, Nd^{3+}, Er^{3+}, and Tm^{3+} in $LiYF_4$ and YPO_4.

	Ce^{3+}	Pr^{3+}		Nd^{3+}		Er^{3+}		Tm^{3+}
	$LiYF_4$	$LiYF_4$	YPO_4	$LiYF_4$	YPO_4	$LiYF_4$	YPO_4	$LiYF_4$
Δ_E(fd)	43773	50966	47021	56684	52772	89762	86822	94218
F^2(fd)		22703	22703	22543	22543	19724	19724	19639
F^4(fd)		11321	11321	11188	11188	9358	9358	9275
F^6(fd)		9677	9677	9608	9608	8038	8038	7991
G^3(fd)		8370	8370	8284	8284	6848	6848	6789
G^5(fd)		6518	6518	6442	6442	5292	5292	5240
ζ(dd)	[1082]	1149	1188	1216	1257	1768	1821	1839
B_0^2(dd)	4673	4626	4763	4598	4734	4290	4417	4252
B_0^4(dd)	–18649	–18463	2221	–18351	2208	–17120	2060	–16971
B_4^4(dd)	–23871	–23632	–22568	–23489	–22431	–21914	–20927	–21723

$^2F_{7/2}$ crystal field components in the measured emission spectrum. The parameter values for the calculation are listed in tables 2.1 and 2.2. Besides the zero-phonon lines the spectrum also shows some weak vibronic lines. The low intensity of the highest energy zero-phonon line in the experiment is due to resonant reabsorption of this emission.

Praseodymium

Figure 2.2 shows the calculated and the experimentally observed emission spectrum of $LiYF_4$:Pr^{3+} 0.1% upon excitation at 157 nm. The assignment of transitions is indicated in the figure. Fine structure is observed for all emission bands except for the highest energy emission. No clear vibronic progression can be observed in the emission spectrum. The intensity ratios of the emission bands are in excellent agreement with the ratios shown in the simulated spectrum. The calculated energy of the emission to the $^1G_4$ levels situated at 272 nm, however, is too low. It is known for trivalent praseodymium that the energy of the $^1G_4$ multiplet is influenced by correlated crystal field interactions if two electrons occupy the same orbital, but even with inclusion of correlated crystal field interaction the calculation model predicts the position of the $^1G_4$ at a somewhat different energy. The parameter values used for the calculation are summarized in tables 2.1 and 2.2.

Figure 2.3 shows the calculated and experimentally observed emission spectrum of YPO_4:Pr^{3+} 1% upon excitation at 157 nm. Besides sharp zero-phonon lines this spectrum also displays a clear vibronic structure on the emission bands for the transitions to the $^3H_4$, $^3H_5$ and $^3H_6$ multiplets. The parameter values used for the calculation are summarized in tables 2.1 and 2.2. The intensities of the emission bands and the relative intensities of the zero-phonon lines of the experiment is closely re-

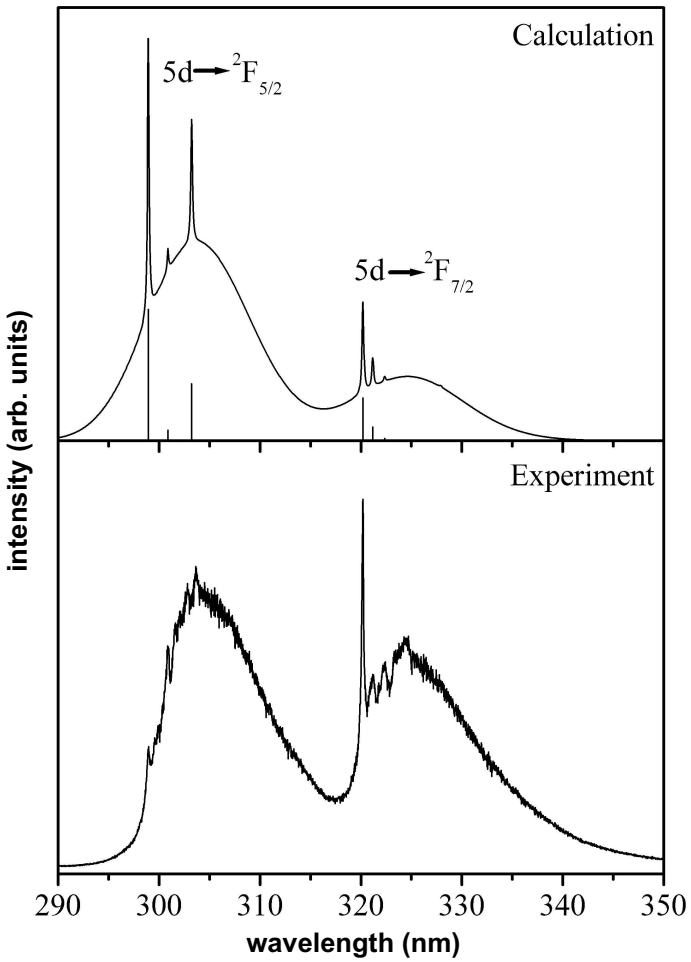

Figure 2.1: Calculated and measured emission spectrum of $LiYF_4$:Ce^{3+} 1% upon excitation at 193 nm at 10 K. In the upper spectrum the sticks give information on the positions and intensities calculated for the zero-phonon lines while the spectrum is obtained by superimposing a Gaussian band (offset 600 cm^{-1}, width 1000 wavenumbers) on the zero-phonon lines which have been given a width of 20 cm^{-1}. The same procedure is used in figures 2.2 to 2.9.

produced in the calculated spectrum. Also the positions of the zero-phonon lines are in good agreement. Clearly, the model and the parameter values for the $4f^{n-1}5d$ states and the $4f^n$ states for Pr^{3+} in YPO_4 give a good description of the actual states involved.

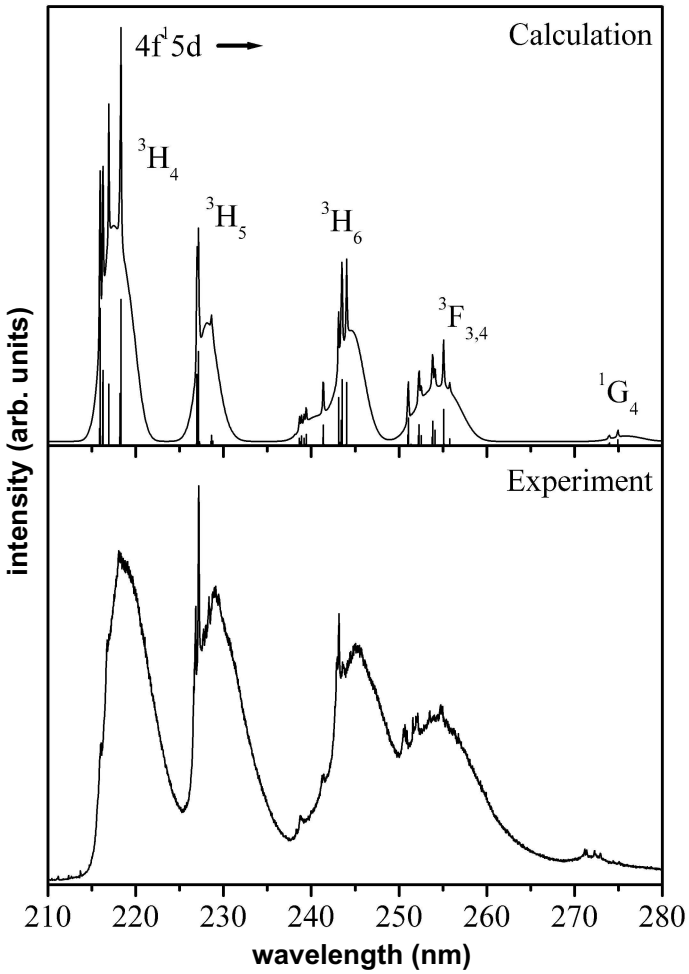

Figure 2.2: Calculated and measured emission spectrum of $LiYF_4$:Pr^{3+} 0.1% upon excitation at 157 nm at 10 K. See also figure 2.1.

The main difference between the experimental and calculated spectrum is in the vibronic structure. In the model a vibronic Gaussian band is superimposed on the zero-phonon line. For the $4f^{n-1}5d \rightarrow 4f^n$ emission spectra for the lanthanide ions in $LiYF_4$ a broad vibronic band gives a reasonably good description since vibronic features are not clearly observed. However, in the case of YPO_4 the Huang-Rhys factor is smaller for the $4f^{n-1}5d \rightarrow 4f^n$ transitions which results in a higher relative intensity of the zero-phonon lines and the observation of sharp vibronic lines corresponding to coupling with well-defined vibrational modes. From the analysis of the vibronic

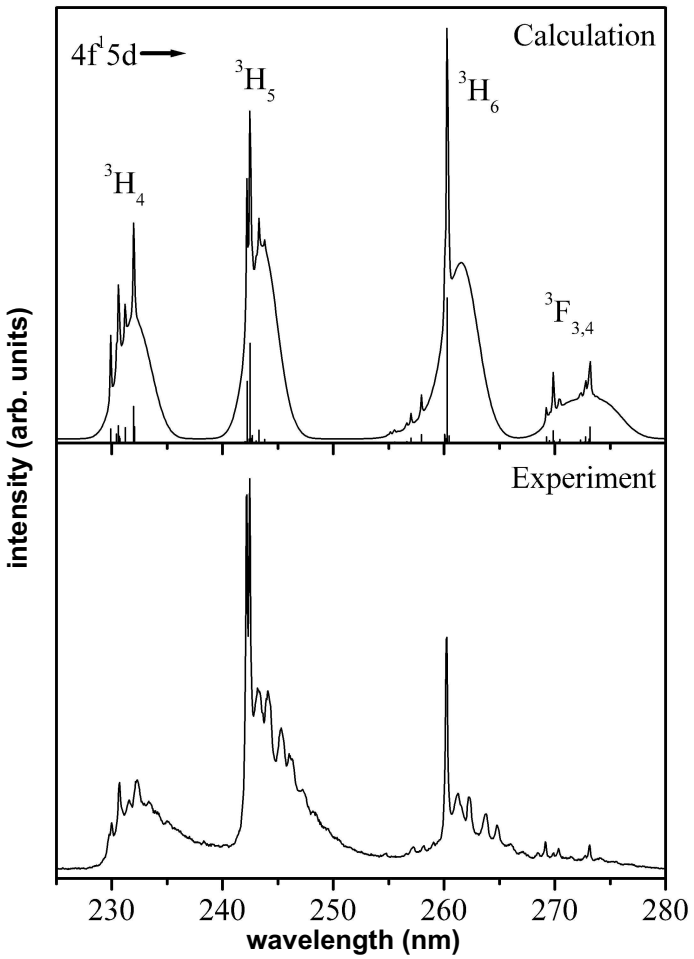

Figure 2.3: Calculated and measured emission spectrum of YPO_4:Pr^{3+} 1% upon excitation at 157 nm at 10 K. See also figure 2.1.

lines in figure 2.3 vibrational modes of 148 cm^{-1} and 370 cm^{-1} can be observed. A further analysis of the vibronic structure of the $4f^{n-1}5d \rightarrow 4f^n$ emission bands in YPO_4 is an interesting topic for further studies.

Neodymium

The spectra depicted in figures 2.4 and 2.5 show the calculated and experimentally observed $4f^25d \rightarrow 4f^3$ emission spectrum of $LiYF_4$:Nd^{3+} and YPO_4:Nd^{3+}, respectively, upon excitation at 157 nm at 10 K. The emissions to the $^4I_{9/2}$, $^4I_{11/2}$ and $^4I_{13/2}$

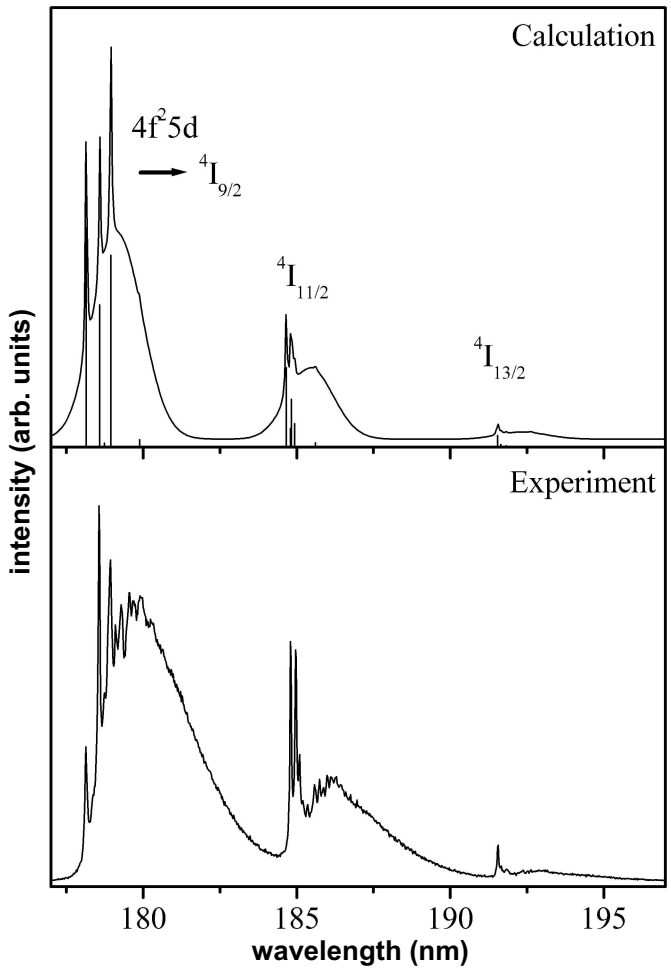

Figure 2.4: Calculated and measured emission spectrum of $LiYF_4:Nd^{3+}$ 1% upon excitation at 157 nm at 10 K. See also figure 2.1.

levels are shown and indicated in the figures. For both $LiYF_4:Nd^{3+}$ and $YPO_4:Nd^{3+}$ the positions and intensities of the zero-phonon lines in the simulated spectra are in good agreement with the experimentally obtained spectra. The highest energy zero-phonon line of the emission to the $^4I_{9/2}$ levels of both $LiYF_4:Nd^{3+}$ and $YPO_4:Nd^{3+}$ are weak due to reabsorption. In the emission spectrum of $LiYF_4:Nd^{3+}$ a vibronic structure is visible, albeit weak. For $YPO_4:Nd^{3+}$ a clear vibronic progression is observed just as for $YPO_4:Pr^{3+}$. Due to the presence of many zero-phonon lines it is not possible to assign energies to vibrations unambiguously. The parameter values

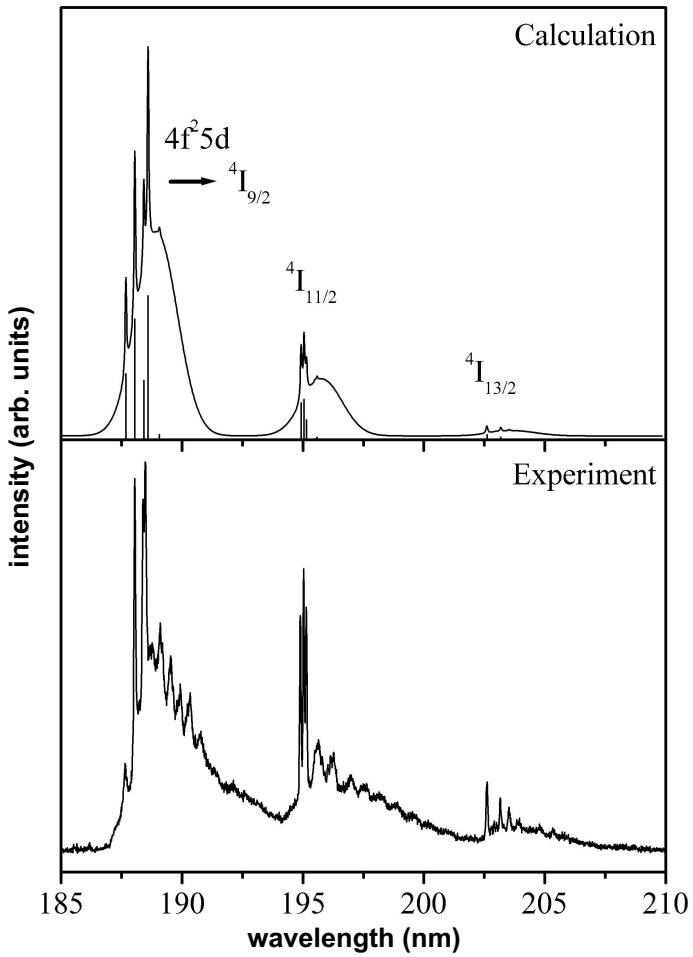

Figure 2.5: Calculated and measured emission spectrum of YPO_4:Nd^{3+} 1% upon excitation at 157 nm at 10 K. See also figure 2.1.

used for the calculations are summarized in tables 2.1 and 2.2.

Erbium

Figure 2.6 shows the calculated and experimentally observed emission spectrum of $LiYF_4$:Er^{3+} upon 157 nm excitation at 10 K. At this excitation wavelength only the high-spin $4f^{10}5d$ state is populated (the onset of the low-spin excitation is at 155 nm [17]) and as a result only spin-forbidden emission is observed. The emission from the high-spin $4f^{10}5d$ state to the $^4I_{15/2}$ ground state is very intense com-

pared to the emission to the $^4I_{13/2}$ level. The much higher relative intensity of the higher energy emission band is reproduced in the calculated emission spectrum. In fact, the calculated relative intensity of the emission band to the $^4I_{13/2}$ level is even weaker than in the experiment. This may be (partly) due to the fact that the emission spectra could not be corrected for the wavelength dependence of the instrumental response. Note that the observation of the weak $4f^{10}5d \rightarrow 4f^{11}(^4I_{13/2})$ emission band is hampered by the presence of emission bands around 180 nm and 185 nm due to a contamination with Nd^{3+}. The fact that these emissions show up as relatively strong bands is due to the fact that at 157 nm the Er^{3+} ion is excited in a spin-forbidden transition while the Nd^{3+} ion has a strong spin-allowed absorption band. The small relative intensity of the emission band corresponding to the $4f^{10}5d \rightarrow 4f^{11}(^4I_{13/2})$ transition can be understood on the basis of J-selection rules. Transitions with ΔJ of ± 1 are expected to have the highest transition probability for $4f^{n-1}5d \leftrightarrow 4f^n$ transitions. The lowest calculated high-spin $4f^{10}5d$ state has 89% contributions of J=17/2 states. In accordance with the ΔJ selection rule the highest emission intensity is expected for the emission to the $^4I_{15/2}$ ground state, which is observed in both the simulated and the experimental emission spectrum.

In figure 2.7 the calculated and experimentally observed emission spectrum of YPO_4 doped with Er^{3+} upon 157 nm excitation at 10 K is shown. At this excitation wavelength the low-spin $4f^{10}5d$ state is populated [17] and after relaxation to the high-spin state spin forbidden emission is observed. Just as in $LiYF_4$ the emission from the high-spin $4f^{10}5d$ state to the $^4I_{15/2}$ ground state is very intense compared to the emission to the $^4I_{13/2}$ level. The measured intensity ratio between the emissions to the $^4I_{15/2}$ and the $^4I_{13/2}$ levels differs from the calculated intensity ratio. The relative intensity of the higher energy band is expected to increase if the spectrum could be corrected for the wavelength dependence of the instrumental response resulting in a better agreement with the calculated spectrum. The parameter values used for the calculation are summarized in tables 2.1 and 2.2. The emission band at 170 nm shows a clear vibronic progression. The weak emissions at 188 nm are due to contamination of the sample with neodymium. The sharp emission lines at 184 nm are due to the intraconfigurational $4f^n\ ^2F_{7/2} \rightarrow ^4I_{15/2}$ transition of erbium. For YPO_4:Er^{3+} the influence of the ΔJ selection rule is also observed. The lowest calculated high-spin $4f^{10}5d$ state has 81% contributions of J=17/2 states. According to the ΔJ selection rule the highest emission intensity is expected (and calculated) for the emission to the $^4I_{15/2}$ ground state, which is indeed observed in the spectrum.

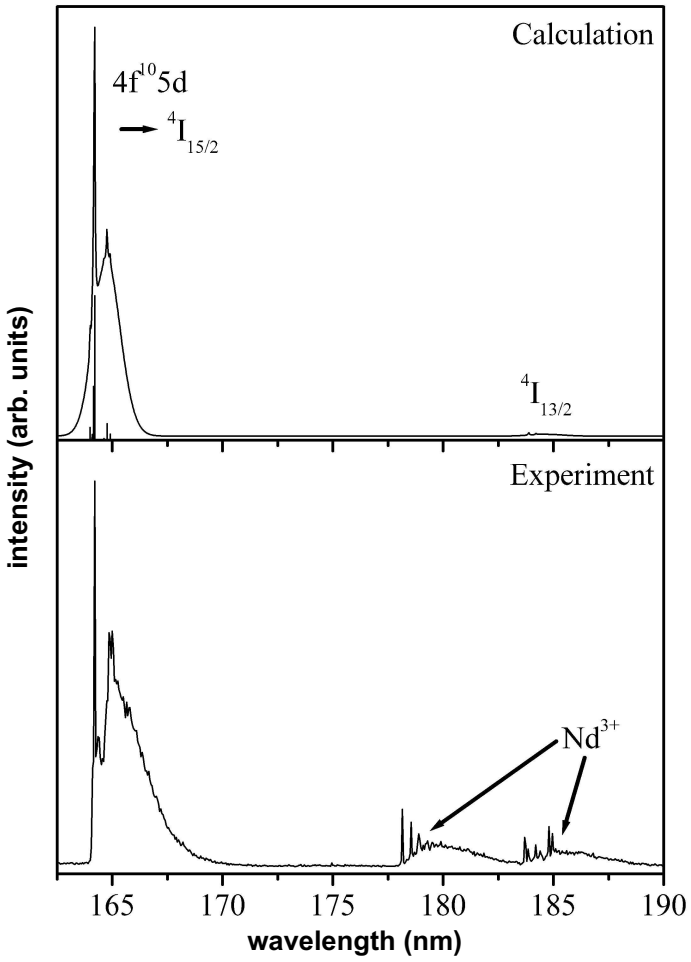

Figure 2.6: Calculated and measured emission spectrum of $LiYF_4$:Er^{3+} 1% upon excitation at 157 nm at 10 K. See also figure 2.1.

Thulium

Figure 2.8 shows the calculated and experimentally observed emission spectrum of $LiYF_4$ doped with Tm^{3+}. Upon excitation at 157 nm emission from both the high-spin and low-spin $4f^{11}5d$ state are observed. The corresponding simulated emission spectra were calculated separately and plotted with a ratio of the high-spin/low-spin emission intensity chosen to match the experimentally observed spectrum. The parameter values used for the calculations are summarized in tables 2.1 and 2.2. The calculated and measured intensities are in good agreement, except for the spin-

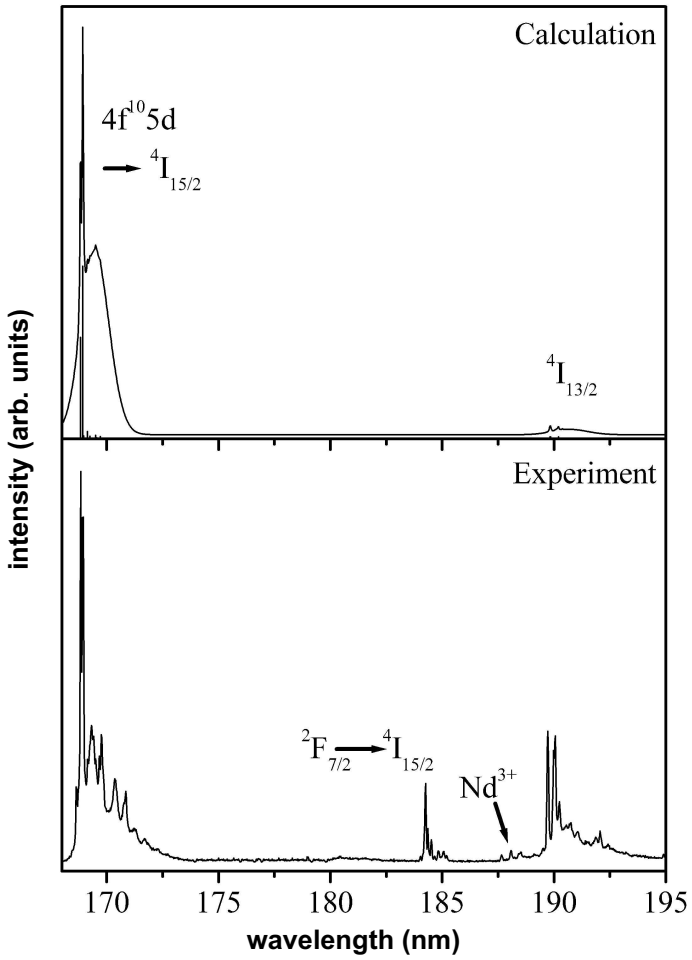

Figure 2.7: Calculated and measured emission spectrum of YPO_4:Er^{3+} 1% upon excitation at 157 nm at 10 K. See also figure 2.1.

allowed emission to the $^3H_6$ levels at 160 nm, which is weaker in the experimental spectrum. This is due to the low sensitivity of the photomultiplier tube at this wavelength. The steep increase on the left hand side of the experimental spectrum is a due to scattered 157 nm radiation of the laser.

With the use of gated detection it was possible to record an emission spectrum for $LiYF_4$:Tm^{3+} showing only the spin-forbidden emissions. The spin-allowed fd-emission for Tm^{3+} in $LiYF_4$ has a 16 ns life time [7] and by applying gated detection with a delay of 1 μs and a gate of 5 μs, only the longer lived spin-forbidden emission ($\tau = 5.4\ \mu s$) is detected. The resulting emission spectrum is depicted in figure 2.9

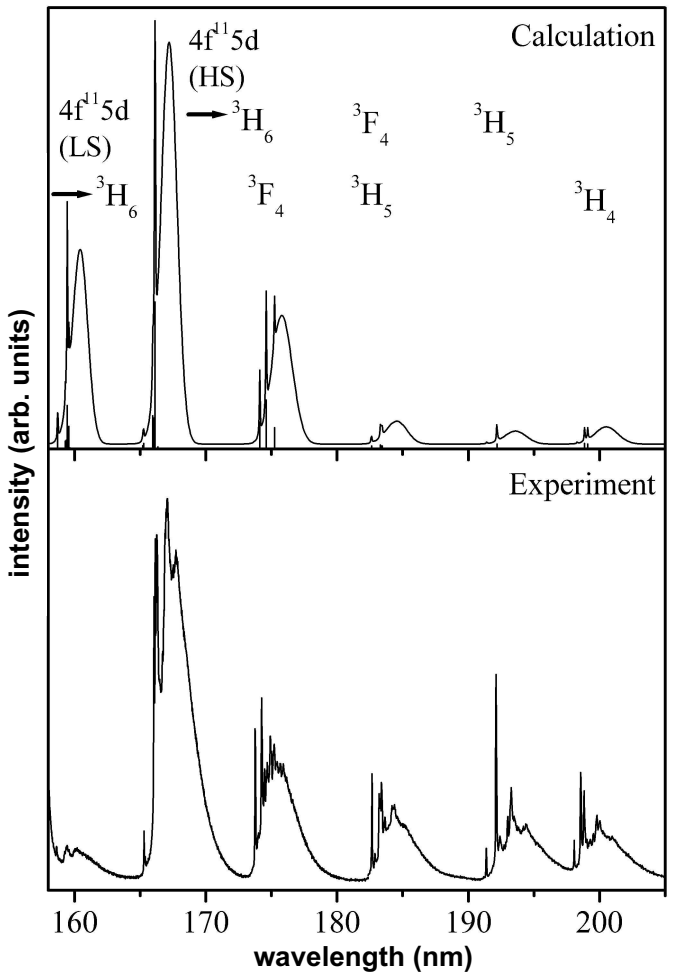

Figure 2.8: Calculated and measured emission spectrum of $LiYF_4:Tm^{3+}$ 1% upon excitation at 157 nm at 10 K. The spin-allowed and spin-forbidden emission spectra were calculated separately and their relative intensity was set to match the experimentally observed spectrum. See also figure 2.1.

together with the calculated spin-forbidden emission spectrum. The intensity ratios of the zero-phonon lines in the emission spectra show a good agreement with the calculated intensities.

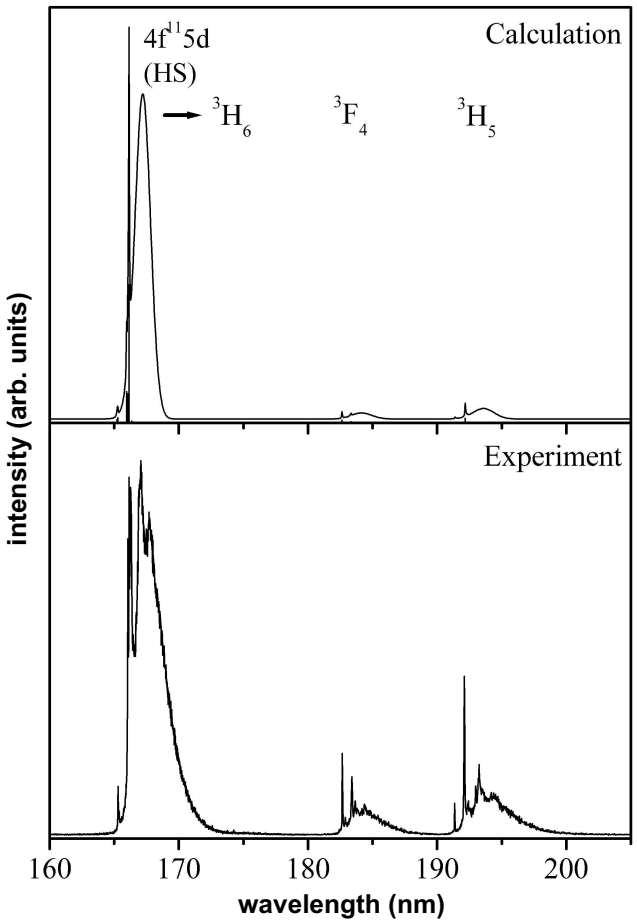

Figure 2.9: Calculated and measured spin-forbidden emission spectrum of $LiYF_4$:Tm^{3+} upon excitation at 157 nm at 10 K using gated detection (delay 1 μs, gate 5 μs). See also figure 2.1.

2.4.3 Luminescence lifetime measurements

The lifetime of the spin-forbidden $4f^{n-1}5d \rightarrow 4f^n$ emission was measured for Er^{3+} in $LiYF_4$ and YPO_4 and for Tm^{3+} in $LiYF_4$. In figure 2.10 a typical example of a luminescence decay curve is shown. The longer time (> 2 μs) part of the luminescence decay is well-described by a single exponential with a lifetime in the order of μs. The flattening at shorter times is due to saturation of the detector. The experimentally observed lifetimes are included in table 2.3. The presently reported lifetimes are somewhat different from values published previously by us and also

other groups [7, 13]. The reason is that in previous work the life times were obtained from luminescence decay curves measured at a synchrotron. The repetition rate (typically MHz) of synchrotron radiation is determined by the round trip time of bunches in the ring and is too high to accurately determine lifetimes that are μs or longer. For MHz repetition rates the decrease in signal between two pulses is very limited and the determination of the lifetime from the fit to a single exponential is rather inaccurate. With the presently used VUV laser with a much lower repetition rate (typically 100 Hz) the luminescence lifetimes can be accurately determined in the μs-ms range. We therefore believe that the values for the lifetimes in table 2.3 are more reliable than previously reported values.

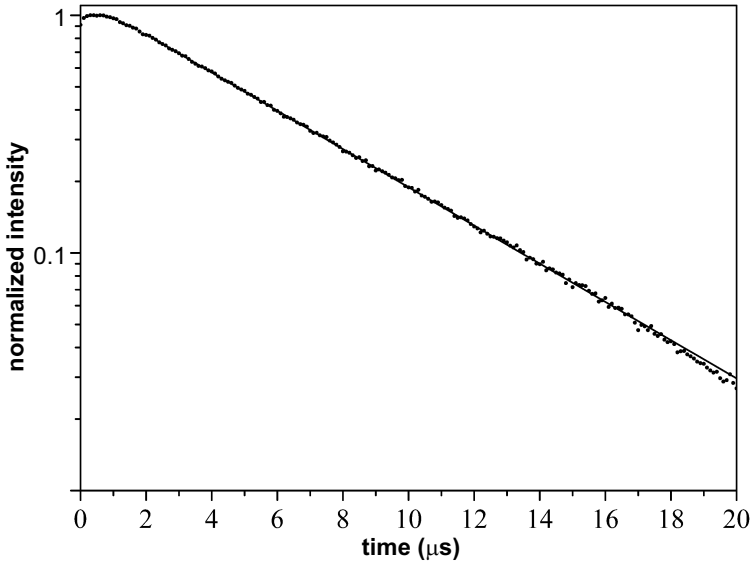

Figure 2.10: Luminescence decay curve of the spin-forbidden $4f^{10}5d \rightarrow 4f^{11}$ emission at 168 nm of $LiYF_4$:Tm^{3+} upon excitation at 157 nm at 10 K. The dots give the measured time dependence of the luminescence intensity and the drawn line gives the best fit to a single exponential decay with $\tau = 5.4\ \mu s$. Note that the vertical axis is a logarithmic scale.

Since the $4f^{n-1}5d \rightarrow 4f^n$ transitions are parity-allowed electric dipole transitions it is relatively simple to calculate the radiative transition probability. Using equation (2.8) and the parameter values from tables 2.1 and 2.2 the radiative decay rates were determined using radial integrals $\langle 5d|r|4f\rangle$ tabulated in table 2.3. The general trend in the decay times is well reproduced by the calculation and also the order of magnitude is correct. However, the experimentally obtained decay times are a factor of three lower than the calculated values. It is at this moment not clear what causes the difference. Most probably it is related to the radial integrals $\langle 5d|r|4f\rangle$.

The transition probabilities are very sensitive to small changes in this integral. The radial integrals are calculated for the free-ion using Cowan's program [25]. In the crystal the radial integral will change due to covalency effects and this may explain the difference between calculated and experimentally observed luminescence decay times. For YPO_4:Er^{3+} the shortening of the life time observed may also be partly due to fast non-radiative decay from the lowest high-spin $4f^{10}5d$ level to the $^2F(2)_{7/2}$ level of erbium. The energy difference in the order of 5000 $cm^{-1}$is approximately five times the maximum phonon energy in YPO_4 and multi-phonon relaxation from the lowest high-spin $4f^{10}5d$ level to the $^2F(2)_{7/2}$ level is expected [34].

Table 2.3: Radial integrals $\langle 5d|r|4f\rangle$ and calculated and experimentally observed lifetimes for the spin-forbidden emissions of Er^{3+} and Tm^{3+} in $LiYF_4$ and YPO_4.

	Wavelength (nm)	τ_{exp} (μs)	τ_{calc} (μs)	$\langle 5d\|r\|4f\rangle$ [25] Å
$LiYF_4$:Er^{3+}	167	2.4	4.2	0.304
YPO_4:Er^{3+}	170	1.0	3.4	0.304
$LiYF_4$:Tm^{3+}	168	5.4	13.1	0.291

2.5 Conclusion

High resolution $4f^{n-1}5d \rightarrow 4f^n$ emission spectra of Pr^{3+}, Nd^{3+}, Er^{3+}, and Tm^{3+} in $LiYF_4$ and YPO_4 have been measured and were compared with calculated emission spectra using a recently developed model for $4f^{n-1}5d$ states. The emission spectra show a well-resolved fine structure with sharp zero-phonon lines and, especially in the YPO_4 host lattice, vibronic lines. In general a good agreement between calculation and experiment was found for the relative intensities and energies of zero-phonon lines corresponding to $4f^{n-1}5d \rightarrow 4f^n$ transitions to the lower energy $4f^n$ states. Luminescence lifetimes for the spin-forbidden $4f^{n-1}5d \rightarrow 4f^n$ emissions were calculated and found to be longer than the experimentally observed lifetimes.

References

[1] R. T. Wegh, H. Donker, K. D. Oskam, and A. Meijerink, Science **283**, 663 (1999).

[2] B. Liu *et al.*, Journal of Luminescence **101**, 155 (2003).

[3] H. Kondo, T. Hirai, and S. Hashimoto, Journal of Luminescence **108**, 59 (2004).

[4] N. Kodama and Y. Watanabe, Applied Physics Letters **84**, 4141 (2004).

[5] V. Babin, K. Oskam, P. Vergeer, and A. Meijerink, Radiation Measurements **38**, 767 (2004).

[6] P. Dorenbos, Journal of Luminescence **91**, 155 (2000).

[7] L. van Pieterson, R. T. Wegh, A. Meijerink, and M. F. Reid, Journal of Chemical Physics **115**, 9382 (2001).

[8] N. M. Khaidukov *et al.*, Optics Communications **184**, 183 (2000).

[9] M. True *et al.*, Journal of Alloys and Compounds **374**, 36 (2004).

[10] V. N. Makhov *et al.*, Surface Review and Letters **9**, 271 (2002).

[11] M. Kirm *et al.*, Radiation Effects and Defects in Solids **157**, 911 (2002).

[12] D. N. Karimov *et al.*, Optical Materials **16**, 437 (2001).

[13] V. N. Makhov *et al.*, Journal of Luminescence **87-89**, 1005 (2000).

[14] R. T. Wegh, E. V. D. van Loef, and A. Meijerink, Journal of Luminescence **90**, 111 (2000).

[15] Y. Chen *et al.*, Pysica Status Solidi B **240**, R1 (2003).

[16] L. van Pieterson *et al.*, Physical Review B **65**, 045113/1 (2002).

[17] L. van Pieterson, M. F. Reid, G. W. Burdick, and A. Meijerink, Physical Review B **65**, 045114/1 (2002).

[18] W. T. Carnall, G. L. Goodman, K. Rajnak, and R. S. Rana, Journal of Chemical Physics **90**, 3443 (1989).

[19] C. Görller-Walrand and K. Binnemans, *Rationalization of crystal-field parametrization* (PUBLISHER, ADDRESS, 1996), Vol. 23, pp. 121–283.

[20] C. Görller-Walrand and K. Binnemans, *Spectral intensities of f-f transitions* (PUBLISHER, ADDRESS, 1998), Vol. 25, pp. 101–264.

[21] B. Henderson and G. F. Imbusch, *Optical Spectroscopy of Inorganic Solids* (Clarendon Press, Oxford, 1989).

[22] O. Guillot-Noel, B. Bellamy, B. Viana, and D. Gourier, Physical Review B **60**, 1668 (1999).

[23] G. F. Imbush and R. Copelman, *Laser Spectroscopy of Solids* (Springer, New York, 1981).

[24] B. G. Wybourne, *Spectroscopic Properties of Rare Earths* (Interscience Publishers, New York, 1965).

[25] R. D. Cowan, *The Theory of Atomic Structure and Spectra* (University of California, Berkeley, 1981).

[26] G. W. Burdick and F. S. Richardson, Chemical Physics **228**, 81 (1998).

[27] T. Hayhurst *et al.*, Journal of Chemical Physics **76**, 3960 (1982).

[28] A. A. S. da Gama, G. F. de Sá, P. Porcher, and P. Caro, Journal of Chemical Physics **75**, 2583 (1981).

[29] M. A. Couto dos Santos *et al.*, Journal of Alloys and Compounds **275-277**, 435 (1998).

[30] T. Hayhurst *et al.*, Journal of Chemical Physics **74**, 5449 (1981).

[31] H. P. Jenssen, A. Linz, C. A. Leavitt, R. P. Morrison, and D. E. Wortman, Physical Review B **11**, 92 (1975).

[32] M. F. Reid, L. van Pieterson, R. T. Wegh, and A. Meijerink, Physical Review B **62**, 14744 (2000).

[33] G. M. Williams *et al.*, Physical Review B **40**, 4132 (1989).

[34] R. T. Wegh, W. van Klinken, and A. Meijerink, Physical Review B **64**, 045115 (2001).

Chapter 3

Time and temperature dependence of the emissions from the quantum cutting phosphor $LiGdF_4:Eu^{3+}$

The Gd-Eu couple is well known for efficient conversion of absorbed high-energy photons into two visible photons (quantum cutting). For this couple, a model describing the quantum-cutting mechanism has been proposed by Wegh et al. *[1]. This model is mainly supported by emission spectra, while the kinetics of the energy-transfer processes involved in quantum cutting have hardly been investigated. The present chapter reports time and temperature dependent studies of the spectroscopic properties of $LiGdF_4:Eu^{3+}$ 0.5%. The experimentally observed decay curves at room temperature of the Eu^{3+} $^5D_0$, $^5D_1$ and Gd^{3+} $^6P_{7/2}$ emission can be explained by a parameter model based on the kinetics of the mechanism. The temperature-dependent study shows a change in the energy-transfer kinetics that is consistent with the absence of quantum cutting at low temperatures ($T < 50$ K).*

3.1 Introduction

There is an increasing demand for efficient vacuum-ultraviolet (VUV, $\lambda < 200$ nm) phosphors for application in plasma display panels and mercury-free fluorescent tubes based on a Xe discharge. The 90% quantum efficiency of the present generation of VUV phosphors leaves room for improvement. The short-wavelength excitation light of the Xe discharge has enough energy to obtain two visible photons for each VUV photon absorbed. This process is generally known as quantum cutting.

In 1974 Piper *et al.* [2] and Sommerdijk *et al.* [3] reported on the first quantum-cutting phosphor. In their materials the Pr^{3+} ion shows a cascade emission, converting VUV radiation into 405 and 480 nm photons with a visible quantum efficiency of 140%. The Pr^{3+} cascade emission is not used in lighting applications since 405 nm radiation has a too low color rendering index.

A more recent discovery is quantum cutting by downconversion. In this concept two ions are used to split the excitation energy. A well-known example is the Gd-Eu couple, for which efficient quantum-cutting has been demonstrated in a number of fluoride lattices [4–8].

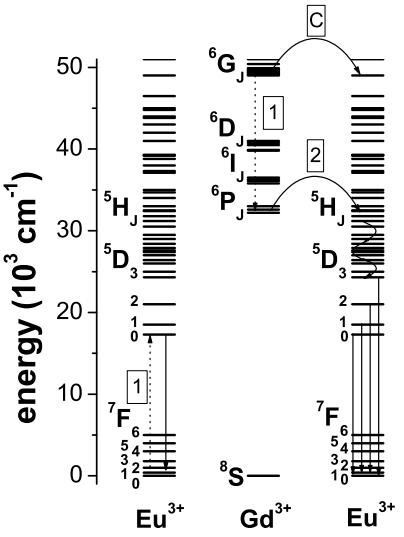

Figure 3.1: Energy-level diagram for the Gd^{3+}-Eu^{3+} system, showing the possibility for cross relaxation (denoted by 1): $Gd^{3+}(^6G_J)$, Eu^{3+} $(^7F_1) \rightarrow Gd^{3+}(^6P_J)$, Eu^{3+} $(^5D_0)$. Subsequent energy transfer (denoted by 2) occurs from $Gd^{3+}(^6P_J)$ to Eu^{3+} (^5H_J). Energy transfer from $Gd^{3+}(^6G_J)$ to a high energy level of Eu^{3+} is denoted by C.

A model for the quantum-cutting mechanism has been proposed by Wegh *et al.* [1] (see figure 3.1). After excitation in the Gd^{3+} ^6G_J levels, partial energy transfer to Eu^{3+} by cross relaxation takes place: Gd^{3+} ^6G_J, Eu^{3+} $^7F_1 \rightarrow Gd^{3+}$ ^6P_J, Eu^{3+} $^5D_0$, denoted 1 in figure 3.1. This yields one photon from the Eu^{3+} $^5D_0 \rightarrow {}^7F_J$ transition. Note that the cross-relaxation step is thermally activated [1]. There is no spectral overlap between the Eu^{3+} $^7F_0 \rightarrow {}^5D_0$ transition and Gd^{3+} $^6G_{7/2} \rightarrow {}^6P_J$ transitions, which prevents cross relaxation at low temperatures. After the cross-relaxation step, the remaining energy on Gd^{3+} is transferred in a second energy-transfer step from Gd^{3+} ^6P_J to Eu^{3+}, denoted 2 in figure 3.1, which yields the second photon from a Eu^{3+} $^5D_J \rightarrow {}^7F_J$ transition. The process denoted C in figure 3.1 stands for single-step energy transfer from Gd^{3+} ^6G_J to Eu^{3+}. After this energy-transfer step relaxation to the Eu^{3+} ^5D_J levels takes place and only one photon is emitted for each VUV photon absorbed. This process competes with cross relaxation and the ratio of the two processes determines the intrinsic quantum efficiency.

In previous studies, quantum cutting has been demonstrated by studying emission and excitation spectra. In case of quantum cutting, an increase in the intensity of the Eu^{3+} $^5D_0 \rightarrow {}^7F_J$ emission to the $^5D_1 \rightarrow {}^7F_J$ emission is observed upon excitation in the Gd^{3+} ^6G_J levels [4–8].

The analysis of the emission spectra gives insight in the quantum-cutting process via time-integrated luminescence and no information is obtained on the kinetics of the energy-transfer processes involved. After Gd^{3+} ^6G_J excitation, a relatively fast increase in the time-resolved signal of the Eu^{3+} $^5D_0$ emission is expected as compared to the increase in the $^5D_1$ emission intensity, since the $^5D_0$ level is populated directly in the cross-relaxation step. Kondo and coworkers have done time-dependent luminescence studies on the Eu^{3+} $^5D_{1,0} \rightarrow {}^7F_J$ emission in $NaGdF_4$:Eu^{3+} and have observed this [6]. However, upon excitation into the ^6I_J levels of Gd^{3+} the Eu^{3+} ^5D_J emissions show a strong instant signal which is in contradiction with the kinetics of the quantum-cutting model.

In this work the dynamics of the Gd^{3+} ^6P_J, Eu^{3+} $^5D_1$ and the Eu^{3+} $^5D_0$ emissions are investigated for $LiGdF_4$:Eu^{3+}. A parameter model based on the mechanisms described in figure 3.1 is used to fit to room-temperature decay curves of the Eu^{3+} emissions. A good agreement would provide further proof for the downconversion mechanisms as proposed in the quantum-cutting model and provide information on the kinetics of the steps involved. Also, temperature dependent spectra and decay curves are measured for the Gd^{3+} ^6G_J, ^6P_J, and the Eu^{3+} $^5D_1$ and $^5D_0$ emissions. Cross relaxation is expected to be absent at low temperatures (< 50 K [1]) and thus a change in the luminescence decay properties is expected as a function of temperature.

3.2 Experimental

A powder sample was prepared by firing stoichiometric mixtures of LiF, GdF_3 and 0.5% EuF_3 at 550 °C in a nitrogen atmosphere. The sample was checked by X-ray diffraction and found to be single phase. $LiGdF_4$ is isostructural to $LiYF_4$, which has the inverse scheelite structure, space group $I4_{1/a}$.

For emission spectra at room temperature (RT) a SPEX DM-3000F spectrofluorometer adapted for the VUV was used [9]. The excitation source is a D_2-lamp (Hamamatsu L1835, 150 W). The excitation and emission light are both dispersed by double 0.22 m gratings (SPEX 1680, 1200 l/mm) blazed at 150 nm for the excitation light and at 500 nm for the emission light.

Decay curves at RT were measured with the use of two excitation sources. For excitation in Gd^{3+} ^6P_J levels a Lambda Physik LPD3000 tunable dye laser filled with a Rhodamine B dye solution was used. Radiation with a wavelength of 311.4 nm was created by second-harmonic generation of the dye-laser output with a KDP crystal. The dye laser was pumped by a Lambda Physik LPX100 excimer (XeCl) laser. For excitation in the Gd^{3+} ^6G_J levels a fluoride excimer laser (ExciStar S-200, Tuilaser) filled with an argon/fluorine gas mixture was used. The excitation wavelength is 193 nm and the pulse duration is typically 10 ns. Emission light was dispersed by an Acton Research monochromator (Scientific SpectraPro, 150 l/mm grating, blazed at 500 nm with 0.300 m focal length) and detected by a RCA C31034 photo multiplier tube (PMT). The signal from the PMT was amplified by an operational amplifier (10^4, response ~ 2 μs) and then registered with a Tektronix 2440 digital oscilloscope.

Temperature-dependent emission spectra and decay curves were measured with the fluoride excimer laser as excitation source (argon/fluorine gas mixture, 193 nm). The emission from the sample was dispersed by a 1200 l/mm grating (Jobin Yvon, Triax 550, blazed at 450 nm) and detected with a Hamamatsu R928 PMT. The signal from the PMT was amplified by an operational amplifier (10^4, response ~ 2 μs) and then registered with a Tektronix 2440 digital oscilloscope. Control over the temperature from 30 K to RT was achieved by mounting the sample on an Oxford Instruments Optistat$^{CF\text{-}V}$ liquid-helium cold-finger cryostat connected to an Oxford Intelligent Temperature Controller (ITC4). The temperature sensor of the temperature controller is mounted at the end of the cold finger and the measured temperature deviates from the actual temperature of the sample. The temperature of the sample was determined by comparing the Boltzman populations from the Stark levels of the Gd^{3+} $^6P_{7/2} \rightarrow {}^8S_{7/2}$ transition. For this purpose, high-resolution emission spectra were obtained in the wavelength region of 310.6 to 311.6 nm, with the use of a 3600 l/mm grating (Jobin Yvon, Triax 550) blazed for the VUV/UV.

3.3 Results and Discussion

3.3.1 Spectroscopy and kinetics of quantum cutting at room temperature

Evidence for quantum cutting in Gd-Eu couples is commonly obtained by comparison of emission spectra at different excitation wavelengths. When excitation is into the Gd^{3+} ^6P_J, ^6I_J, or ^6D_J levels, a single energy-transfer step to Eu^{3+} occurs and the 'normal' branching ratio for the Eu^{3+} ^5D_J emission is obtained. This branching ratio is also observed after excitation of a high-energy Eu^{3+} energy level. It is determined by multi-phonon relaxation from the $^5D_3$ level to the lower-energy ^5D_J levels and, depending on the Eu^{3+} concentration, by cross relaxation between Eu^{3+} ions. An emission spectrum upon excitation in Gd^{3+} ^6P_J is plotted in figure 3.2.a. The plot

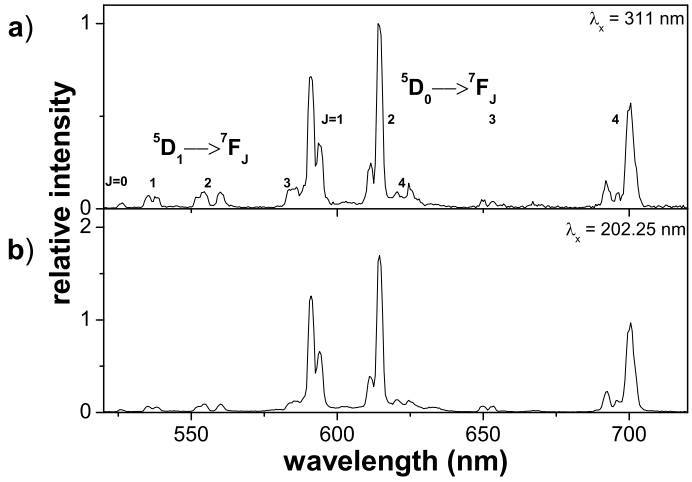

Figure 3.2: Emission spectra (RT) of the Eu^{3+} $^5D_{1,0}$ emissions upon excitation into the Gd^{3+} ^6P_J levels (a) and into the Gd^{3+} ^6G_J levels (b).

shows the Eu^{3+} $^5D_1$ and $^5D_0$ emissions. The same peaks were observed in previous work and they are assigned accordingly [1]. The spectrum is normalized to the Eu^{3+} $^5D_0 \rightarrow {}^7F_2$ emission peak. Figure 3.2.b shows the same emissions, but after excitation in Gd^{3+} ^6G_J. In order to show the effect of quantum cutting, the spectrum is scaled to the Eu^{3+} $^5D_1$ emission in figure 3.2.a. The Eu^{3+} $^5D_0$ emissions have increased in intensity upon excitation in Gd^{3+} ^6G_J. The higher relative intensity of the $^5D_0$ emission lines in this scaled spectrum is the effect of the cross-relaxation step in figure 3.1. In this step only the Eu^{3+} $^5D_0$ level is populated, which leads to an increase of the $^5D_0$ emission after Gd^{3+} ^6G_J excitation.

The cross-relaxation efficiency can also be calculated from the emission spectra

shown in figure 3.2 according to the equation proposed by Wegh *et al.* [1],

$$\frac{p_1}{p_1 + p_C} = \frac{R(^5D_0/^5D_{1,2,3})_{^6G_J} - R(^5D_0/^5D_{1,2,3})_{^6P_J}}{R(^5D_0/^5D_{1,2,3})_{^6P_J} + 1}. \tag{3.1}$$

Here, p_1 and p_C are the probabilities for cross relaxation and direct energy transfer from Gd^{3+} ^6G_J to Eu^{3+}, and $R(^5D_0/^5D_{1,2,3})_{^6G_J}$ and $R(^5D_0/^5D_{1,2,3})_{^6P_J}$ are the $^5D_0/^5D_{1,2,3}$ emission intensity ratios upon ^6G_J excitation and upon ^6P_J excitation. Evaluation of equation (3.1) gives a cross-relaxation probability of 58%. This means that the quantum efficiency is 158%. This value is lower than the value of 190% reported by Wegh *et al.* [1]. The lower efficiency of this sample is probably caused by defects in the sample. A defect emission is observed at low temperatures (see below).

Time-dependent measurements, with fits included, are shown in figure 3.3. In figure 3.3.a the time-dependent traces are shown for the Eu^{3+} $^5D_1$ emission upon excitation in Gd^{3+} ^6P_J (triangles) and in Gd^{3+} ^6G_J (squares). Figure 3.3.b shows the time-dependent traces for the Eu^{3+} $^5D_0$ emission upon excitation in Gd^{3+} ^6P_J (triangles) and in Gd^{3+} ^6G_J (squares). The shape of the curves can be understood from the kinetics of the downconversion model described in figure 3.1 when a fast migration regime is assumed [10]. In the fast migration regime, the inter-Gd energy transfer is much faster than Gd-Eu energy transfer. Energy migration over Gd^{3+} ^6P_J levels in $LiGdF_4$ has been investigated and found to be a fast process ($10^{7\pm1}$ s^{-1} per Gd-Gd energy-transfer step) [11,12]. In this case, the inter-Gd energy migration, subsequent Gd-Eu energy transfer and fast multi-phonon relaxation on the Eu^{3+} ion can be described by one effective energy-transfer rate from Gd^{3+} $^6P_{7/2}$ to Eu^{3+} $^5D_1$. With this assumption, the following set of coupled differential rate equations is used to describe relaxation after Gd^{3+} ^6P_J excitation,

$$\begin{aligned} \frac{\mathrm{d}n_1}{\mathrm{d}t} &= \gamma_P n_P - \gamma_1 n_1 \\ \frac{\mathrm{d}n_0}{\mathrm{d}t} &= \gamma_1 n_1 - \gamma_0 n_0. \end{aligned} \tag{3.2}$$

In equation (3.2) n_1 stands for the population of Eu^{3+} ions in the $^5D_1$ excited state, n_P stands for the population of Gd^{3+} ions in the ^6P_J excited state and n_0 stands for the population of Eu^{3+} ions in the $^5D_0$ excited state. The effective rate constant for relaxation from Gd^{3+} ^6P_J to Eu^{3+} $^5D_1$ is denoted by γ_P, the rate constant for (radiative and non-radiative) decay from the Eu^{3+} $^5D_1$ level is given by γ_1 and the rate constant for radiative decay from the Eu^{3+} $^5D_0$ level by γ_0. In equation (3.2) the time dependence of the $^5D_1$ emission is described by a feeding and decaying term, with feeding from the Gd^{3+} ^6P_J levels. The resulting curve accurately describes the experimental curve in figure 3.3.a. The values for γ_P (1783 s^{-1}) and γ_1 (778 s^{-1}) obtained from this fit were fixed at these values when subsequent rate equations were used for fitting. The time dependence of the population of the Eu^{3+} $^5D_0$ level

is coupled to the time dependence of the population of the Eu^{3+} $^5D_1$ level since in equation (3.2) the $^5D_0$ level is fed by the $^5D_1$ level. The fit shows good agreement with the shape of the experimental curve in figure 3.3.b when γ_0 is equal to 148 s^{-1}.

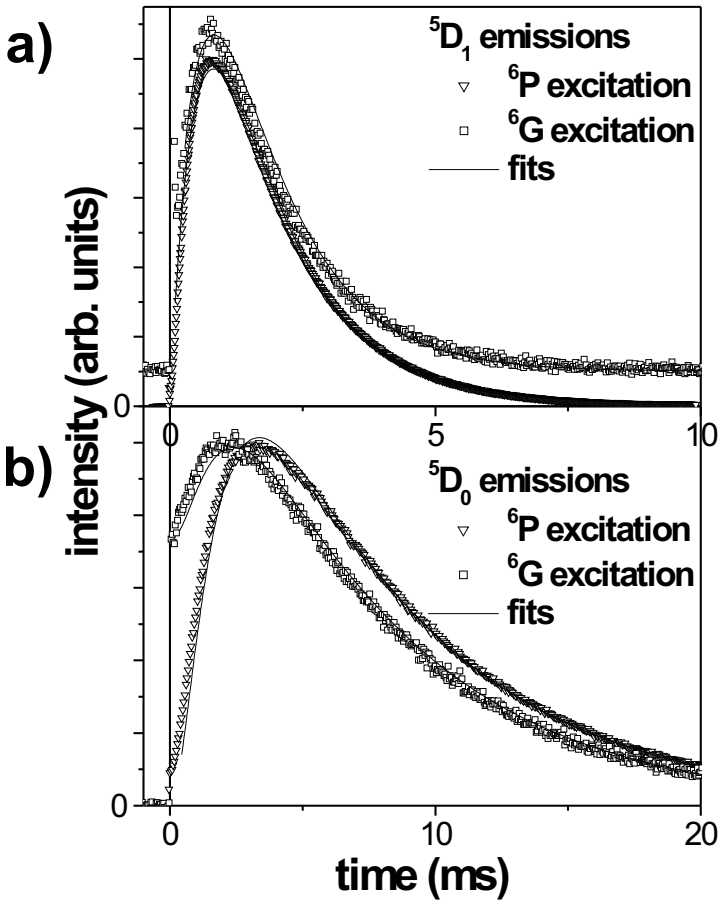

Figure 3.3: a) Time-resolved intensity of the $^5D_1$ emission (RT, 552 nm) for excitation into Gd^{3+} ^6P_J (311 nm, triangles) or into Gd^{3+} ^6G_J (193 nm, squares). The decay curve after ^6G excitation is shifted along the y-axis. b) Time-resolved intensity of the $^5D_0$ emission (RT, 700 nm) for excitation into Gd^{3+} ^6P_J (311 nm, triangles) or into Gd^{3+} ^6G_J (193 nm, squares). Note the different time scales. Solid lines are fits to the experimental curves (see text).

Relaxation after Gd^{3+} ^6G_J excitation is described by a similar set of coupled

differential rate equations,

$$\begin{aligned} \frac{\mathrm{d}n_P}{\mathrm{d}t} &= \gamma_G n_G - \gamma_P n_P \\ \frac{\mathrm{d}n_1}{\mathrm{d}t} &= \gamma_P n_P - \gamma_1 n_1 \\ \frac{\mathrm{d}n_0}{\mathrm{d}t} &= \gamma_G n_G + \gamma_1 n_1 - \gamma_0 n_0, \end{aligned} \tag{3.3}$$

where γ_G denotes the effective cross-relaxation rate that feeds both the $^5D_0$ level of Eu^{3+} and the ^6P levels of Gd^{3+}. When the two sets of coupled differential rate equations (equations 3.2 and 3.3) are compared, it is noted that upon Gd^{3+} ^6G_J excitation one equation is added, which describes the time dependence of the population of the Gd^{3+} ^6P_J levels. This is due to the fact that the Gd^{3+} ^6P_J levels are now fed by Gd^{3+} ^6G_J levels in the cross-relaxation step. In the experiment (figure 3.3.a) the measured decay curve for the Eu^{3+} $^5D_1$ emission after Gd^{3+} ^6G_J excitation is almost identical to the one obtained after Gd^{3+} ^6P_J excitation. This shows that cross relaxation is a much faster process than energy transfer from Gd^{3+} ^6P_J to Eu^{3+} $^5D_1$ (otherwise the feeding of the $^5D_1$ emission would be slower due to the cross-relaxation step which feeds the ^6P level). This is to be expected since the effective rate constant for the Gd^{3+} $^6P_J \rightarrow Eu^{3+}$ energy transfer includes the relatively slow non-radiative relaxation processes to the $^5D_1$ level on the Eu^{3+} ion.

As a consequence of the fast cross-relaxation step, when monitoring the decay of the Eu^{3+} $^5D_0$ emission upon Gd^{3+} ^6G_J excitation an instant signal is expected due to fast feeding of the $^5D_0$ level through cross relaxation. This is exactly what is observed in the experimental results shown in figure 3.3.b. The fit to the Eu^{3+} $^5D_0$ emission curve is done with all transition rates obtained from fits to the previous curves. The theoretical curve predicts the rise-time and the appearance of the instantaneous signal accurately. This gives a good indication that the model used is appropriate. Also, the theoretical curve reproduces the ratio between the instant signal and the rising signal in the experiment remarkably well. However, the good agreement on this point is somewhat fortuitous since the model contains two simplifications which influences seem to cancel each other. In the model, it is assumed that the cross-relaxation efficiency is 100%, leading to an increased contribution of the instantaneous signal as compared to the experiments. However, the model also assumes no radiative and non-radiative losses for the build-up component of the $^5D_0$ emission, leading to an increased contribution of the rising signal as compared to the experiment. Apparently, these two effects cancel each other.

The decay rates obtained are listed in table 3.1. The value of 1783 s^{-1} for γ_P mainly reflects the non-radiative relaxation processes on the Eu^{3+} ion. The (non-radiative) energy-transfer rate from the Gd^{3+} ^6P_J levels is found to be much faster: 1.7×10^4 s^{-1} (see below). The radiative decay rate for the Eu^{3+} $^5D_0$ emission is slow for a $4f^n \rightarrow 4f^n$ transition. It corresponds to a lifetime of 6.7 ms, which is in agreement with the lifetime obtained after direct excitation into the $^5D_0$ level and slightly lower

Table 3.1: Parameter values obtained for the rate constants in equations (3.2) and (3.3) from fits to the luminescence decay curves in figure 3.3. The numbers between brackets give the statistical 95% confidence interval. The solid lines in figure 3.3 show the decay curves obtained based on the parameter values.

	From	To	γ (s^{-1})
γ_P	$Gd^{3+}\ {}^6P_J$	$Eu^{3+}\ {}^5D_1$	1783 (30)
γ_G	$Gd^{3+}\ {}^6G_J$	$Gd^{3+}\ {}^6P_J$	$> 5 \times 10^4$
γ_1	$Eu^{3+}\ {}^5D_1$	-	778 (10)
γ_0	$Eu^{3+}\ {}^5D_0$	-	148 (2)

than the 7.3 ms obtained by others [13]. The confidence margins are 95% statistical confidence margins based on the fitting process. They give an indication of the quality of the fits. It is known that differences in the detection methods limit the accuracy of obtained decay rates to some 10%. The same detection equipment was used to obtain the four decay curves discussed above.

3.3.2 Temperature dependence

Apart from the kinetics, also the temperature dependence of the Gd-Eu quantum-cutting system is worth studying. Due to a mismatch in energy, energy transfer by cross relaxation is expected to be inefficient at low temperatures and changes in the visible spectra as a function of temperature have been observed [1]. The ${}^7F_0 \rightarrow {}^5D_0$ energy difference is slightly ($\sim$ 250 cm^{-1}) larger than the ${}^6G_{7/2} \rightarrow {}^6P_{7/2}$ energy difference and phonon-assisted energy transfer or thermal population of the the Eu^{3+} ${}^7F_1$ state or the higher crystal-field levels of the $Gd^{3+}\ {}^6G_{7/2}$ state is needed to overcome the mismatch. In figure 3.4 emission spectra are shown from 200 to 620 nm at various temperatures. All graphs are scaled on the $Eu^{3+}\ {}^5D_0 \rightarrow {}^7F_1$ emission at 590.5 nm. At low temperatures, a defect band emission is observed in the blue spectral region. The presence of defects reduces the quantum efficiency of this phosphor.

In the red spectral region, Eu^{3+} emission lines are observed at all temperatures and the four dominant peaks at RT are assigned to $Eu^{3+}\ {}^5D_0$ emissions. When the temperature is decreased below 100 K more peaks around 592 nm start to appear. These are assigned to $Gd^{3+}\ {}^6G_J \rightarrow {}^6P_J$ emission lines [1]. They are most apparent at the lowest temperatures. The presence of the $Gd^{3+}\ {}^6G_{7/2}$ emission can be explained by less efficient cross-relaxation. The thermally activated cross-relaxation process is inhibited at low temperatures. At temperatures higher than 100 K the ${}^7F_1$ level of Eu^{3+} and the Stark levels of the ${}^6G_{7/2}$ level of Gd^{3+} become sufficiently thermally populated to allow for efficient cross relaxation.

Furthermore, at short wavelengths ($\sim$ 204 nm), $Gd^{3+}\ {}^6G_{7/2} \rightarrow {}^8S_{7/2}$ emissions

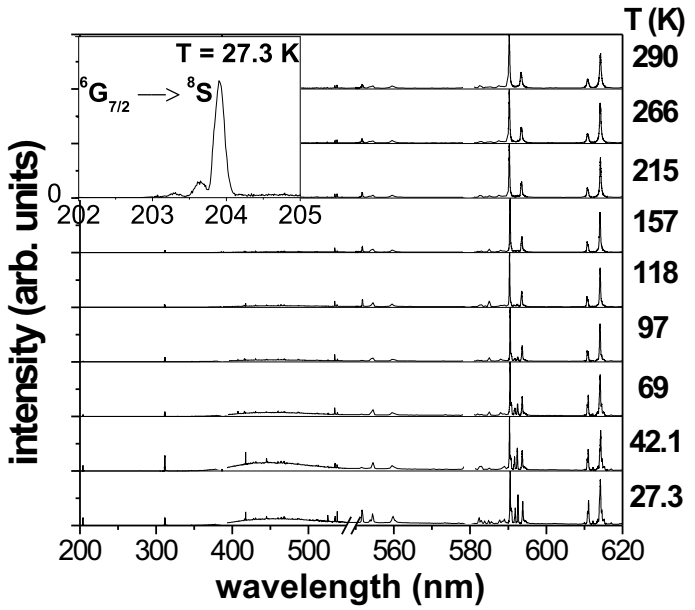

Figure 3.4: Emission spectra of $LiGdF_4$:Eu^{3+} 0.5% at various temperatures (λ_x = 193 nm). The reflection of the laser radiation in second (around 386 nm) and third (around 579 nm) order were removed from the spectra. Note the change in wavelength scale. The inset shows the Gd^{3+} $^6G_{7/2} \rightarrow {}^8S_{7/2}$ emission at 27.3 K.

are observed at low temperatures. The inset shows the Gd^{3+} $^6G_{7/2} \rightarrow {}^8S_{7/2}$ emission spectrum at 27.3 K. Three peaks are observed at 203.30, 203.64 and 203.90 nm, corresponding to emissions from the different $^6G_{7/2}$ stark levels. The positions are consistent with the energies calculated and observed for the $^6G_{7/2}$ crystal-field levels from excitation spectra [9].

While the relative intensity of the Gd^{3+} ^6G_J emissions show a strong decrease with increasing temperature, the intensity of the Gd^{3+} ^6P_J emission (311 nm) rises when the temperature is increased betweeen 25 and 50 K and then decreases monotonously when the temperature is increased further. The rise is explained by increased feeding from the Gd^{3+} ^6G_J levels by the thermally activated cross-relaxation process, while energy migration over the $^6P_{7/2}$ levels leading to Gd^{3+} ($^6P_{7/2}$) $\rightarrow$ Eu^{3+} energy transfer is still inefficient. When the temperature is increased further, both energy-transfer steps become more efficient, leading to a decrease in ^6G_J and ^6P_J emission intensity and fast energy transfer to Eu^{3+}.

Overall, the temperature dependent emission spectra are in agreement with quantum cutting by a temperature-activated cross-relaxation process. Cross relaxation

becomes efficient when the temperature is raised above 100 K. At lower temperatures Gd^{3+} $^6G_{7/2}$ emission is observed.

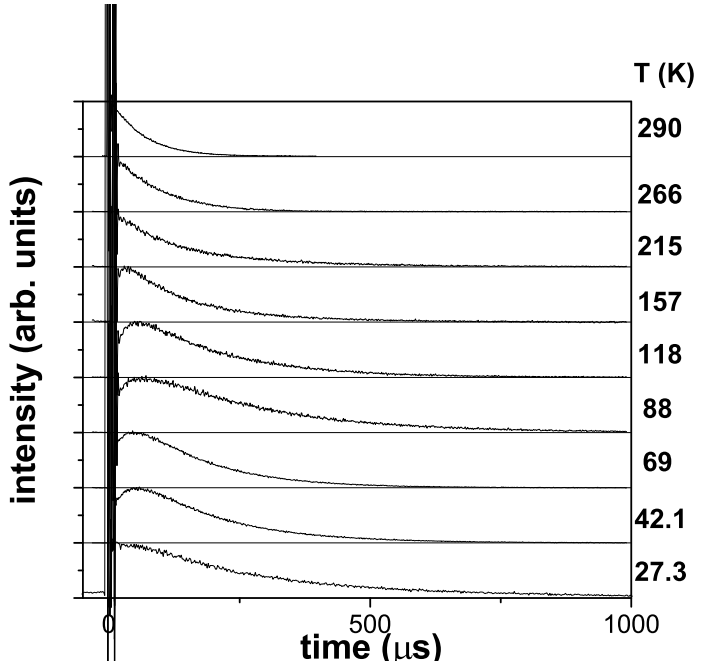

Figure 3.5: Decay curves at various temperatures of the Gd^{3+} ^6P_J emission (λ_x = 193 nm, λ_m = 311 nm).

Next, temperature-dependent luminescence decay curves will be discussed in a qualitative manner. The increased influence of competing processes and the slowed-down energy migration at low temperatures inhibits a quantitative analysis due to the relatively large extension in parameters needed to describe the additional processes.

Temperature dependent decay curves of the Gd^{3+} ^6P_J emission are shown in figure 3.5. The oscillations at short times are due to instrumental response to a fast signal.

The luminescence decay curves reflect the qualitative discussion on the temperature dependence of the ^6P_J emission intensity. At the lowest temperature, the ^6P_J emission shows a decaying signal with a lifetime of 260 μs with a small feeding term. This lifetime is much faster than the radiative lifetime of 8.7 ms [11], which shows that migration and energy transfer is already present. When the temperature is raised to 42.1 K the feeding component becomes remarkably more pronounced in the decay curve. This component is attributed to cross relaxation from the Gd^{3+} $^6G_{7/2}$ level, which is in agreement with the observations in the emissions spectra. When the temperature is increased further, a feeding component is still apparent up

to 157 K while the time to reach the maximum of the decay curve shifts to shorter times. This reflects an increase in the cross-relaxation rate from the Gd^{3+} $^6G_{7/2}$ level and the energy-transfer rate from the $^6P_{7/2}$ level. For higher temperatures, a single-exponential decay function is measured. The observations are explained by more efficient feeding through cross-relaxation and more efficient energy migration over the Gd^{3+} ^6P_J levels as the temperature is increased, which agrees with the quantum-cutting model. The room-temperature lifetime of the ^6P_J emission is 60 μs.

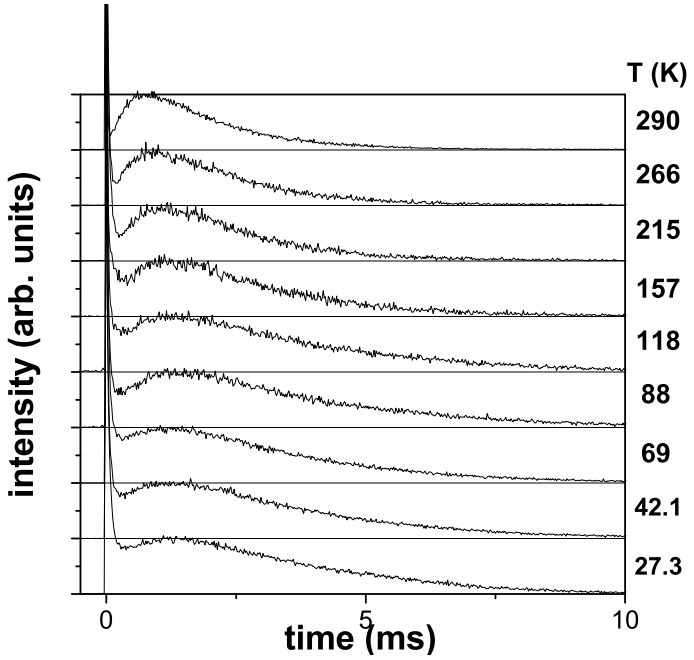

Figure 3.6: Decay curves at various temperatures of the Eu^{3+} $^5D_1$ emission (λ_x = 193 nm, λ_m = 552 nm).

The temperature-dependent decay curves for the Eu^{3+} $^5D_1$ emission are shown in figure 3.6. The large signal at short time intervals is due to instrumental response.

At room temperature, a feeding process is observed in the decay curve, which is explained by non-radiative relaxation from the higher-energy ^5D_J levels. When the temperature is lowered to 100 K, relaxation rates slow down, which is indicated by an increase in the rise time of the signals. When the temperature is lowered further, a large instant intensity and a relatively small feeding term are observed. Since the cross-relaxation probability is reduced at these low temperatures the origin of the large instant signal is attributed to competing processes such as energy transfer via the defect center. When the temperature is increased, quantum cutting becomes more probable and the feeding component becomes more pronounced.

Figure 3.7 shows the decay curves of the Eu^{3+} $^5D_0$ emission at several tempera-

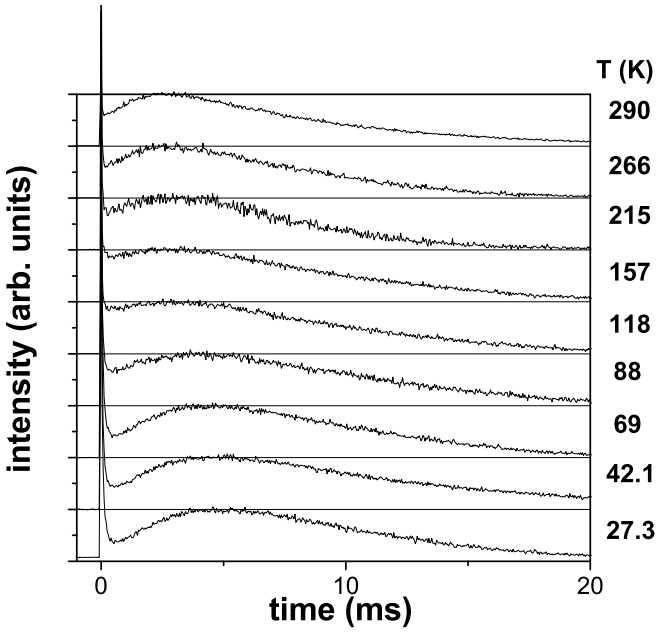

Figure 3.7: Decay curves at various temperatures of the Eu^{3+} $^5D_0$ emission (λ_x = 193 nm, λ_m = 590.5 nm)

tures. The signal at short times is due to instrumental response.

All curves show a feeding component of which the rise time increases when the temperature is lowered. Also, notable changes can be observed in the instantaneous signal of the decay curves as compared to the rise-time signal. From the low-temperature regime, the instantaneous signal is observed to increase when the temperature is increased to 157 K. Then, the feeding term becomes more apparent. The increase in the instantaneous signal can be explained by the enhancement of cross relaxation, which leads to a fast population of the Eu^{3+} $^5D_0$ level. When the temperature is increased further, the feeding term (caused by energy transfer from Gd^{3+} ^6P_J levels to Eu^{3+}) becomes more dominant, resulting in a relative decrease of the instant luminescence signal at temperatures above 157 K. At temperatures lower than 157 K the Eu^{3+} luminescence resulting from Gd^{3+} $^6P_J \rightarrow Eu^{3+}$ energy transfer is less dominant due to slower energy-transfer and multi-phonon relaxation rates.

The decay curves of the Eu^{3+} $^5D_0$ level at various temperatures are in accordance with the decay curves from the Eu^{3+} $^5D_1$ level and the Gd^{3+} ^6P_J levels. They show a strong inhibition of cross relaxation and Gd^{3+} $^6P_{7/2} \rightarrow Eu^{3+}$ energy transfer at low temperatures. Cross relaxation becomes efficient when the temperature reaches 100 K, which agrees with the quantum-cutting model.

3.4 Conclusion

In this study the kinetics of the Gd-Eu downconversion process were investigated by measuring emission spectra and time-dependent luminescence intensities for the Eu^{3+} $^5D_{1,0}$ and Gd^{3+} ^6G_J and ^6P_J emissions upon Gd^{3+} ^6P_J and ^6G_J excitation. Analysis of the room-temperature luminescence decay curves shows that the experimental results can be explained by rate equations based on the downconversion model. A good agreement is obtained between the various decay curves and fitted curves based on parameters for decay rates and energy-transfer rates for the various levels involved. Emission spectra and decay curves were measured as a function of temperature and showed that the cross-relaxation step is temperature activated and becomes efficient at temperatures above 100 K. The present analysis provides more insight in the kinetics of energy-transfer processes in the Gd-Eu quantum-cutting system and the temperature dependence of the energy-transfer processes.

References

[1] R. T. Wegh, H. Donker, K. D. Oskam, and A. Meijerink, Journal of Luminescence **82**, 93 (1999).

[2] W. W. Piper, J. A. DeLuca, and F. S. Ham, Journal of Luminescence **8**, 344 (1974).

[3] J. L. Sommerdijk, A. Bril, and A. W. De Jager, Journal of Luminescence **8**, 341 (1974).

[4] R. T. Wegh, H. Donker, K. D. Oskam, and A. Meijerink, Science **283**, 663 (1999).

[5] B. Liu *et al.*, Journal of Luminescence **101**, 155 (2003).

[6] H. Kondo, T. Hirai, and S. Hashimoto, Journal of Luminescence **108**, 59 (2004).

[7] N. Kodama and Y. Watanabe, Applied Physics Letters **84**, 4141 (2004).

[8] F. You, S. Huang, S. Liu, and Y. Tao, Journal of Luminescence **110**, 95 (2004).

[9] R. T. Wegh *et al.*, Physical Review B **56**, 13841 (1997).

[10] B. Henderson and G. F. Imbusch, *Optical Spectroscopy of Inorganic Solids* (Clarendon Press, Oxford, 1989).

[11] H. S. Kiliaan, A. Meijerink, and G. Blasse, Journal of Luminescence **35**, 155 (1986).

[12] A. J. De Vries, M. F. Hazenkamp, and G. Blasse, Journal of Luminescence **42**, 275 (1988).

[13] J. van Vliet, D. van der Voort, and G. Blasse, Journal of Luminescence **42**, 305 (1989).

Chapter 4

Quenching of Pr^{3+} $^1S_0$ emission by Eu^{3+} and Yb^{3+}

Energy transfer between Pr^{3+} and Eu^{3+} is studied by luminescence spectroscopy and time-resolved measurements. In earlier experiments Zachau et al. *[1] observed no energy transfer from the $^1S_0$ level of Pr^{3+} to the $^5D_3$ level of Eu^{3+} for YF_3:Pr, Eu in spite of the favorable spectral overlap for energy transfer. This unexpected result was not explained. To resolve this issue, first the critical distance for energy transfer using the Förster theory is calculated and it is shown that efficient energy transfer between Pr^{3+} and nearest Eu^{3+} neighbors is predicted. Nevertheless, luminescence experiments show no Eu^{3+} emission upon excitation in the $^1S_0$ level of Pr^{3+} in YF_3:Pr, Eu confirming the results in [1]. The experiments do show a strong quenching of the $^1S_0$ emission by Eu^{3+}. The quenching is explained by a low-energy metal-to-metal charge-transfer state (Pr^{4+}-Eu^{2+}) for Pr-Eu pairs. Additional support for this quenching mechanism is provided by the observation that also addition of Yb^{3+} leads to quenching of the $^1S_0$ emissions.*

4.1 Introduction

Higher energy efficiencies for the conversion of high-energy radiation into visible light can be obtained by the use of quantum-cutting phosphors. A quantum-cutting phosphor is a material that is capable of emitting two visible photons for every (vacuum-)ultraviolet photon absorbed. The discovery of such phosphors [2–5] has been an exciting development in the field of luminescence research.

The discovery of quantum-cutting systems started with the finding of single ions capable of a cascade emission such as Pr^{3+} [2, 3], Tm^{3+} [6] and Gd^{3+} [7]. The Pr^{3+} cascade emission occurs when the 4f5d state is located above the $^1S_0$ state. It was initially observed in highly ionic materials (fluorides) with a small crystal field splitting for the Pr^{3+} ion (see, for example, the review articles from S. Kück *et al.* [8] and A. P. Vink *et al.* [9]). More recently, it has also been observed in oxides like $LaMgB_5O_{10}$ [10], LaB_3O_6 [11], and $SrAl_{12}O_{19}$ [12]. The first step of the cascade emission is the $^1S_0 \rightarrow {}^1I_6$ transition, which leads to emission with a wavelength of $\sim$ 405 nm. After non-radiative relaxation to the $^3P_0$ level, the second step is a transition from this level to one of the lower lying levels. Typically, radiation of 485 nm ($^3P_0 \rightarrow {}^3H_4$) and of 610 nm ($^3P_0 \rightarrow {}^3H_6$ or $^1D_2 \rightarrow {}^3H_4$) is observed.

Despite their high quantum efficiency, phosphors based on the Pr^{3+} cascade emission are not used in lighting applications because of the unfavorable wavelength of the photons emitted in the first step of the cascade ($\sim$ 405 nm) [13]. A solution to this problem is to convert the $^1S_0 \rightarrow {}^1I_6$ emission to a more useful visible wavelength by energy transfer to a co-activator. Zachau and coworkers tried to transfer the energy of the Pr^{3+} $^1S_0 \rightarrow {}^1I_6$ transition to suitable co-activators, like the Eu^{3+} ion [1]. Considering the favorable spectral overlap between the $^1S_0 \rightarrow {}^1I_6$ emission of Pr^{3+} and the $^7F_{0,1} \rightarrow {}^5D_3, {}^5L_6$ absorption lines of Eu^{3+} efficient energy transfer, followed by the well-known red/orange emission from the $^5D_0$ level of Eu^{3+}, is expected. Upon adding Eu^{3+} as a co-activator in YF_3:Pr^{3+} Zachau *et al.* did not observe any Eu^{3+} emission after excitation of Pr^{3+} into the 4f5d bands. Based on these observations it was concluded that the expected energy transfer does not occur.

This is remarkable, since an important condition for energy transfer, the presence of resonance between the Pr^{3+} $^1S_0 \rightarrow {}^1I_6$ transition and absorptions of the Eu^{3+} ion, is fulfilled. In this case energy transfer can occur through exchange interaction [14] or multipole-multipole interaction [15].

In this work the system YF_3:Pr^{3+}, Eu^{3+} is studied to solve the puzzle presented in Ref. [1]. First, it is shown that based on dipole-dipole interaction, energy transfer between nearest-neighbor Pr^{3+} $^1S_0 \rightarrow {}^1I_6$ and Eu^{3+} $^7F_{0,1} \rightarrow {}^5D_3$, $^5L_6$ has a similar probability as radiative decay from the Pr^{3+} $^1S_0$ level. As a result, energy transfer and subsequent Eu^{3+} emission should occur. To explain the observed absence of Eu^{3+} emission upon excitation in the $^1S_0$ level of Pr^{3+}, luminescence spectra and time-resolved luminescence signals were measured for YF_3:Pr^{3+} 1%, Eu^{3+} x% (x =

0, 5 and 10). The experiments show a strong quenching of the Pr^{3+} $^1S_0$ emission in the presence of Eu^{3+} ions. This quenching process is attributed to non-radiative relaxation via a metal-to-metal charge-transfer state.

4.2 Experimental

4.2.1 Sample preparation

Powder samples of YF_3 doped with Pr^{3+} and samples doped with Pr^{3+} and codoped with Eu^{3+}, Yb^{3+}, or La^{3+} were prepared by mixing stoichiometric amounts of YF_3, PrF_3, YbF_3, EuF_3, and LaF_3. The mixtures were fired in a tube oven under a nitrogen atmosphere at 650 °C. A sample of YF_3 doped with 1% Pr^{3+}, a sample doped with 1% Pr^{3+} and 5% Eu^{3+} and a sample doped with 1% Pr^{3+} and 10% Eu^{3+} were fired simultaneously. A second batch consisted of YF_3 doped with 1% Pr^{3+}, YF_3 doped with 1% Pr^{3+} and 5% Yb^{3+}, and YF_3 doped with 1% Pr^{3+} and 10% of Yb^{3+}. A third batch consisted of YF_3 doped with 1% Pr^{3+}, YF_3 doped with 1% Pr^{3+} and 5% La^{3+}, and YF_3 doped with 1% Pr^{3+} and 10% of La^{3+}. The phase purity was checked with powder diffraction. YF_3 has space group $Pnma$ and the site symmetry for the cation is C_s [16].

4.2.2 Optical measurements

Luminescence spectra in the UV/VIS spectral region were recorded with a SPEX DM-3000F spectrofluorometer with a 450 W Xe-lamp as excitation source. The excitation light was dispersed by double 0.22 m gratings (SPEX 1680, 1200 l/mm) blazed at 150 nm for the excitation light and at 500 nm for the emission light. A spectrum for the wavelength-dependent intensity of the lamp/gratings combination was obtained by division of the excitation spectrum of Pyridine 2 dissolved in ethanol by the absorption spectrum of this solution. The signal detected in the excitation spectra was corrected for the wavelength dependent intensity of the lamp and the wavelength dependent throughput of the excitation gratings with this spectrum.

For dye solutions, an excitation spectrum* divided by an absorption spectrum yields a straight line as a function of wavelength if the quantum efficiency of the dye is independent of wavelength. Since an excitation spectrum obtained in an experiment is altered by the spectral distribution of the lamp and the throughput of the excitation gratings, division of the two experimental spectra gives a spectrum of the wavelength dependent intensity of the lamp/grating combination. Such a correction curve was obtained independently for two dyes: Pyridine 2 (its absorption coefficient varies one order of magnitude with wavelength, and its quantum

*For the excitation spectrum the concentration of dye in the solution was small, so that saturation effects were avoided. For all wavelengths the transmission was larger than 90%.

efficiency as a function of wavelength is not known) and Rhodamine 6G (its absorption coefficient varies two orders of magnitude as a function of wavelength, so that the excitation spectrum has a worse signal-to-noise ratio for low absorption, and the quantum efficiency is known to be independent of excitation wavelength [17]). Both correction spectra yielded the same correction curve but for the Pyridine 2 dye a better signal-to-noise ratio was obtained.

Emission spectra with VUV excitation source were recorded on a SPEX DM-3000F spectrofluorometer, adapted for excitation in the VUV [7]. The spectra were corrected for the gratings/detector combination with a typical response curve provided by the manufacturer. To be able to compare the intensities of different spectra, all spectra were recorded under the same experimental conditions.

For time-resolved luminescence measurements with a sub-microsecond time resolution an excimer laser (ExciStar S-200, TuiLaser) filled with an argon/fluorine gas mixture was used as excitation source. The pulse duration of the laser is typically 10 ns and the wavelength is 193 nm. The emission was detected by a Jobin Yvon Triax 550 spectrometer, equipped with a Hamamatsu R7154 photo-multiplier tube. The signal was monitored as a function of time with a Tektronix 2440 digital oscilloscope.

Time-resolved luminescence measurements with a sub-nanosecond time resolution were recorded at the DESY Synchrotron in Hamburg (Germany) at the HIGITI experimental station of HASYLAB, which is described in detail elsewhere [7]. The bunch separation was 200 ns, which sets the upper limit of the measuring range of life times to ~ 1 μs.

4.3 Results and Discussion

4.3.1 Energy-transfer rate

To evaluate if energy transfer via dipole-dipole interaction can compete with radiative decay, the Förster theory [15] for resonant energy transfer can be applied. In Ref. [1] emission and excitation spectra were recorded and based on the observed spectral overlap between the Pr^{3+} $^1S_0$ emission and Eu^{3+} absorption lines it was concluded that energy transfer from the $^1S_0$ level of Pr^{3+} to Eu^{3+} is expected. No quantitative analysis was presented. To determine if the absence of Eu^{3+} emission upon excitation in the $^1S_0$ level of Pr^{3+} can be due to low energy-transfer rates, first the critical distance for dipole-dipole energy transfer is determined. In figure 4.1 the Pr^{3+} emission ($^1S_0 \rightarrow {}^1I_6$) and Eu^{3+} excitation spectrum ($^7F_{0,1} \rightarrow {}^5D_3, {}^5L_6$) in the region of interest (around 400 nm) are shown. The spectra are in good agreement with the spectra reported by Zachau *et al.* [1]. Spectral overlap between the Pr^{3+} emission and the Eu^{3+} absorption lines is present around 400 nm. For a quantitative analysis the expression derived by Förster [15] and Dexter [18] for the energy-transfer rate

for dipole-dipole interaction is considered,

$$\gamma_{\mathrm{dd}} = \frac{3\hbar^4 c^4 \gamma_{\mathrm{r}}}{4\pi n^4 R^6} Q_{\mathrm{a}} \int \frac{g_{\mathrm{d}}(E) g_{\mathrm{a}}(E)}{E^4} \mathrm{d}E. \tag{4.1}$$

Here γ_{dd} is the energy-transfer rate for dipole-dipole interaction (s^{-1}), R is the donor-acceptor distance (m), γ_{r} is the radiative decay rate of the donor transition (s^{-1}) and Q_{a} is the integrated absorption strength of the acceptor transition (Jm^2). The integral over the energy (J) defines the spectral overlap of the emission spectrum of the donor and the absorption spectrum of the acceptor. Both spectra are normalized and denoted by $g_i(E)$. All other symbols have their usual meaning. The emission spectrum is normalized from 250 to 450 nm where al strong $^1\mathrm{S}_0$ emission lines are situated [8]. The refractive index n of YF_3 around 400 nm is 1.58 [19].

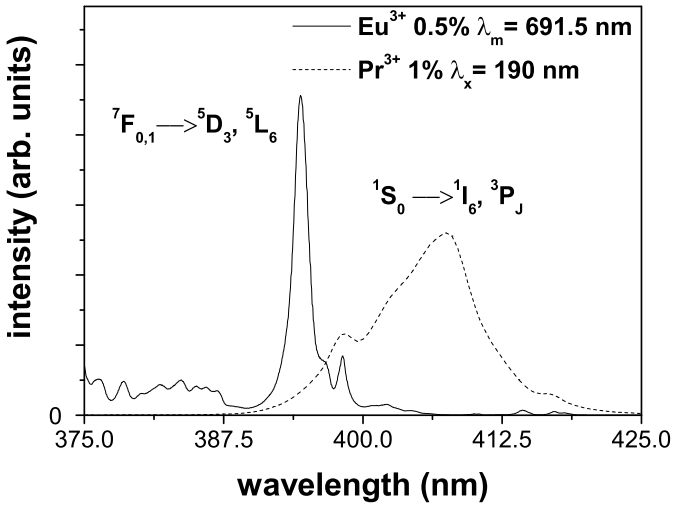

Figure 4.1: Excitation spectrum of YF_3:Eu^{3+} 0.5% (solid line) and emission spectrum of YF_3:Pr^{3+} 1% (dashed line). The excitation and emission wavelengths are indicated in the figure. Both spectra were recorded at room temperature (RT). Note the spectral overlap between the Pr^{3+} $^1\mathrm{S}_0 \rightarrow {}^1\mathrm{I}_6$, $^3\mathrm{P}_J$ emissions and the Eu^{3+} $^7\mathrm{F}_{0,1} \rightarrow {}^5\mathrm{D}_3$, $^5\mathrm{L}_6$ absorptions.

To determine the integrated absorption strength Q_{a} in the spectral region of interest an absorption spectrum can be recorded for a slice of a single crystal with a well-determined width and concentration of Eu^{3+} ions. Since we have only microcrystalline powder samples, a different method was chosen to estimate the absorption strength in the spectral region between 375 and 425 nm. The absorp-

tion strength for the $^7F_{0,1}\rightarrow{}^5D_3$,$^5L_6$ transitions was estimated by scaling the absorption strength to calculated absorption strengths of the magnetic dipole transitions $^7F_0\rightarrow{}^5D_1$ (around 525 nm) and $^7F_1\rightarrow{}^5D_0$ (around 590 nm). These absorption strengths were calculated from the oscillator strength P by

$$Q_{\mathrm{a}} \;=\; \frac{he^2}{4\epsilon_0 mc}P. \tag{4.2}$$

The oscillator strength for transitions within the $4f^n$ configuration of lanthanide ions is the sum of the (forced) electric-dipole contribution, which is strongly dependent on the host lattice, and the magnetic-dipole contribution, which is lattice independent. For the electric-dipole forbidden $^7F_0\rightarrow{}^5D_1$ and $^7F_1\rightarrow{}^5D_0$ transitions the oscillator strengths are determined by the magnetic-dipole transition moments and are lattice independent [20,21],

$$P_{\mathrm{md}} \;=\; \frac{\pi\hbar\nu}{3mc^2}\frac{n}{g_{\mathrm{J}}}(\mathbf{L} \;+\; 2\mathbf{S})^2. \tag{4.3}$$

The transition frequency is denoted by ν ;g_{J} is the statistical weight of the lower energy J-multiplet, determined by the degeneracy of the J-multiplet and its Boltzman factor. From the energies of the $^7F_1$ crystal field components (relative to the $^7F_0$ ground state) and the degeneracy (3 for $^7F_1$ vs. 1 for $^7F_0$) the statistical weight at room temperature is 5.74 for the $^7F_1$ level and 2.09 for the $^7F_0$ level. The matrix elements ($\mathbf{L}+2\mathbf{S}$) for the magnetic-dipole transitions are 0.107 for the $^7F_1$-$^5D_0$ transition and 0.0204 for the $^7F_0$-$^5D_1$ transition [22].

To determine the transition dipole moment for the forced electric-dipole transitions in the region around 400 nm the excitation spectrum of the Eu^{3+} emission is shown in figure 4.2. In this spectrum the magnetic-dipole transitions around 525 nm and 590 nm are well-resolved, as well as the stronger lines around 400 nm. The experimentally determined ratio of the integrated absorption strength in figure 4.2 for the magnetic-dipole transitions $^7F_1\rightarrow{}^5D_0$ and $^7F_0\rightarrow{}^5D_1$ is 1.04 times larger than the calculated ratio for these transitions. The difference may be due to some contribution of forced electric-dipole transitions and to the fact that transitions from the different crystal field levels of the $^7F_1$ multiplet do not have the same transition probabilities (as assumed in the analysis). The deviation between experiment and theory gives an indication of the accuracy of the method used to determine the oscillator strength for the electric-dipole transitions (some 10 % error). From an integrated absorption strength of 2.045×10^{-47} Jm^2 for the $^7F_0\rightarrow{}^5D_1$ transition, the integrated absorption strength in the region 375-425 nm is calculated to be 80×10^{-47} Jm^2. The spectral overlap integral for this spectral region with the Pr^{3+} $^1S_0$ emission spectrum is 1.32×10^{92} J^{-5}. Substitution of these numbers in equation (5.1) gives

$$\gamma_{\mathrm{dd}} \;=\; \gamma_{\mathrm{r}}\Big(\frac{0.40}{R}\Big)^6, \tag{4.4}$$

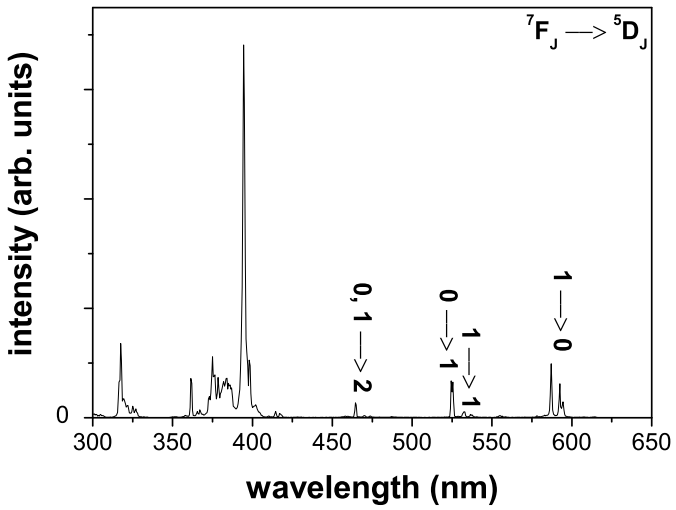

Figure 4.2: Excitation spectrum (RT) of YF_3:Eu^{3+} 0.5%. The emission wavelength monitored is 691.5 nm. $^7F_J \rightarrow {}^5D_J$ transitions are assigned in the figure.

where R is in nm. The critical distance for energy transfer R_c of 0.40 nm is similar to the distance between nearest neighbors in the YF_3 lattice (0.359 nm) which means that for nearest neighbor pairs of Pr-Eu the transfer rate is comparable to the radiative decay rate from the $^1S_0$ level. It is therefore peculiar that no Eu^{3+} emission is observed in YF_3:Pr^{3+}, Eu^{3+}. At Eu^{3+} concentrations of 5 or 10 mole% (relative to Y) a significant fraction of Pr^{3+} ions will have a nearest Eu^{3+} neighbor. To explain the absence of Eu^{3+} emission in the codoped YF_3 systems the following section describes experiments on the luminescence intensity and time-resolved behavior for the $^1S_0$ emission in YF_3:Pr^{3+} 1%, Eu^{3+} x% and YF_3:Pr^{3+} 1%, Yb^{3+} x%.

4.3.2 Luminescence of YF_3:Pr^{3+}, Eu^{3+} and YF_3:Pr^{3+}, Yb^{3+}

Measuring emission spectra of YF_3:Pr^{3+} 1% codoped with various Eu^{3+} concentrations can provide evidence for the occurrence of energy transfer. In case of energy transfer, the Pr^{3+} $^1S_0$ emission is expected to decrease in favor of Eu^{3+} emissions, since Pr^{3+} ions that have close Eu^{3+} neighbors depopulate their $^1S_0$ levels by energy transfer to Eu^{3+}.

Emission spectra are shown in figure 4.3 for three different Eu^{3+} codoping concentrations. Excitation is at 190 nm. At this wavelength Pr^{3+} ions are excited selectively in the 4f5d state. The strong Eu^{3+} $4f^5$5d and Eu-F charge-transfer transitions are at higher energies and direct excitation of Eu^{3+} can only occur in the weak tran-

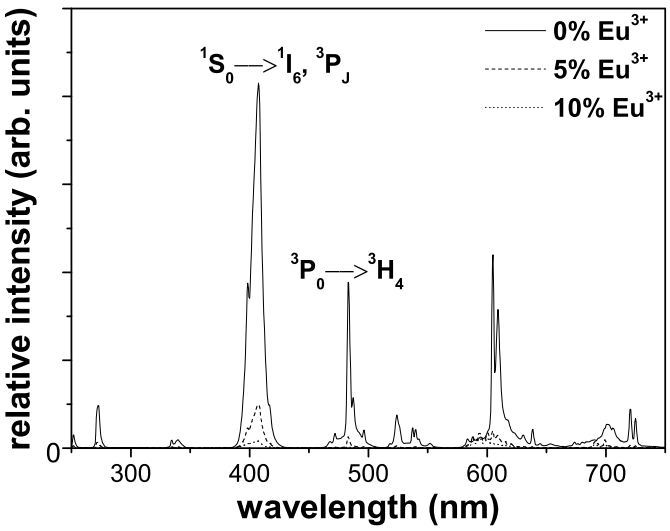

Figure 4.3: Emission spectra (RT) of YF_3 doped with 1% Pr^{3+} and codoped with Eu^{3+} plotted on a relative intensity scale. The concentrations of Eu^{3+} are indicated in the figure. Excitation is into the Pr^{3+} $^3H_4\rightarrow$ 4f5d band at 190 nm. The Pr^{3+} $^1S_0\rightarrow{}^1I_6$, ^3P_J and $^3P_0\rightarrow{}^3H_4$ transitions are indicated in the figure.

sitions within the $4f^6$ configuration. For the YF_3:Pr^{3+} sample (solid line), the well-known Pr^{3+} $^1S_0\rightarrow{}^1I_6$, ^3P_J and $^3P_0\rightarrow{}^3L_J$ cascade emission is observed [1,3,23]. When Eu^{3+} is codoped (dashed and dotted lines) the cascade emission is still present, but no pronounced Eu^{3+} emission (around 600 nm) is observed. This confirms the observations of Zachau *et al.* and indicates that the expected energy transfer from Pr^{3+} to Eu^{3+} does not take place. However, by keeping the measuring conditions the same for the emission spectra recorded for the three samples (YF_3:Pr^{3+} 1%, YF_3:Pr^{3+} 1%, Eu^{3+} 5% and YF_3:Pr^{3+} 1%, Eu^{3+} 10%) an interesting observation is made. Comparison of the relative intensities in figure 4.3 shows that the Pr^{3+} emission is quenched due to the presence of Eu^{3+} ions. This quenching is strong: for 5% Eu^{3+}, the Pr^{3+} $^1S_0$ emission lines have decreased to $\sim$10% compared to the intensity of the sample with only Pr^{3+}. The branching ratio of the $^1S_0$ multiplet does not change. Experimental variations in the measured luminescence intensity, for instance caused by different morphologies of the powders and small changes in the alignment, lead to fluctuations in intensity of typically 20%. This can not explain the observed strong reduction in intensity. Therefore, the decrease in the emission intensity as presented in figure 4.3 shows that Eu^{3+} quenches the Pr^{3+} luminescence.

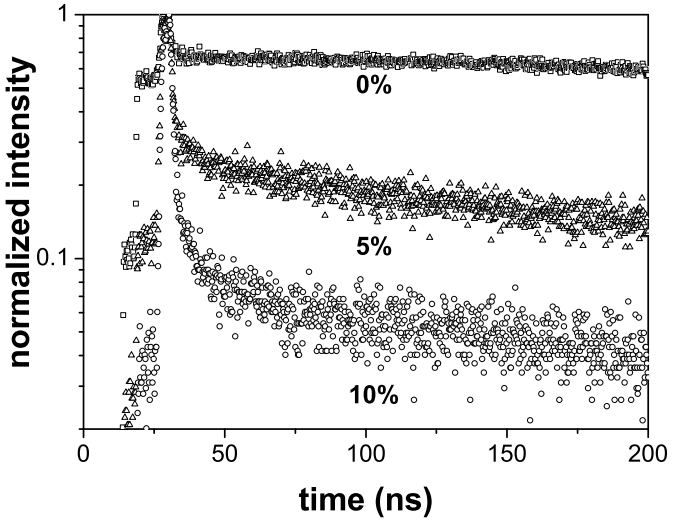

Figure 4.4: Decay curves (RT) of YF_3 doped with 1% Pr^{3+} and codoped with Eu^{3+}. The doping concentrations of Eu^{3+} are indicated in the figure. The wavelength monitored is 251.5 nm (Pr^{3+} $^1S_0 \rightarrow {}^3F_4$ transition).

Supporting evidence for quenching of the Pr^{3+} luminescence by Eu^{3+} is obtained by time-resolved luminescence measurements, shown in figure 4.4. In the experiments the Pr^{3+} $^1S_0 \rightarrow {}^3F_4$ luminescence intensity was monitored as a function of time after pulsed excitation for three different samples: YF_3 doped with 1% Pr^{3+} and codoped with 0, 5 or 10% Eu^{3+}. The doping concentrations of Eu^{3+} are indicated in the figure. For the singly doped compound (0% Eu^{3+}) the decay curve consists of a fast and a slow component. The slow component is due to the radiative decay of Pr^{3+}. Measurements with a sub-microsecond time resolution yield a decay rate for the slow component of 570 ns. The fast component may be attributed to either a small fraction of Pr^{3+} ions that have a fast non-radiative decay component, or to a defect emission with a fast decay rate. Since the fast components were also present when other transitions originating from the $^1S_0$ level were monitored, the fast component is attributed to Pr^{3+} ions that have additional non-radiative decay pathways.

When europium is codoped the contribution of the fast component increases strongly. Furthermore, the slow component becomes faster. The changes in the time-resolved signal can be explained by the introduction of non-radiative decay when incorporating Eu^{3+} into the lattice.

Both the emission spectra and the time-resolved luminescence measurements

show that Eu^{3+} ions act as quenching centers for Pr^{3+} $^1S_0$ luminescence. The interaction between Eu^{3+} and Pr^{3+} does not lead to efficient Eu^{3+} emission. Considering these observations, the following mechanism is proposed: Eu^{3+} and Pr^{3+} interact through a (Eu^{2+}, Pr^{4+}) charge-transfer (CT) state, which energetically overlaps the Pr^{3+} $^1S_0$ level. The large lattice relaxation involved in the metal-to-metal charge-transfer (MMCT) transition leads to a fast non-radiative decay to the ground state and explains the absence of emission.

To test this hypothesis the luminescence behavior of Pr^{3+} is studied when Yb^{3+} ions are used as codoping ions instead of Eu^{3+} ions. The Dieke diagrams [24, 25] for Pr^{3+} and Yb^{3+} show that there are no possibilities for resonant energy transfer between Pr^{3+} $^1S_0 \rightarrow {}^{2S+1}L_J$ and Yb^{3+} $^2F_{7/2} \rightarrow {}^2F_{5/2}$ transitions. Furthermore, the Yb-F charge-transfer and $4f^{12}5d$ states of Yb^{3+} are at high energies in fluorides ($> 60\ 000\ cm^{-1}$ [26]). Quenching of the Pr^{3+} $^1S_0$ emission by Yb^{3+} is therefore not possible via resonant energy transfer to Yb^{3+}. However, the redox potential for the Yb^{3+}/Yb^{2+} couple is very similar to that of the Eu^{3+}/Eu^{2+} couple (typically, the $Yb^{3+} \rightarrow Yb^{2+} + h$ CT transition is slightly higher in energy than the $Eu^{3+} \rightarrow Eu^{2+} + h$ transition [26]). If quenching of the Pr^{3+} $^1S_0$ emission occurs via a metal-to-metal charge-transfer state for Pr^{3+}-Eu^{3+} pairs, a similar process is expected for Pr^{3+}-Yb^{3+} pairs. In view of the somewhat higher energy of the charge-transfer state of Yb^{3+} (compared to Eu^{3+}) quenching is expected to be less efficient.

Experimental evidence can be obtained by luminescence experiments on YF_3:Pr^{3+} codoped with Yb^{3+}. Figure 4.5 shows emission spectra for YF_3:Pr^{3+} 1%, Yb^{3+} x% (x = 0, 5, 10). The YF_3:Pr^{3+} 1% sample used for these measurements is prepared under the same conditions as the doubly doped samples. As expected, the singly doped compound (solid line) shows the cascade emission with the same branching ratio as for the YF_3:Pr^{3+} 1% sample which was fired with the Eu^{3+} codoped samples. When adding Yb^{3+} (dashed and dotted lines), the luminescence intensity decreases, although not as strongly as for codoping with Eu^{3+}. The branching ratio of the $^1S_0$ emission is unaffected by the addition of Yb^{3+}.

Figure 4.6 shows the luminescence decay curves. The Yb^{3+} doping concentrations are indicated in the figure. For the singly doped compound, the decay curve again consists of a fast and a slow component (τ = 570 ns). Upon adding Yb^{3+}, the fast component becomes more pronounced and also the decay rate of the slow component increases, indicating depopulation of the $^1S_0$ state due to the presence of Yb^{3+} ions. In view of the absence of pathways involving resonant energy transfer from Pr^{3+} ($^1S_0$) to Yb^{3+}, this observation supports the presence of quenching through a metal-to-metal charge-transfer state for both Pr^{3+}-Eu^{3+} and Pr^{3+}-Yb^{3+} pairs.

Measurements of the Pr^{3+} $^1S_0$ emission intensity in YF_3:Pr^{3+} 1%, La^{3+} x% revealed a moderate decrease of the luminescence intensity as a function of La^{3+} doping concentration. When 10% La^{3+} is added, the signal reduces to 40%. Due to the larger difference in ionic radius of La^{3+} as compared to Yb^{3+} or Eu^{3+} when doped

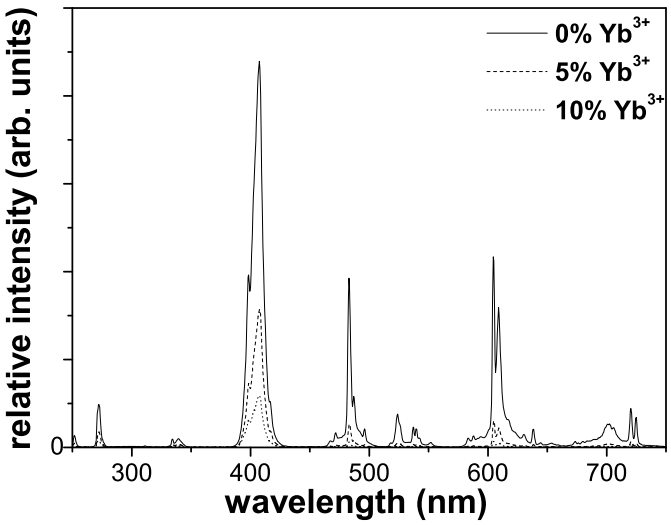

Figure 4.5: Emission spectra (RT) of YF_3 doped with 1% Pr^{3+} and codoped with Yb^{3+} plotted on a relative intensity scale. The concentrations of Yb^{3+} are indicated in the figure. Excitation is into the Pr^{3+} $^3H_4 \rightarrow$ 4f5d band at 190 nm.

into YF_3, more lattice strain will be induced when incorporating such a large concentration of La^{3+}. Distortions of the YF_3 host material can lead to defect sites that quench the Pr^{3+} luminescence. The reduction of the Pr^{3+} $^1S_0$ emission intensity induced by strain is much smaller than the reduction induced by codoping with Eu^{3+} or Yb^{3+}, thus providing evidence that quenching through a MMCT is responsible for the observed reduction and not strain in these systems.

Further evidence for the possibility of quenching through a MMCT state is found in the literature. In a systematic study by Dorenbos [27] on the energetic location of the trivalent and divalent lanthanide ions, it was noted that in general Ce^{3+} 5d $\rightarrow$ 4f luminescence is quenched by Eu^{3+} through electron transfer from Ce^{3+} 5d to Eu^{3+}. This is the same mechanism as the quenching mechanism proposed in the present study. The electron transfer is possible since the energetic position of the lowest Ce^{3+}5d level is higher than the position of the Eu^{2+} ion. Based on the results presented in Ref. [27] it can be expected that the $Pr^{3+1}S_0$ level is quenched by Eu^{3+} and Yb^{3+} since in both of these cases the $Pr^{3+1}S_0$ state is higher in energy than Eu^{2+} or Yb^{2+}. Not only are the findings of Dorenbos in agreement with the present study, they also show that the presence of this MMCT transition and the resulting quenching of the luminescence is expected in every host lattice.

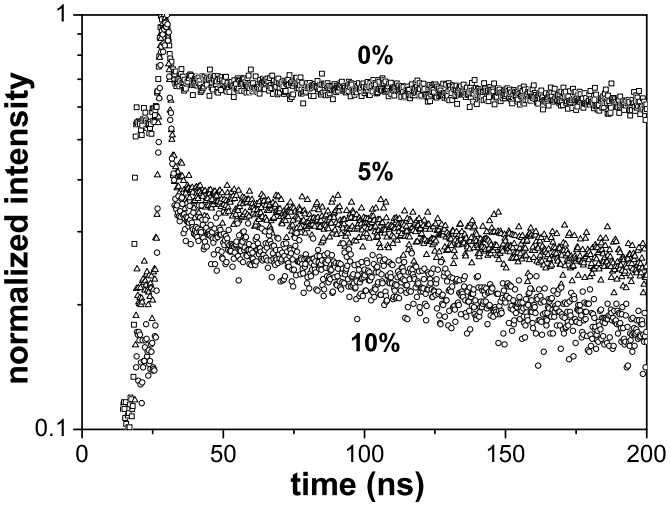

Figure 4.6: Decay curves (RT) of YF_3 doped with 1% Pr^{3+} and codoped with Yb^{3+}. The doping concentrations of Yb^{3+} are indicated in the figure. The wavelength monitored is 251.5 nm (Pr^{3+} $^1S_0 \rightarrow {}^3F_4$ transition).

An estimate for the critical distance R_c of the quenching process can be obtained from the integrated signal, I, of the normalized luminescence decay curves (figures 4.4 and 4.6) for the samples codoped with 5 and 10% of Eu^{3+} or Yb^{3+}, assuming a statistical distribution of rare-earth (RE) ions over the cation sites. An estimation of the number of lattice sites N involved in quenching of the Pr^{3+} $^1S_0$ luminescence is obtained by,

$$N = \frac{\log(I/I_0)}{\log(1 - c_{RE})}, \tag{4.5}$$

where I_0 is the integrated luminescence intensity for a singly (Pr^{3+}) doped compound and c_{RE} is the fraction of Eu^{3+} or Yb^{3+}. When N is known, it can be mapped on the radial distribution function of the cation sites in YF_3 and an estimate for R_c is obtained. This procedure leads to an R_c for YF_3:Pr^{3+}, Eu^{3+} between 0.62 and 0.69 nm. For YF_3:Pr^{3+}, Yb^{3+} a value between 0.42 and 0.62 nm is obtained. The integrated signal of the $^1S_0$ emission in figures 4.3 and 4.5 can also be used as I in equation (4.5). If this is done larger R_c's are obtained (0.76 nm for Eu^{3+} and 0.63 nm for Yb^{3+}). This overestimation may be caused by competitive absorption of the metal-to-metal CT state at 190 nm. This absorption reduces the $^1S_0$ emission intensity in addition to the reduction caused by quenching due to nearby Eu^{3+} or Yb^{3+} ions. The normalized decay curves are not sensitive for the reduction by competitive

absorption.

Compared to an R_c for dipole-dipole interaction of 0.40 nm, the critical distance for quenching of the $^1S_0$ emission by a MMCT is larger and is the dominating process. This explains the observation that no Eu^{3+} emission is observed upon excitation of Pr^{3+} in the $^1S_0$ level.

4.4 Conclusion

Using the Förster theory it is shown that energy transfer between Pr^{3+} $^1S_0 \rightarrow {}^1I_6$, ^3P_J and Eu^{3+} $^7F_{0,1} \rightarrow {}^5D_3$, $^5L_6$ can occur through a dipole-dipole mechanism, with a critical distance of 0.40 nm. However, the energy-transfer process is surpassed by a stronger interaction, which leads to a fast depopulation of the Pr^{3+} $^1S_0$ level. When comparing the relative intensity of emission spectra and time-resolved luminescence measurements of the Pr^{3+} emission in the presence of either Eu^{3+} or Yb^{3+}, it is observed that these ions act as quenching centers for the Pr^{3+} $^1S_0$ luminescence. This is attributed to the presence of a metal-to-metal charge-transfer state: RE^{3+}, $Pr^{3+} \rightarrow RE^{2+}$, Pr^{4+} (RE = Eu or Yb). The larger value of the critical distance for quenching in comparison to the critical distance for energy transfer explains the absence of Eu^{3+} emission upon excitation of Pr^{3+} in the $^1S_0$ level.

References

[1] M. Zachau, F. Zwaschka, and F. Kummer, Proceedings - Electrochemical Society **97-29**, 314 (1998).

[2] J. L. Sommerdijk, A. Bril, and A. W. de Jager, Journal of Luminescence **9**, 288 (1974).

[3] W. W. Piper, J. A. DeLuca, and F. S. Ham, Journal of Luminescence **8**, 344 (1974).

[4] R. T. Wegh, H. Donker, K. D. Oskam, and A. Meijerink, Science **283**, 663 (1999).

[5] R. T. Wegh, E. V. D. van Loef, and A. Meijerink, Journal of Luminescence **90**, 111 (2000).

[6] R. Pappalardo, Journal of Luminescence **14**, 159 (1976).

[7] R. T. Wegh *et al.*, Physical Review B **56**, 13841 (1997).

[8] S. Kuck *et al.*, Journal of Luminescence **102-103**, 176 (2003).

[9] A. P. Vink, P. Dorenbos, and C. W. E. Van Eijk, Journal of Solid State Chemistry **171**, 308 (2003).

[10] A. M. Srivastava, D. A. Doughty, and W. W. Beers, Journal of the Electrochemical Society **143**, 4113 (1996).

[11] A. M. Srivastava, D. A. Doughty, and W. W. Beers, Journal of the Electrochemical Society **144**, L190 (1997).

[12] A. M. Srivastava and W. W. Beers, Journal of Luminescence **71**, 285 (1997).

[13] T. Justel, H. Nikol, and C. Ronda, Angewandte Chemie-International Edition **37**, 3085 (1998).

[14] D. L. Dexter, Physical Review **108**, 630 (1957).

[15] T. Forster, Annalen der Physik **2**, 55 (1948).

[16] A. Zalkin and D. H. Templeton, Journal of the American Chemical Society **75**, 2453 (1953).

[17] R. A. Velapoldi, Journal of Research of the National Bureau of Standards, Section A: Physics and Chemistry **76**, 641 (1972).

[18] D. L. Dexter, Journal of Chemical Physics **21**, 836 (1953).

[19] P. Chindaudom and K. Vedam, Applied Optics **33**, 2664 (1994).

[20] J. A. Detrio, Physical Review B **[3]4**, 1422 (1971).

[21] J. Sytsma, G. F. Imbusch, and G. Blasse, Journal of Chemical Physics **92**, 3249 (1990).

[22] A. Meijerink and G. J. Dirksen, Journal of Luminescence **63**, 189 (1995).

[23] J. L. Sommerdijk, A. Bril, and A. W. De Jager, Journal of Luminescence **8**, 341 (1974).

[24] G. H. Dieke and H. M. Crosswhite, Applied Optics **2**, 675 (1963).

[25] G. H. Dieke, *Spectra and Energy Levels of Rare Earth Ions in Crystals* (Interscience, New York, 1968).

[26] L. van Pieterson, M. Heeroma, E. de Heer, and A. Meijerink, Journal of Luminescence **91**, 177 (2000).

[27] P. Dorenbos, Journal of Physics: Condensed Matter **15**, 8417 (2003).

Chapter 5

A study on the downconversion efficiency for Pr^{3+}-Mn^{2+} pairs in fluorides

In this chapter the possibility for making an efficient quantum cutter for the conversion of one vacuum-ultraviolet (VUV) photon to two visible photons is investigated for Pr^{3+}-Mn^{2+} ion pairs. Cross relaxation starting at the high-energy $^1S_0$ level of Pr^{3+} offers the possibility for efficient downconversion by Pr^{3+}-Mn^{2+} pairs. It is observed that energy transfer from Pr^{3+} to Mn^{2+} is not efficient, in spite of the favorable spectral overlap between the $^1S_0 \rightarrow {}^1I_6$ emission of Pr^{3+} and the $^6A_1 \rightarrow {}^4A_1, {}^4E$ absorption of Mn^{2+}. To explain the absence of energy transfer, the transfer rates are calculated for cross relaxation through dipole-dipole or exchange interaction. The calculations show that the transfer rates are indeed smaller than the radiative decay rate for the $^1S_0$ level, but they cannot explain the complete absence of observable Pr-Mn energy transfer. Possible explanations are discussed.

5.1 Introduction

The discovery of the mercury-discharge fluorescent tube, more than 100 years ago [1], has resulted in research on luminescent materials (phosphors) for the conversion of 254 nm ultraviolet (UV) radiation into visible light. Since the introduction of the commercial fluorescent tube in 1936, the efficiency and stability of phosphors have improved. For the present generation of phosphors the quantum efficiency for the conversion of 254 nm UV radiation into red, green or blue light is close to 100 % [2]. Further research is mainly aimed at cost price reduction and marginal improvements of the efficiency or stability. Due to the mature status of the product, research on luminescent materials for mercury discharge fluorescent tubes has strongly decreased in the past decades.

Recently, a strong increase in research on luminescent materials for the conversion of vacuum-ultraviolet (VUV) radiation into visible light is observed. There is a need to find new luminescent materials for the conversion of VUV radiation from a xenon discharge (around 172 nm) into visible light [2]. The high energy of the VUV photons allows for the generation of two visible photons for each VUV photon absorbed and the search for a VUV phosphor with a near 200% quantum efficiency is an exciting challenge in the field of luminescence research. Two recent developments are particularly noteworthy in this field. First, photon cascade emission from the $^1S_0$ level of Pr^{3+} allows for a visible quantum efficiency above 100%. Recently it was discovered that this cascade emission is not only possible in fluorides [3, 4], but also in oxides [5–7]. A second breakthrough is the discovery of quantum cutting through downconversion which allows for visible quantum efficiencies close to 200% [8].

The photon cascade emission from Pr^{3+} was first reported for this ion doped in YF_3 [9, 10]. The cascade emission originates from the $^1S_0$ level of Pr^{3+} and can only occur when the lowest energy 4f5d state of Pr^{3+} is situated at higher energies than the $^1S_0$ level. In figure 5.1.a the cascade is depicted. The transition from the $^1S_0$ level to the $^1I_6$ level results in emission of one visible photon around 405 nm. A second visible photon is emitted due to the transition from the $^3P_0$ level to the $^3H_4$ ground level (around 480 nm) or to the $^3H_6$ level (605 nm). Competing emission in the infrared (IR) and UV due to transitions to other levels may also occur but can be suppressed by a proper choice of the host lattice. When Pr^{3+} resides in a site for which the Judd-Ofelt parameter Ω_6 is large compared to the Judd-Ofelt parameters Ω_4 and Ω_2 a favorable VIS/(UV + IR) ratio is obtained [9]. A more serious problem is the wavelength of 405 nm for the photon emitted in the first step. The use of this wavelength in white-light applications results in a too low color rendering index. A solution to this problem is to convert the 405 nm photon to a more useful visible wavelength. This may be achieved by transfer of the $^1S_0 \rightarrow {}^1I_6, {}^3P_J$ energy to a second ion which subsequently emits a visible photon. This cross-relaxation concept was investigated by Zachau *et al.* for Pr^{3+} in combination with various other

rare-earth ions (Sm^{3+}, Eu^{3+}, Dy^{3+}, Er^{3+} and Tm^{3+}) in YF_3 [11]. No cross relaxation was observed.

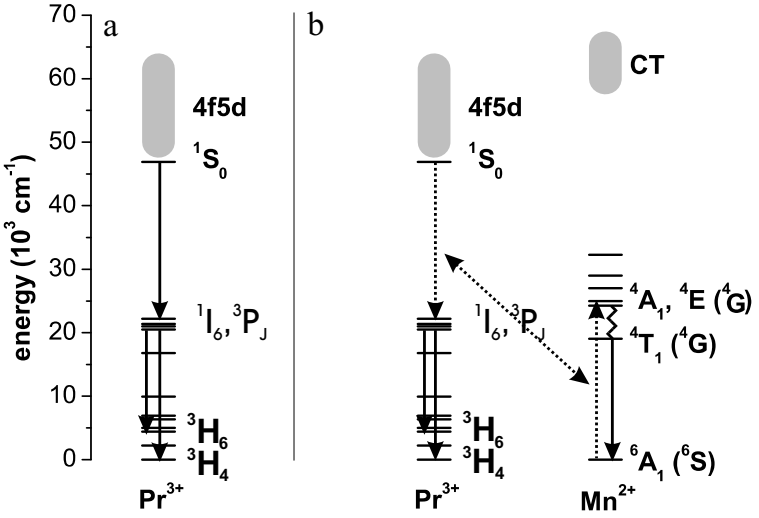

Figure 5.1: (a). Schematic of the Pr^{3+} cascade emission and (b) the desired energy-transfer process between Pr^{3+} and Mn^{2+}. Solid lines denote radiative transitions. The energy-transfer process is depicted by dotted lines. The zig-zag line denotes non-radiative relaxation. After the energy transfer process, Pr^{3+} and Mn^{2+} each emit one visible photon.

In this chapter a study on the possibility to transfer the $^1S_0 \rightarrow {}^1I_6, {}^3P_J$ energy to a 3d transition metal ion is presented. In particular, energy transfer to Mn^{2+} ($3d^5$) is investigated. The Mn^{2+} ion has narrow absorption bands around 400 nm due to transitions from the $^6A_1$ ground state to $^4A_1$ and ^4E excited states. In view of the spectral overlap between the $^1S_0 \rightarrow {}^1I_6, {}^3P_J$ emission and these Mn^{2+} excitation lines, energy transfer is expected to occur (see figure 5.1.b). The excitation transitions on Mn^{2+} are strongly (parity and spin) forbidden, so energy transfer through dipole-dipole interaction is expected to be inefficient. Indeed, in a recent study on $SrAlF_5$ doped with Pr^{3+} and Mn^{2+} no energy transfer was observed [12]. The Mn^{2+} concentration in the samples was not indicated. For high Mn^{2+} concentrations energy transfer might occur through exchange interaction. Energy transfer through exchange is not influenced by the oscillator strengths of the transitions involved [13]. Since exchange interaction occurs through wavefunction overlap the transfer rate drops rapidly with distance and energy transfer is only expected for nearest neighbor Pr^{3+}-Mn^{2+} pairs. As a result, relatively high concentrations of Mn^{2+} have to be used.

In order to study if energy transfer from Pr^{3+} to Mn^{2+} occurs, a number of fluoride host lattices in which Pr^{3+} shows cascade emission have been codoped with

Pr^{3+} and various concentrations of Mn^{2+}. To determine whether or not the desired spectral conversion of the 405 nm emission occurs by energy transfer to Mn^{2+}, luminescence spectra are recorded and analyzed.

5.2 Experimental

5.2.1 Sample preparation

For the study of energy transfer between Pr^{3+} and Mn^{2+} four different fluoride host lattices were synthesized. In all these systems both Pr^{3+} and Mn^{2+} can be incorporated. Dopant concentrations between 0 and 5% were chosen. The YF_3, SrY_2F_8 and CaF_2 samples were synthesized in a high frequency furnace (Philips PH1006/13). Dried powders of the starting compounds were inserted in a vitreous carbon crucible and heated in a dry nitrogen atmosphere until melting was observed. Then the samples were slowly cooled ($\sim$1 degree/minute) to room temperature. For SrY_2F_8 and CaF_2 clear single crystals were obtained. For YF_3 polycrystalline samples were obtained. Polycrystalline powders of $LiBaF_3$ were prepared in a tube furnace. An intimate mixture of LiF, BaF_2 and the dopant fluoride was fired at 800 °C for three hours in a 25% H_2/75% N_2 atmosphere. The resulting products were shown to be single phase by X-ray powder diffraction.

5.2.2 Optical measurements

For spectroscopic measurements with excitation in the VUV region, a SPEX DM-3000F spectrofluorometer equipped with 0.22 m double monochromators (SPEX 1680, 1200 l/mm), adapted for VUV measurements [14], was used. The excitation source was a D_2-lamp (Hamamatsu L1835, 150 W). The spectral resolution of this apparatus is approximately 0.5 nm. Excitation spectra measured on this set up were corrected for the lamp intensity and the throughput of the excitation gratings with spectra of sodium salicylate as a reference [15].

For spectroscopic measurements with excitation in the ultraviolet or visible a 450 W Xe lamp in combination with a SPEX DM-3000F spectrofluorometer with 0.22 m double monochromators (SPEX 1680, 1200 l/mm blazed at 500 nm) was used. A spectrum for the wavelength dependent intensity of the lamp and throughput of the excitation gratings was obtained by division of the excitation spectrum of a Pyridine 2 solution by the absorption spectrum of this solution. The signal detected in the excitation spectra was corrected for the lamp/gratings response with this spectrum.

Time-resolved luminescence measurements were recorded using an excimer laser (ExciStar S-200, Tuilaser) filled with an argone/fluorine gas mixture as excitation source. The pulse duration of the laser is typically 10 ns and the wavelength is 193 nm. The emission was detected by a Jobin Yvon Triax 550 spectrometer, equipped

with a Hamamatsu R928 photo-multiplier tube. The signal was monitored as a function of time with a Tektronix 2440 digital oscilloscope.

Low-temperature VUV excitation spectra were measured at the DESY Synchrotron in Hamburg (Germany) at the HIGITI experimental station of HASYLAB, which is described in detail elsewhere [14].

5.3 Results

For the downconversion of one VUV photon into two visible photons by Pr^{3+} and Mn^{2+} (as shown in figure 5.1) several conditions have to be met: (1) there should be a cascade emission originating from the $^1S_0$ level of the Pr^{3+} ion (i.e., the lowest energy 4f5d state has to be higher in energy than the $^1S_0$ state), (2) the Pr^{3+} $^1S_0 \rightarrow {}^1I_6$ emission lines and absorption lines of the Mn^{2+} ion in the fluoride host lattice should have spectral overlap and (3) the distance between the Pr^{3+} and Mn^{2+} ions needs to be small to allow for interaction between the ions.

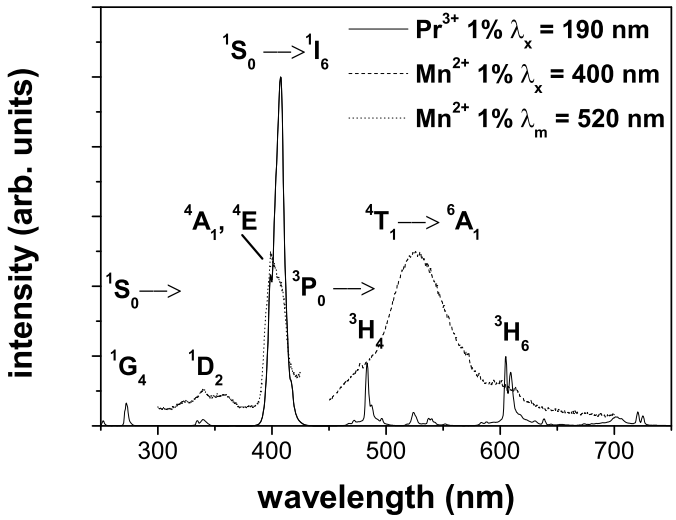

Figure 5.2: Emission and excitation spectra (RT) of YF_3 doped with 1% Pr^{3+} or 1% Mn^{2+}. The excitation wavelengths or the emission wavelength monitored are indicated in the figure.

Optical spectroscopy experiments on singly doped (Pr or Mn) systems provide information on whether or not the first two conditions are met. If this is the case, measurements on doubly doped systems (Pr and Mn) can be done to investigate if the interaction between neighboring ions is strong enough to give rise to efficient

energy transfer. For all fluoride host lattices discussed in this section, the first two conditions are met. As typical examples first the YF_3 and SrY_2F_8 host lattices will be discussed in detail and after this the results for other fluoride host lattices will be presented with a focus on the analysis of the doubly doped samples.

YF_3

In figure 5.2 luminescence spectra are shown of YF_3 samples doped with a single type of ion. The emission spectrum of YF_3:Pr^{3+} upon excitation in the 4f5d band (190 nm) shows a number of sharp lines in the UV and visible part of the spectrum. The spectrum is well known and is dominated by the strong $^1S_0 \rightarrow {}^1I_6$ emission line around 408 nm [9, 10]. In the higher-energy region weaker lines corresponding to other transitions from the $^1S_0$ state are observed and in the visible range there are $^3P_0$ emission lines. The observation of $^1S_0$ emission from Pr^{3+} shows that the 4f5d state is situated above the $^1S_0$ level. The excitation spectrum of the Mn^{2+} emission shows a sharp line around 401 nm and some weaker lines at shorter wavelengths. The 401 nm line is assigned to the $^6A_1 \rightarrow {}^4A_1$, ^4E transitions within the $3d^5$ configuration of Mn^{2+}. The emission spectrum of the Mn^{2+} ion in YF_3 consists of a broad band around 520 nm which is assigned to the $^4T_1 \rightarrow {}^6A_1$ transition.

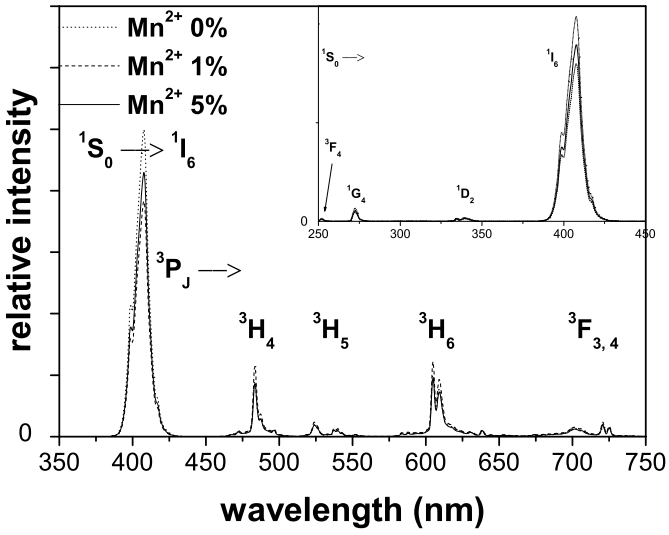

Figure 5.3: Emission spectra (λ_x = 190 nm, RT) of YF_3:Pr^{3+} 1% Mn^{2+} x%. The concentrations of Mn^{2+} are indicated in the figure. The emissions lines are assigned.

The luminescence spectra of YF_3:Pr^{3+} and YF_3:Mn^{2+} show that the first two conditions for energy transfer are met: the 4f5d state is at higher energy than the $^1S_0$ level and the $^1S_0 \rightarrow {}^1I_6$ emission line of Pr^{3+} has a good spectral overlap with the $^6A_1 \rightarrow {}^4A_1$, ^4E absorption lines of Mn^{2+} in YF_3.

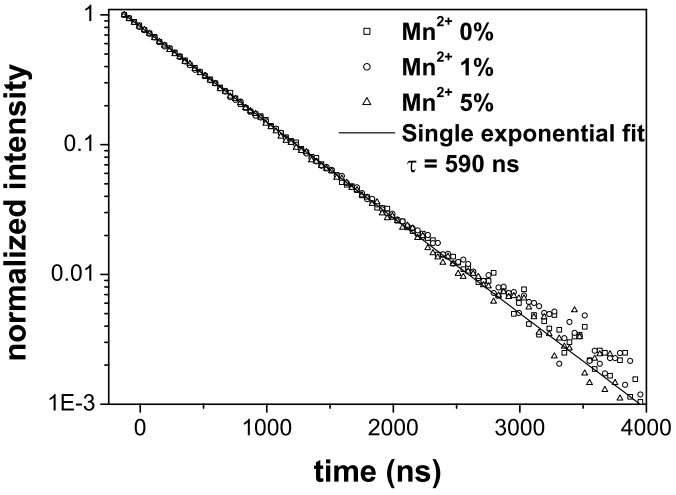

Figure 5.4: Time-resolved luminescence intensity of the Pr^{3+} $^1S_0 \rightarrow {}^1I_6$ emission (λ_x = 193 nm, λ_m = 405 nm, RT) for YF_3:Pr^{3+} 1% Mn^{2+} x%. The concentrations of Mn^{2+} are indicated in the figure.

To investigate if the energy-transfer process (cross relaxation) shown in figure 5.1 occurs, the luminescence properties of doubly doped (Pr^{3+} and Mn^{2+}) YF_3 were investigated. In figure 5.3 the emission spectra of YF_3:Pr^{3+} are shown for samples with the same Pr^{3+} concentration (1 mol% with respect to Y^{3+}) and three different Mn^{2+} concentrations (0%, 1% and 5%). The spectra were recorded under identical circumstances in order to be able to compare absolute emission intensities. The emission in the visible spectral range shows that the spectra do not change upon adding Mn^{2+}. If the energy transfer Pr^{3+}($^1S_0 \rightarrow {}^1I_6$) to Mn^{2+}($^6A_1 \rightarrow {}^4A_1$, ^4E) occurs, one would expect to observe a Mn^{2+} emission band around 520 nm that increases in intensity upon raising the Mn^{2+} concentration. The absence of a Mn^{2+} emission band indicates that energy transfer does not occur. The observation that the Pr^{3+} emission intensity remains constant upon adding Mn^{2+} shows that the absence of a Mn^{2+} emission band is not due to quenching of the Pr^{3+} emission in a Pr-Mn pair. Clearly, there is no energy transfer from Pr^{3+} and Mn^{2+} in spite of the favorable spectral overlap and a considerable number of nearest neighbor pairs of Pr-Mn (especially in the 5% Mn^{2+} sample). From this observation one can conclude that even

for the nearest neighbor pairs the energy transfer cannot compete with radiative decay from the $^1S_0$ state. The small differences in the intensity of the Pr^{3+} emission for the three samples are reproducible and are ascribed to (unintentional) differences in the synthesis procedure. The Pr-emission intensity varies up to 20% between the strongest luminescing sample (0% Mn) and the weakest luminescing sample (1% Mn). The Pr-luminescence intensity of the 5% Mn^{2+} sample is in between, confirming that the intensity is not reduced by energy transfer to Mn^{2+}.

To further support the observation that there is no energy transfer from Pr^{3+} to Mn^{2+} in YF_3, luminescence decay curves were measured for the $^1S_0$ emission in YF_3:Pr^{3+} 1% codoped with 0%, 1% or 5% Mn^{2+}. The luminescence decay curves are shown in figure 5.4. The decay curves are identical and show a single exponential decay characterized by a decay time of 590 ns, which is typical for Pr^{3+} $^1S_0$ emission in YF_3 [16]. The fact that addition of Mn^{2+} up to concentrations of 5% does not influence the luminescence decay behavior of the $^1S_0$ emission confirms the absence of energy transfer from the $^1S_0$ level of Pr^{3+} to Mn^{2+} in YF_3.

SrY_2F_8

The host lattice SrY_2F_8 is particularly interesting for a study of energy transfer between Pr^{3+} and Mn^{2+} since this lattice offers both divalent and trivalent cation sites. Therefore, both Mn^{2+} and Pr^{3+} can be incorporated without the need for charge compensation. In figure 5.5 the excitation and emission spectra of Pr^{3+} in SrY_2F_8 are shown. In the emission spectrum the characteristic emission lines originating from transitions from both the $^1S_0$ level and the $^3P_0$ level are observed. The emission lines are assigned in figure 5.5. In the excitation spectrum, the $4f^2 \rightarrow 4f5d$ (fd) excitation band is observed below 210 nm. The onset of the fd band at 210 nm is very close to the position where the $^1S_0$ level is expected [9]. This indicates that in this host lattice the first condition (cascade emission from the $^1S_0$ level) is only just met.

Figure 5.6 shows the excitation and emission spectra of Mn^{2+} in SrY_2F_8. The Mn^{2+} ion has a bright green/yellow emission in this host lattice with a maximum at 545 nm. The emission can be assigned to the $^4T_1 \rightarrow {}^6A_1$ transition within the $3d^5$ configuration of Mn^{2+}. In the excitation spectrum the weak (spin and parity-forbidden) transitions within the $3d^5$ configuration are observed between 250 and 450 nm. The lines and bands are assigned in the spectrum. One of the stronger excitation lines (corresponding to the $^6A_1 \rightarrow {}^4A_1$, ^4E transitions) is situated around 400 nm. The strong absorption band (not to scale in figure 5.6) with an onset at 180 nm and a maximum at 150 nm is assigned to the F^- to Mn^{2+} charge-transfer (CT) transition which is usually located in the VUV [12].

The observation of cascade emission from the $^1S_0$ level of Pr^{3+} shows that the first condition is met. To determine whether or not there is spectral overlap for energy transfer from Pr^{3+} to Mn^{2+} via cross relaxation, the Pr^{3+} emission spectrum and the Mn^{2+} excitation spectrum in the region 250-500 nm need to be compared.

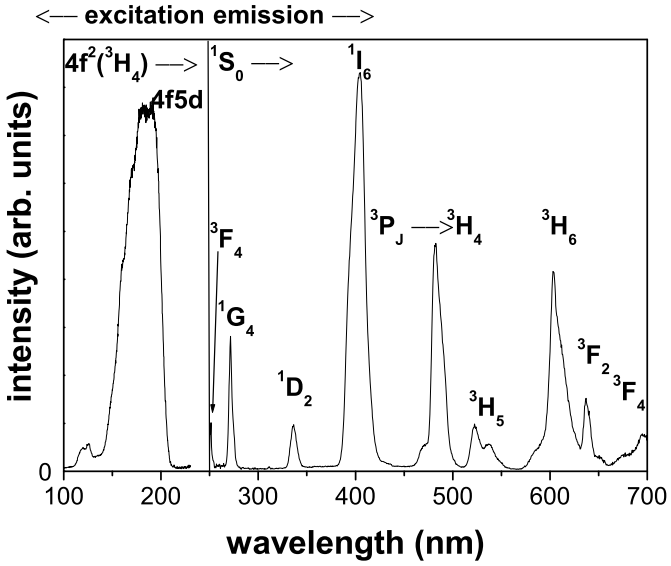

Figure 5.5: Excitation (10 K, $\lambda_m = 401$ nm) and emission (RT, $\lambda_x = 186$ nm) spectrum of SrY_2F_8:Pr^{3+} 0.05%.

Comparison of figure 5.5 (right-hand side) and figure 5.6 (left-hand side) shows a good spectral overlap between the $^1S_0 \rightarrow {}^1I_6$ emission of Pr^{3+} and the $^6A_1 \rightarrow {}^4A_1$, ^4E excitation lines of Mn^{2+} in SrY_2F_8. This allows for cross relaxation between Pr^{3+} and Mn^{2+} which gives rise to emission of two visible photons: one from the $^3P_0$ level of Pr^{3+} (after relaxation from $^1I_6$ to $^3P_0$) and one from the $^4T_1$ level of Mn^{2+} (after relaxation from $^4A_1$, ^4E to $^4T_1$). Also other cross-relaxation processes between Pr^{3+} in the $^1S_0$ excited state and Mn^{2+} in the ground state are possible: from the spectral overlap between the $^1S_0 \rightarrow {}^1D_2$ emission of Pr^{3+} and the $^6A_1 \rightarrow {}^4E(^4D)$ excitation line of Mn^{2+} (both around 340 nm) it is clear that also cross relaxation can occur which results in Pr^{3+} in the $^1D_2$ excited state and Mn^{2+} in the $^4E(^4D)$ excited state. Also this cross-relaxation process can give rise to the emission of two visible photons (one red photon from the $^1D_2$ level of Pr^{3+} and one yellow/green photon from Mn^{2+}). An undesired cross-relaxation process would involve the energy transfer of the $^1S_0 \rightarrow {}^1G_4$ energy of Pr^{3+} to Mn^{2+} (exciting Mn^{2+} to the $^4T_1(^4P)$ level). The spectral overlap observed around 270 nm shows that also this cross-relaxation process may occur. As emission from the $^1G_4$ level of Pr^{3+} is in the infrared spectral region, this process is undesired.

To investigate if any of the cross-relaxation processes as described above do indeed occur, codoped samples of SrY_2F_8 with 0.05% Pr^{3+} and 0, 1 or 5% Mn^{2+} were

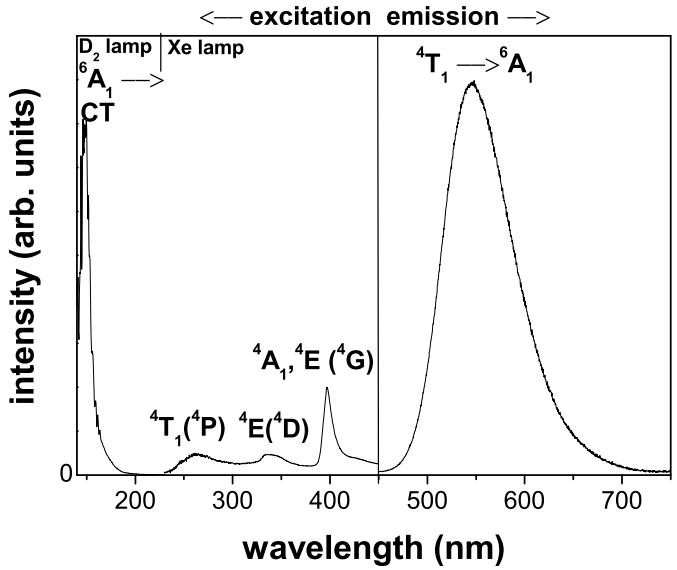

Figure 5.6: Excitation ($\lambda_m = 555$ nm) and emission ($\lambda_x = 161$ nm) spectra (RT) of SrY_2F_8:Mn^{2+} 1%. The excitation spectrum consists of two parts. Since two different lamps (indicated in the figure) are used in the excitation spectrum, the two parts of the excitation spectrum are not to scale. The absorption band denoted CT has a much higher intensity (see text).

synthesized. Figure 5.7 shows emission spectra recorded for singly doped (0.05% Pr^{3+}) and doubly doped (0.05% Pr^{3+} and 5% Mn^{2+}) samples upon excitation in the $4f^2 \rightarrow 4f5d$ band of Pr^{3+} at 185 nm. At this wavelength, Pr^{3+} ions are excited almost exclusively (the Mn^{2+} CT absorption band is at higher energies). If energy transfer via cross relaxation occurs, the relative intensity of the $^1S_0$ emission lines will decrease and emission from Mn^{2+} is expected to be observed in the doubly doped sample. However, figure 5.7 shows that the emission spectrum hardly changes when Mn^{2+} is present. No quenching of the $^1S_0$ emission is detected, and only very weak Mn^{2+} emission around 545 nm is observed, probably due to direct excitation into the tail of the Mn-F CT transition. It can be concluded that the expected (and desired) cross-relaxation process is either very inefficient or does not occur at all.

$LiBaF_3$

Emission spectra of Pr^{3+} doped in $LiBaF_3$ and of a doubly doped sample are shown in figure 5.8. The emission spectrum of the Pr^{3+}-doped compound (dashed line)

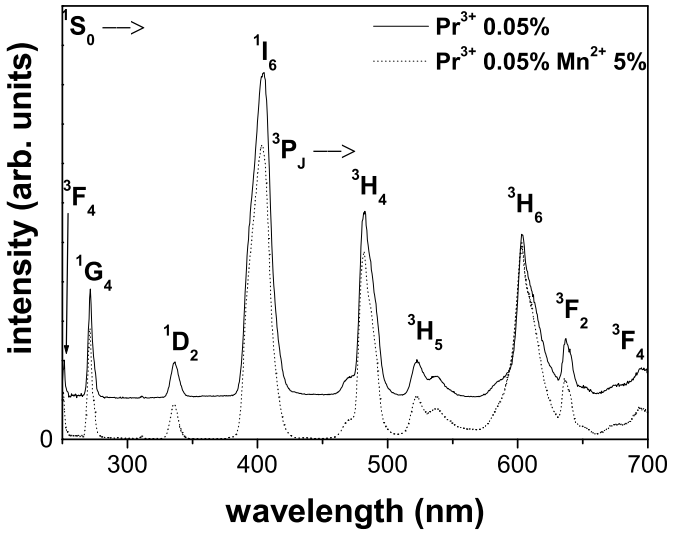

Figure 5.7: Emission spectra (RT, $\lambda_x = 185$ nm) of SrY_2F_8 doped with 0.05% Pr^{3+}, or with 0.05% Pr^{3+} and 5% Mn^{2+}. The spectrum of the singly doped compound is shifted along the y-axis.

shows the familiar cascade emission. For the doubly doped sample (solid line), a broad band in the red is observed which is assigned to the Mn^{2+} $^4T_1 \rightarrow {}^6A_1$ transition. A red Mn^{2+} emission indicates a Mn^{2+} site with a relatively large crystal-field splitting. The other emission lines of smaller intensity coincide with the Pr^{3+} emissions and are assigned accordingly.

In figure 5.9 excitation spectra of $LiBaF_3$ doped with 5% Mn^{2+}, 1% Pr^{3+}, and a doubly doped sample (1% Pr^{3+} and 5% Mn^{2+}) are shown. The excitation spectrum of the Pr^{3+} emission shows the 4f5d band in the VUV region, above the $^1S_0$ level. The high energetic location of the Pr^{3+} 4f5d transition is expected since Pr^{3+} substitutes for 12-coordinated Ba^{2+} ions [17]. For the Mn^{2+}-doped and the doubly doped sample the Mn^{2+} $^4T_1 \rightarrow {}^6A_1$ emission is monitored around 670 nm to record the excitation spectra. In both spectra a broad band between 210 and 170 nm is observed. This band is assigned to a Mn-F CT transition, even though the wavelength of this absorption band is rather long for a Mn-F charge transfer. Two possible explanations can be given for this observation. First, this band may be ascribed to a Mn-O charge-transfer band, since the presence of oxygen as an impurity cannot be excluded. However, the emission spectrum after excitation at 190 nm is the same as after excitation in the $^4A_1$, ^4E absorption lines at 400 nm. Since the bulk of Mn^{2+} ions can be excited at 400 nm, this shows that the emission at 670 nm is not due to

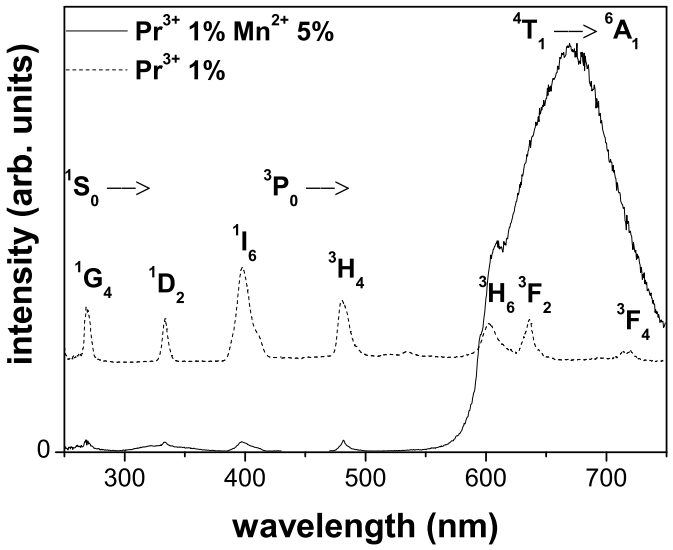

Figure 5.8: Emission spectra (10 K, $\lambda_x = 190$ nm) of $LiBaF_3$ doped with 1% Pr^{3+}, or with 1% Pr^{3+} and 5% Mn^{2+}. The emission spectrum of the singly doped compound is shifted along the y-axis. Emissions are assigned in the figure.

a fraction of Mn^{2+} ions which are close to an oxygen impurity. Alternatively, Mn^{2+} may substitute for Li^+ in $LiBaF_3$. The Li^+ ion has octahedral coordination in $LiBaF_3$ and an ionic radius of 0.74 Å [18] for sixfold coordination. This is close to the ionic radius of sixfold coordinated Mn^{2+} (0.83 Å), whereas Ba^{2+} has a larger ionic radius (1.35 Å, sixfold coordination [18]). The stronger interaction with fluorine ions for Mn^{2+} on the relatively small Li^+ sites may cause a shift to lower energies, explaining the presence of the CT band around 190 nm. Substitution of Mn^{2+} for a Li^+ in $LiBaF_3$ is supported by EPR studies of Yosida [19]. It is also in agreement with the long-wavelength emission of Mn^{2+}, since Mn^{2+} on octahedral sites is known to give red emission [20].

On the basis of the excitation and emission spectra presented above the occurrence of energy transfer can be discussed. The overlap between the Pr^{3+} fd excitation band and the Mn^{2+} CT excitation band complicates the analysis. The fact that the excitation spectrum of the Mn^{2+} emission in the doubly doped sample and the singly doped (Mn^{2+}) sample are identical indicates that energy transfer does not occur. Also the observation that the relative intensities of the $^1S_0$ emission lines to the $^3P_0$ emission lines hardly change in the doubly doped sample confirms that energy

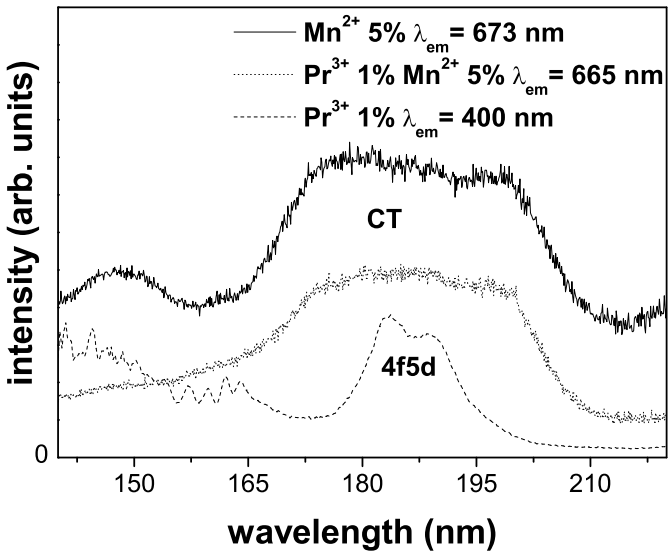

Figure 5.9: Excitation spectra (10 K) of $LiBaF_3$ samples doped with 5% Mn^{2+}, 1% Pr^{3+}, or both. For the doubly doped sample the Mn^{2+} $^4T_1 \rightarrow {}^6A_1$ transition is monitored. Emission wavelengths are indicated in the figure. The spectra monitoring Mn^{2+} transitions are shifted along the y-axis.

transfer as depicted in figure 5.1 does not take place in spite of a favorable spectral overlap.

CaF_2

Figure 5.10 shows excitation spectra of two singly doped compounds (CaF_2 doped with 0.05% Pr^{3+} or doped with 0.5% Mn^{2+}) and a doubly doped compound (0.05% Pr^{3+} and 5% Mn^{2+}). For the Pr^{3+}-doped sample (dashed line), the 4f5d band is again situated above the $^1S_0$ level. For the Mn^{2+}-doped sample (solid line), the Mn-F CT transition is at higher energy, with a peak at 156 nm.

In the excitation spectrum of the Mn^{2+} emission in the doubly doped sample the Pr^{3+} fd excitation bands do not show up. The clear absence of the 4f5d excitation bands shows that energy transfer from the $^1S_0$ state of Pr^{3+} to Mn^{2+} does not occur. Note that the shape of the Mn^{2+} excitation spectrum is changed for the doubly doped sample, possibly due to competitive absorption on the longer-wavelength side (160-175 nm) of the Mn^{2+} excitation band.

The absence of energy transfer is also apparent in the emission spectra. Figure 5.11

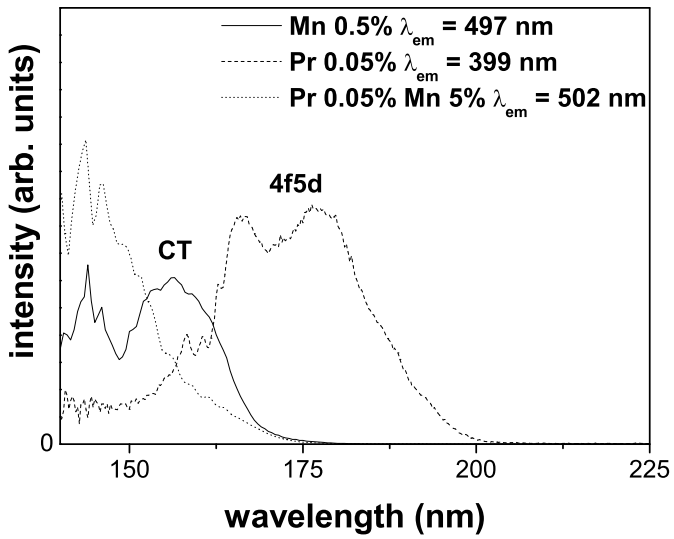

Figure 5.10: Excitation spectra (RT) of CaF_2 doped with 0.5% Mn^{2+}, 0.05% Pr^{3+}, or with 0.05% Pr^{3+} and 5% Mn^{2+}. Emission wavelengths are indicated in the figure.

shows the emission spectra of the singly doped samples (0.05% Pr^{3+} or 0.5% Mn^{2+}) and the doubly doped sample (0.05% Pr^{3+} and 5% Mn^{2+}). The bright green Mn^{2+} emission band is observed in the Mn^{2+}-doped sample upon excitation in the charge-transfer band. The emission spectrum of the Pr^{3+}-doped sample shows the cascade emission of Pr^{3+}. Note that the intensity of the $^3P_0$ emission is very weak relative to the $^1S_0$ emission. This is explained by quenching of the $^3P_0$ emission by cross relaxation in clusters of Pr^{3+} [21]. For the doubly doped sample the emission spectrum shows the strong $^1S_0$ emission lines upon excitation in the 4f5d band of Pr^{3+}. A very weak Mn^{2+} emission band is observed around 500 nm, probably due to excitation in the tail of the Mn-F charge-transfer excitation band. The lines around 610 nm are attributed to Pr^{3+} $^1D_2 \rightarrow {}^3H_4$ emissions. The Pr^{3+} ions that show this emission are located at an irregular site. The excitation spectrum of the 610 nm emission shows, apart from a band around 190 nm, an additional band around 220 nm. The appearance of the band around 220 nm shows that these Pr^{3+} ions are located at a site for which the cascade emission is absent. Just as for the other fluoride host lattices no energy transfer from the $^1S_0$ state of Pr^{3+} to Mn^{2+} occurs in spite of the high Mn^{2+} concentration and the good spectral overlap between the $^1S_0 \rightarrow {}^1I_6$ emission of Pr^{3+} and the $^6A_1 \rightarrow {}^4A_1$, ^4E excitation lines of Mn^{2+}.

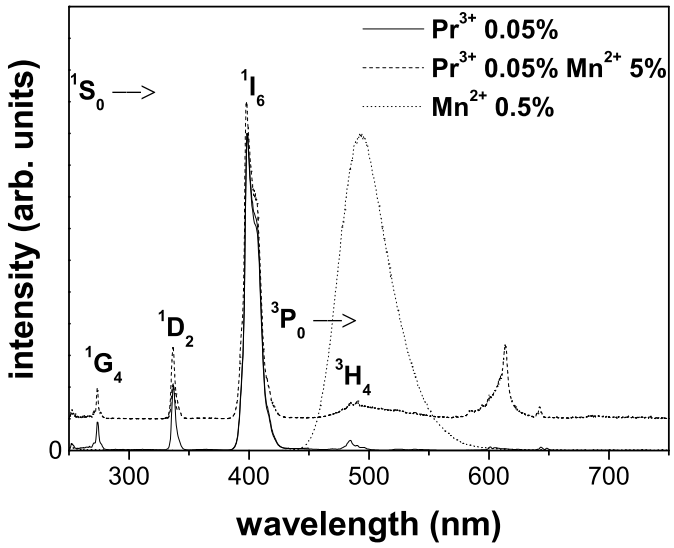

Figure 5.11: Emission spectra (RT) of CaF_2 doped with 0.05% Pr^{3+} ($\lambda_x = 177$ nm), 0.5% Mn^{2+} ($\lambda_x = 160$ nm), or with 0.05% Pr^{3+} and 5% Mn^{2+} ($\lambda_x = 177$ nm). The Pr^{3+} emission lines are assigned and the emission spectrum for the doubly doped sample is shifted along the y-axis.

5.4 Discussion

In the previous section spectroscopic results were presented to study the occurrence of cross relaxation in Pr^{3+}-Mn^{2+} pairs in a number of fluoride lattices. For each host lattice, $^1S_0$ emission lines of Pr^{3+} and a good spectral overlap between the $^1S_0$ emission lines and the Mn^{2+} absorption bands were observed. Despite the fulfillment of these two conditions, no evidence of energy transfer between Pr^{3+} and Mn^{2+} was found. For Pr^{3+} and Mn^{2+} doped in YF_3 and SrY_2F_8, Mn^{2+} emission was completely absent after excitation in the Pr^{3+} 4f5d band. For the doubly doped samples of CaF_2 and $LiBaF_3$ excitation spectra of the Mn^{2+} $^4T_1 \rightarrow {}^6A_1$ emission did not show the 4f5d excitation bands of Pr^{3+}. The apparent absence of energy transfer between Pr^{3+} and Mn^{2+} is in line with the findings of Van der Kolk *et al.* [12].

In order to understand the absence of energy transfer, energy-transfer rates are calculated for energy transfer by dipole-dipole or exchange interaction. First, energy transfer by dipole-dipole interaction will be considered. The energy-transfer rate γ_{dd} is given by [13],

$$\gamma_{\mathrm{dd}} = \frac{3\gamma_{\mathrm{rad}}\hbar^4c^4}{4\pi n^4R^6}Q_{\mathrm{a}}\int\frac{g_{\mathrm{d}}(E)g_{\mathrm{a}}(E)}{E^4}\mathrm{d}E. \tag{5.1}$$

Equation (5.1) includes the radiative decay rate of the donor (γ_{rad}), the integrated absorption strength of the acceptor (Q_{a}), the spectral overlap between donor and acceptor transitions, which is given by the integral, and the distance R between donor and acceptor. The function $g_i(E)$ is the normalized spectral lineshape function of the resonant transitions on the donor or acceptor ion and n is the refractive index.

In order to determine Q_{a} in equation (5.1), the oscillator strength P for the Mn^{2+} $^6A_1\rightarrow{}^4A_1$, ^4E transitions is taken from Ref [22] as 0.45×10^{-7} and the integrated absorption coefficient is calculated with [23],

$$Q_{\mathrm{a}} = \frac{he^2}{4\epsilon_0 mc}P, \tag{5.2}$$

to be 1.0×10^{-46} Jm^2. With n equals 1.58 [24] and a spectral overlap of 5.2×10^{92} J^{-5} determined from the Pr^{3+} emission spectrum and the Mn^{2+} absorption spectrum in YF_3, equation (5.1) yields,

$$\gamma_{\mathrm{dd}} = \gamma_{\mathrm{rad}}\Big(\frac{0.36}{R}\Big)^6, \tag{5.3}$$

where R is in nm.

The critical distance for energy transfer of 3.6 Å is slightly smaller than the nearest-neighbor distance in the different fluoride host lattices (typically the nearest-neighbor distance is around 3.8 Å). This means that the radiative decay from the $^1S_0$ level has a higher probability than energy transfer to a nearest neighbor Mn^{2+} ion. This is in line with the observation that the energy transfer is inefficient. Nevertheless, with a critical distance for energy transfer of 3.6 Å, energy transfer is expected to be observable in the samples with high Mn^{2+} concentrations. For example, in YF_3 the cations have 10 nearest-neighbor cation sites between 3.6 Å and 4.4 Å. Assuming a random distribution of Mn^{2+} ions over these cation sites results in 40% of the Pr^{3+} ions to have one or more Mn^{2+} nearest neighbors in a sample codoped with 5 mole% of Mn^{2+}. The energy-transfer rate to these nearest neighbors is about 0.5 times the radiative decay rate of the $^1S_0$ emission and as a result the relative intensity of the Mn^{2+} emission is expected to be around 13% of the $^1S_0$ emission intensity. Similar numbers (around 10% Mn^{2+} emission for the systems codoped with 5 mole% of Mn^{2+}) are obtained for the other fluoride host lattices. The emission spectra for YF_3:Pr^{3+} 1%, Mn^{2+} 5% (figure 5.3) and SrY_2F_8:Pr^{3+} 0.05%, Mn^{2+} 5% (figure 5.7) show a much weaker relative intensity of the Mn^{2+} emission (less than 1%) upon excitation in the 4f5d band of Pr^{3+}. Clearly, the calculated energy-transfer efficiency is not in line with the observed absence of energy transfer.

Moreover, one may argue that energy transfer by exchange interaction is more efficient at short distances, which would lead to an even higher predicted relative

intensity of Mn^{2+} emission. As was argued in the introduction, energy transfer to Mn^{2+} through dipole-dipole interaction is expected to be inefficient due to the small oscillator strengths of the transitions on the Mn^{2+} ion. Indeed, exchange interaction has been shown to be the dominant energy-transfer mechanism in the commercial phosphor $Ca_5(PO_4)_3F$:Sb^{3+}, Mn^{2+}, where the Sb^{3+} ions act as donors [25]. In comparison with the dipole-dipole mechanism the rate of energy transfer by exchange interaction was found to be more than two orders of magnitude larger. Also for $Eu^{2+}\rightarrow Mn^{2+}$ energy transfer the exchange interaction mechanism dominates [26]. For the Pr-Mn couple it will be shown that energy transfer via exchange interaction is inefficient.

For energy transfer from Sb^{3+} or Eu^{2+} to Mn^{2+} the outer 5s/5p orbitals of Sb^{3+} or the 5d orbitals of Eu^{2+} are involved in the exchange interaction. For Pr^{3+} the $^1S_0$ ($4f^2$) state is involved. Since the spatial extension of the inner-shell 4f orbitals is much smaller than of the Sb^{3+} 5s/5p or Eu^{2+} 5d orbitals, exchange interaction is expected to be weaker for Pr^{3+}-Mn^{2+} than for Sb^{3+}-Mn^{2+} or Eu^{2+}-Mn^{2+}. To estimate the difference in transfer rate the theory of Dexter [13] is used. Dexter showed that the energy-transfer rate for exchange interaction γ_{ex} is proportional to,

$$\gamma_{ex} \propto \exp(-2R/L), \tag{5.4}$$

where R is the distance between donor and acceptor and L is an effective average Bohr radius for the excited and unexcited states of the donor and acceptor.

Bohr radii of 1.8 Å and 0.57 Å are calculated for Sb^{3+} 5s/5p and Pr^{3+} 4f wavefunctions, respectively. Wavefunctions defined by Slater [27] are used to obtain these radii. Evaluation of equation (5.4) for a cation nearest-neighbor distance of 3.6 Å (in YF_3), leads to an energy-transfer rate for Sb^{3+} as the donor that is three orders of magnitude faster than for Pr^{3+} as the donor. This large difference is due to the large difference in Bohr radii between the outer-shell Sb^{3+} 5s/5p orbitals and the inner-shell 4f orbitals. Based on this estimate and the relatively short radiative decay time of the $^1S_0$ level of Pr^{3+} ($\tau \simeq 0.6$ μs) compared to Sb^{3+} ($\tau \simeq 10$ μs [25]) it can be understood that for the Pr^{3+}-Mn^{2+} couple energy transfer by exchange interaction will not be more efficient than energy transfer via dipole-dipole interaction.

Still, the lack of observable energy transfer in the experiments is not in line with the predictions for dipole-dipole energy transfer. Explanations for this may be that only a fraction of the Mn^{2+} ions is incorporated in the host lattices, or that clusters of Mn^{2+} are formed. When Mn^{2+} is doped in $LiBaF_3$, YF_3, SrY_2F_8, or CaF_2, substitution of Mn^{2+} for cations from the host lattice may be hampered by the large difference in ionic radii between Mn^{2+} and the cations of the host lattices [18], or by a difference in valency of the cations. However, incorporation of the weighed amounts of Mn^{2+} in the samples was confirmed by inductively coupled plasma-optical emission spectrometry.

Further work is needed to resolve the issue of why Pr^{3+}-Mn^{2+} energy transfer is absent. On the experimental side, knowledge of the local distribution of Mn^{2+} in

the samples is desired. Insight in the local distribution of Mn^{2+} may be obtained by techniques that probe magnetic interactions. On the theoretical side, a more accurate knowledge of the wavefunctions of Pr^{3+} and Mn^{2+} may lead to a more reliable estimate of the energy-transfer rate by exchange interaction.

5.5 Conclusion

In this work the occurrence of visible quantum cutting in Pr^{3+}-Mn^{2+} pairs by energy transfer from the $^1S_0$ level of Pr^{3+} is studied experimentally. Despite the favorable spectral overlap between Pr^{3+} $^1S_0 \rightarrow {}^1I_6, {}^3P_J$ transitions and the Mn^{2+} $^6A_1 \rightarrow {}^4A_1, {}^4E$ transitions energy transfer does not occur. The origin for the absence of energy transfer is unclear. When substitution of cations for Mn^{2+} on a statistical basis is assumed, energy transfer through a dipole-dipole mechanism, although inefficient, is expected to occur. In order to resolve the discrepancy between experiment and theory, experiments to gain insight in the local distribution of Mn^{2+} ions are required.

References

[1] P. C. Hewitt, Patent No. 682699 (1901).

[2] T. Justel, H. Nikol, and C. Ronda, Angewandte Chemie-International Edition **37**, 3085 (1998).

[3] S. Kuck *et al.*, Journal of Luminescence **102-103**, 176 (2003).

[4] A. P. Vink, P. Dorenbos, and C. W. E. Van Eijk, Journal of Solid State Chemistry **171**, 308 (2003).

[5] A. M. Srivastava, D. A. Doughty, and W. W. Beers, Journal of the Electrochemical Society **143**, 4113 (1996).

[6] A. M. Srivastava and W. W. Beers, Journal of Luminescence **71**, 285 (1997).

[7] A. M. Srivastava, D. A. Doughty, and W. W. Beers, Journal of the Electrochemical Society **144**, L190 (1997).

[8] R. T. Wegh, H. Donker, K. D. Oskam, and A. Meijerink, Science **283**, 663 (1999).

[9] W. W. Piper, J. A. DeLuca, and F. S. Ham, Journal of Luminescence **8**, 344 (1974).

[10] J. L. Sommerdijk, A. Bril, and A. W. De Jager, Journal of Luminescence **8**, 341 (1974).

[11] M. Zachau, F. Zwaschka, and F. Kummer, Proceedings - Electrochemical Society **97-29**, 314 (1998).

[12] E. Van der Kolk *et al.*, Journal of Applied Physics **95**, 7867 (2004).

[13] D. L. Dexter, Journal of Chemical Physics **21**, 836 (1953).

[14] R. T. Wegh *et al.*, Physical Review B **56**, 13841 (1997).

[15] J. A. R. Samson, *Techniques of Vacuum Ultra Violet Spectroscopy* (John Wiley & Sons, New York, 1967).

[16] P. Vergeer, V. Babin, and A. Meijerink, Journal of Luminescence **114**, 267 (2005).

[17] P. Dorenbos, Journal of Luminescence **91**, 155 (2000).

[18] R. D. Shannon, Acta Crystallographica Section A **32**, 751 (1976).

[19] T. Yosida, Journal of the Physical Society of Japan **49**, 127 (1980).

[20] D. T. Palumbo and J. Brown, J. J., Journal of the Electrochemical Society **118**, 1159 (1971).

[21] C. G. Levey, T. J. Glynn, and W. M. Yen, Journal of Luminescence **31-32**, 245 (1984).

[22] S. W. S. McKeever, B. Jassemnejad, J. F. Landreth, and M. D. Brown, Journal of Applied Physics **60**, 1124 (1986).

[23] W. B. Fowler and D. L. Dexter, Physical Review **128**, 2154 (1962).

[24] P. Chindaudom and K. Vedam, Applied Optics **33**, 2664 (1994).

[25] T. F. Soules, R. L. Bateman, R. A. Hewes, and E. R. Kreidler, Physical Review B **7**, 1657 (1973).

[26] U. G. Caldino, A. F. Munoz, and O. J. Rubio, Journal of Physics: Condensed Matter **2**, 6071 (1990).

[27] J. C. Slater, Physical Review **36**, 57 (1930).

Chapter 6

Quantum cutting by cooperative energy transfer in $Yb_xY_{1-x}PO_4:Tb^{3+}$

This chapter presents experimental evidence for cooperative energy transfer from Tb^{3+} to two Yb^{3+} ions and a determination of the energy-transfer rate. Energy transfer from Tb^{3+} to Yb^{3+} was investigated by luminescence measurements on $Yb_xY_{1-x}PO_4$ doped with 1% Tb^{3+}. Time-resolved luminescence experiments were analyzed using Monte Carlo simulations based on theories for phonon-assisted, cooperative, and accretive energy transfer. The luminescence decay curves of the $^5D_4$ emission from Tb^{3+} show an excellent agreement with simulations based on cooperative energy transfer via dipole-dipole interaction, while a phonon-assisted or an accretive energy-transfer mechanism cannot explain the experimental results. The energy-transfer rate to two nearest-neighbor Yb^{3+} ions is 0.26 ms^{-1}. This corresponds to an upper limit for the energy-transfer efficiency of 88% in $YbPO_4:Tb^{3+}$ 1%.

6.1 Introduction

The recent discovery of visible quantum-cutting phosphors [1, 2] has been an exciting development in the search for luminescent materials with a high energy efficiency. In luminescent devices such as fluorescent tubes or plasma display panels, the phosphors used nowadays convert one ultraviolet (UV) photon into one visible photon by dissipating roughly 50% of the absorbed energy into heat. The efficiency gain in quantum-cutting materials is based on the principle that a quantum-cutting phosphor is able to emit two visible photons for every (vacuum-)ultraviolet photon absorbed. The excitation energy is divided over the two photons, leading to the necessary redshift of the absorbed radiation without losing energy efficiency.

Quantum-cutting materials may also be applied in solar cells [3]. If conversion of one UV/VIS photon into two infrared (IR) photons is realized, energy losses by thermalization of electron-hole pairs are minimized. The most widely used solar sells are based on crystalline Si. The development of solar cells would greatly benefit from a quantum-cutting phosphor with the energy of its emission located just above the band gap of Si.

Research on quantum-cutting systems started on single ions capable of a cascade emission such as Pr^{3+} [4, 5], Tm^{3+} [6], and Gd^{3+} [7]. Recently, the focus has shifted to combinations of two ions, where the energy of the donor ion is transferred stepwise to two acceptor ions. This process is generally known as downconversion. A well-known example is the Gd^{3+}-Eu^{3+} couple [1], where for every vacuum-ultraviolet (VUV, $\lambda < 200$ nm) photon absorbed by Gd^{3+}, two red photons are emitted by different Eu^{3+} centers. Another example is the combination Gd^{3+}-Tb^{3+}-Er^{3+} [2]. In both systems, VUV radiation is downconverted to visible radiation with a quantum efficiency exceeding 100%.

Theories for predicting energy-transfer rates (including down- and upconversion) were developed in the late 40s and 50s by Förster [8] and Dexter [9]. These theories are based on different models for the interaction between donor and acceptor centers, viz. dipole-dipole interaction versus exchange interaction through wavefunction overlap. These have in common that the donor and the acceptor transitions should be resonant as the spectral overlap integral relates the energy-transfer rate to the density of acceptor and donor states at a resonant frequency. Therefore, to facilitate first-order energy transfer, the emission spectrum of the donor should overlap with the excitation spectrum of the acceptor. The two quantum-cutting phosphors mentioned above are based on this principle. Splitting of the energy is reached by population of an intermediate energy level of the donor.

If overlap between donor emission and acceptor absorption is absent, second-order downconversion may become the dominant relaxation process (competing with spontaneous emission). In this process a donor excites two acceptors simultaneously. The resonance condition is fulfilled if the sum of the energy of the absorption transitions of the two acceptor centers equals the energy of the emission of the

donor.

This cooperative sensitisation process was predicted in 1957 by Dexter [9] but only recently Basiev *et al.* observed the occurrence of second-order downconversion [10] by measuring the enhancement of the Nd^{3+} $^4F_{3/2}\rightarrow{}^4I_{15/2}$ decay rate upon increasing the Ce^{3+} concentration in the compound $La_{1-x}Ce_xF_3$:Nd^{3+} 0.3%. This enhancement was attributed to second-order downconversion from the Nd^{3+} $^4F_{3/2}$ level exciting two Ce^{3+} ions to their $^2F_{7/2}$ level. Unfortunately, the Ce^{3+} $^2F_{7/2}\rightarrow{}^2F_{5/2}$ emission, in the IR ($\sim$ 5000 nm), was not detected and therefore direct proof of energy transfer from Nd^{3+} to Ce^{3+} was not obtained. In later papers Basiev *et al.* addressed simulations and theory on second-order energy-transfer processes [11, 12] but no comparison to experiments was made.

A promising system to study second-order energy-transfer processes is the combination of one Tb^{3+} and two Yb^{3+} ions: the Tb^{3+} $^5D_4\rightarrow{}^7F_6$ transition is located at approximately twice the energy of the Yb^{3+} $^2F_{7/2}\rightarrow{}^2F_{5/2}$ transition and Yb^{3+} has no other levels up to the UV region (see figure 6.1). Moreover, the $^2F_{5/2}\rightarrow{}^2F_{7/2}$ emission is situated around 1000 nm, just above the band edge of crystalline Si.

Previous studies of Tb-Yb compounds have focused on the experimental observation of upconversion [13–25]. When these compounds are exposed to infrared radiation around 1000 nm, Yb^{3+} ions act as absorption centers. After an upconversion process, green Tb^{3+} luminescence was observed. If energy transfer by a second-order process is responsible for the upconverted luminescence, downconversion should occur as well. In some studies mentioned above, this becomes apparent by an increased decay rate of the upconverted luminescence compared to directly excited Tb^{3+} luminescence [13–15, 21, 22, 24]. However, in analyzing transient luminescence curves, the downconversion probability has often been neglected. Studies that do consider downconversion mention two possibilities for the decay mechanism: second-order energy transfer and phonon-assisted energy transfer [20, 22, 23]. However, downconversion in the Tb-Yb system by either one of these mechanisms has never been established experimentally.

The purpose of this paper is to study second-order downconversion in Tb-Yb compounds and to elucidate its efficiency and energy-transfer mechanism. Energy transfer in powders of $Yb_xY_{1-x}PO_4$ doped with 1% Tb^{3+} is studied by emission, excitation and time-resolved luminescence measurements. The time-resolved luminescence measurements are compared to theories for phonon-assisted energy transfer [26] and second-order downconversion, by simulations using Monte Carlo methods and analytical calculations. According to Auzel [16] and Andrews & Jenkins [27] second-order downconversion can occur through a cooperative and an accretive mechanism. The present analysis shows that the cooperative dipole-dipole mechanism gives an excellent agreement between theory and experiment. Energy transfer via the accretive or the phonon-assisted mechanism cannot explain the experimental observations.

The energy-transfer efficiency is shown to be 88% for $YbPO_4$:Tb^{3+} 1%. This

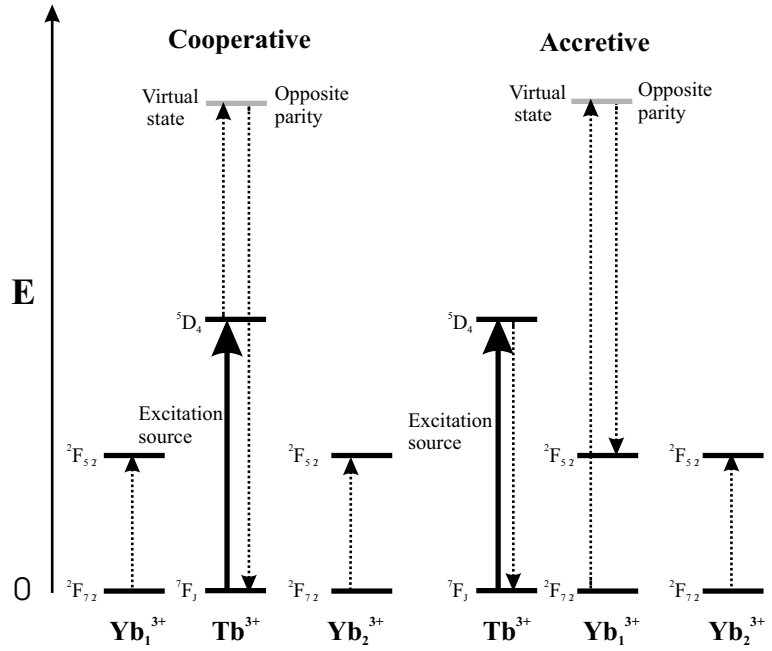

Figure 6.1: Schematic representation of the cooperative and accretive pathways for energy transfer from Tb^{3+} to Yb^{3+}. The bold arrows indicate excitation of Tb^{3+} into the $^5D_4$ state, after which energy transfer may occur. The energy-transfer processes are depicted by the dotted lines. In both mechanisms a virtual state is involved. For the cooperative mechanism, the virtual state is located on Tb^{3+}. For the accretive mechanism, the virtual state is located on Yb^{3+}. Since the total amount of energy is unchanged after the energy transfer, the resonance condition implies that the transition energy of Tb^{3+} balances the sum of the transition energies of the Yb^{3+} ions.

means that 88 out of 100 Tb^{3+} ions each transfer their energy to two Yb^{3+} ions. This makes, in principle, a quantum efficiency of 188% possible, although this is not observed due to concentration quenching at high Yb^{3+} doping concentrations. The relatively high transfer efficiency shows the potential for Tb-Yb based quantum-cutting phosphors for increasing the energy efficiency of crystalline Si-based solar cells by downconversion of the higher-energy part of the solar spectrum.

6.2 Theory

This section reviews possible mechanisms for energy transfer, with emphasis on the interion distance and orientation dependence. For three energy-transfer mecha-

nisms, the cooperative, accretive [16, 27], and the phonon-assisted [26] mechanism, energy-transfer rates will be obtained that are used to compute ensemble averaged decay curves for the donor luminescence in the Monte Carlo simulations and in the analytical solutions. It is assumed that transition-dipole moments are independent of orientation. For the second-order energy-transfer processes, this results in a minor dependence of the transfer rate to the interion orientation (as defined by the angle θ in figure 6.2).

Auzel [16] mentions two mechanisms for second-order energy transfer: a cooperative and an accretive mechanism (see figure 6.1). After excitation of the donor (Tb^{3+} $^7F_6 \rightarrow {}^5D_4$), both mechanisms require polarization induced via a virtual state of opposite parity. For the cooperative pathway, the virtual state is located on the donor (Tb^{3+}) ion and this ion acts twice as a donor of energy. For the accretive pathway, the virtual state is located on one of the acceptor (Yb^{3+}) ions. The latter accepts energy from the donor ion, after which part of the energy is transferred to the second acceptor ion.

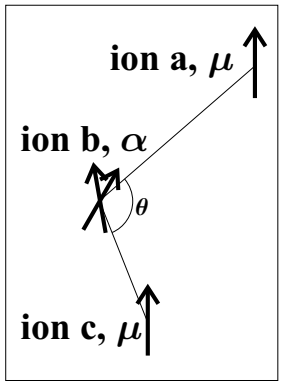

Figure 6.2: Orientational dependence of three-ion energy transfer. The arrows denote transition dipole moments $\boldsymbol{\mu}$. Since the matrix $\boldsymbol{\alpha}$ (equation 6.3) consists of products of two transition dipole moments it is denoted by two arrows. The three-body energy-transfer rate, viz. equation (6.6), shows a weak dependence on the angle θ between the lines connecting ion-pairs ab and bc.

For both of these mechanisms, Andrews & Jenkins [27] have calculated the matrix element M needed as input in Fermi's golden rule to determine the energy-transfer rate,

$$\gamma_{tr} \;=\; \frac{2\pi}{\hbar}|M|^2\rho. \tag{6.1}$$

For a specific pathway , M has the form

$$M \;=\; \boldsymbol{\mu}^a \cdot \mathbf{V}^{ab} \cdot \; \boldsymbol{\alpha}^b \cdot \mathbf{V}^{bc} \cdot \boldsymbol{\mu}^c. \tag{6.2}$$

Here, the superscripts denote the ions involved (see figure 6.2). For the cooperative process, *a* and *c* denote Yb^{3+} ions and *b* denotes a Tb^{3+} ion. For an accretive process, *a* denotes a Tb^{3+} ion and *b* and *c* denote Yb^{3+} ions. The vector $\boldsymbol{\mu}^k$ is the transition-dipole moment for a transition on ion *k* and $\boldsymbol{\alpha}^b$ is the two-photon interaction tensor, describing the transition on ion *b* , via a virtual state. The element *ij* of $\boldsymbol{\alpha}^b$ is given by

$$\alpha_{ij}^{b}(\mp\omega_a, \mp\omega_c) \;=\; \sum_{\zeta}\left(\frac{\mu_i^{2\zeta b}\mu_j^{\zeta 1b}}{E_{\zeta 1}\pm\hbar\omega_a}+\frac{\mu_i^{\zeta 1b}\mu_j^{2\zeta b}}{E_{\zeta 1}\pm\hbar\omega_c}\right), \tag{6.3}$$

where the $\mp$ are chosen with respect to the flow of energy in the system [27] and *i* and *j* denote the x, y, or z direction. The angular frequencies for the transitions on ions *a* and *c* are given by ω_a and ω_c , respectively. The sum runs over all virtual states ζ of ion *b*. The indices 1 and 2, respectively, denote the initial and the final state of ion *b*. $E_{\zeta 1}$ is the energy of the virtual state with respect to the initial state. When including line broadening due to the finite lifetimes, $E_{\zeta 1}$ should be treated as a complex quantity. However, the angular frequencies of transitions to opposite parity states on Tb^{3+} or Yb^{3+} are typically 10^{16} rad/s (in the UV spectral region), so that line broadening is small for lifetimes larger than 10^{-15} s. Therefore, we treat $E_{\zeta 1}$ as a real quantity.

The second-rank tensor $\mathbf{V}^{ab}$ contains the distance and the interion orientation dependence. In our analysis, the elements *ij* of $\mathbf{V}^{ab}$ have been simplified to the Förster analogy. This is justified for interion distances *r* much shorter than the wavelength of light ($r \ll 2\pi c/n\omega$, with *n* the refractive index of the material and ω the angular frequency associated with the energy of the transition). This leads to

$$V_{ij}^{ab} \;=\; \frac{1}{n^2}\left(\frac{n^2+2}{3}\right)^2\frac{1}{4\pi\epsilon_0 r_{ab}^3}v_{ij}^{ab}, \tag{6.4}$$

where r_{ab} is the distance between ions *a* and *b*, and v_{ij}^{ab} is the matrix element $\delta_{ij}-\hat{r}_i\hat{r}_j$. The quantities $\hat{r}_i$ and $\hat{r}_j$ are the x, y, or z components of the unit vector connecting the two ions.

In equation (6.1), $|M|^2$ consists of contributions from cooperative processes, accretive processes and mixtures of the two. Given the nature of the interacting ions, either the cooperative or the accretive process is expected to dominate. In order to obtain the transfer rate for these processes, three assumptions are made. First, all ions of the same species are assumed to be energetically equivalent, i.e., line shapes are homogeneously broadened. This allows for a separation of the spatial dependence from the spectral part. For the cooperative process this leads to

$$\gamma_{\text{coop}} \;=\; \frac{2\pi}{\hbar}\frac{1}{n^8}\left(\frac{n^2+2}{3}\right)^8\frac{\rho}{(4\pi\epsilon_0)^4}\sum_a\sum_{c>a}\frac{\left|\boldsymbol{\mu}^a\cdot\mathbf{v}^{a\text{Tb}}\cdot\boldsymbol{\alpha}^{\text{Tb}}\cdot\mathbf{v}^{\text{Tb}c}\cdot\boldsymbol{\mu}^c\right|^2}{r_{a\text{Tb}}^6 r_{\text{Tb}c}^6}. \tag{6.5}$$

Here, *a* and *c* run over all Yb^{3+} positions in the lattice. Second, in the analysis of first-order energy transfer the transition dipole moments are often treated as randomly oriented [28]. In analogy, we will do this for the dipole moments in equation (6.5). However, we treat the products of dipole moments in $\boldsymbol{\alpha}^b$ (equation 6.3) as fully correlated since a virtual state ζ couples the dipole-moment pair. Transitions involving different virtual states ζ are treated as uncorrelated, since the (4f configuration) levels 1 and 2 contain many different M_J's which couple to different ζ . Third, we assume that the transitions to and from virtual states are also uncorrelated with respect to their transition frequency.

The three assumptions above allow one to average over all orientations of the transition-dipole moments. We will perform the orientational averaging assuming classical angular distributions of the transition dipole moments. Relying on the quantum mechanical analogue would involve summing over all virtual states explicitly and taking all substates $|J, M_J\rangle$ of the levels involved on the Tb^{3+} and the Yb^{3+} ions into account. This entails a tremendous effort and is beyond the scope of this work.

After substitution of $\boldsymbol{\alpha}^{\mathrm{Tb}}$ by equation (6.3) one obtains for the orientational average,

$$\left\langle \left| \boldsymbol{\mu}^a \cdot \mathbf{v}^{a\mathrm{Tb}} \cdot \boldsymbol{\alpha}^{\mathrm{Tb}} \cdot \mathbf{v}^{\mathrm{Tb}c} \cdot \boldsymbol{\mu}^c \right|^2 \right\rangle \; = \\ \frac{4}{9}(3+\cos 2\theta) \sum_{\zeta} \left[\left(\mu^a \mu^{2\zeta\mathrm{Tb}} \mu^{\zeta 1\mathrm{Tb}} \mu^c \right)^2 \left(\frac{1}{E_{\zeta 1} \pm \hbar\omega_a} + \frac{1}{E_{\zeta 1} \pm \hbar\omega_c} \right)^2 \right], \quad (6.6)$$

where $\langle\ \rangle$ means orientational averaging over all dipole moments. The average depends on the angle θ between the pairs ab and bc (see figure 6.2). The contribution of the angular dependent part is at maximum 25% (for $\theta = 180°$). A summation over different triples lowers the angular dependant contribution. Therefore, in the Monte Carlo simulations we neglect the angular dependence and approximate the cooperative energy-transfer rate by

$$\gamma_{\mathrm{coop}} \; = \; C_{\mathrm{coop}} \sum_a \sum_{c>a} \frac{1}{r^6_{a\mathrm{Tb}} r^6_{\mathrm{Tb}c}}, \quad (6.7)$$

which is independent of θ . The constant C_{coop} will be fitted in the Monte Carlo simulations and the analytical solutions that describe the time dependence of the donor emission intensity.

The energy-transfer rate of the accretive energy-transfer process can be treated analogously. However, since there are two accretive pathways, one where the energy is accrued at b and the other where the energy is accrued at c , the matrix element M for the accretive pathway consists of the sum of two contributions. Upon evaluation of equation (6.1) one may note that quantum interference terms vanish in the

orientational averaging. This leads to

$$\gamma_{\text{accr}} \;=\; C_{\text{accr}} \sum_b \sum_{c>b} \Big(\frac{1}{r_{b\text{Tb}}^6 r_{bc}^6} \;+\; \frac{1}{r_{c\text{Tb}}^6 r_{bc}^6} \Big), \tag{6.8}$$

where b and c run over all Yb^{3+} positions in the lattice. Again, C_{accr} will be fitted in the Monte Carlo simulations.

The third energy-transfer mechanism, phonon-assisted energy transfer, is an energy-transfer process in which the energy difference between the transition on the donor (Tb^{3+}) and the transition on the acceptor (Yb^{3+}) is dissipated by multi-phonon emission. The transfer rate $\gamma_{\text{pa}}(\Delta E)$ for a process creating phonons is given by [26]

$$\gamma_{\text{pa}}(\Delta E) \;=\; (n_{\text{ph}} + 1)^p \gamma_{\text{tr}}(\Delta E = 0) \exp(-\kappa \Delta E). \tag{6.9}$$

Here, ΔE is the energy difference between the energy of the donor and acceptor transitions, n_{ph} is the phonon occupation number, and p the minimum number of available phonons required to bridge the energy gap ΔE. The energy-transfer rate γ_{tr} is the (first-order) energy-transfer rate when energy mismatches are absent. The electron-phonon coupling is described by κ . For a dipole-dipole energy-transfer mechanism, orientational averaging over the transition dipole moments yields $2/3$, so that equation (6.9) can be written as

$$\gamma_{\text{pa}} \;=\; C_{\text{pa}} \sum_a \frac{1}{r_{\text{Tb}a}^6}, \tag{6.10}$$

where the sum runs over all Yb^{3+} ions in the lattice. The parameter C_{pa} will be fitted in the Monte Carlo simulations.

6.3 Experimental

6.3.1 Sample preparation

Powder samples of $Yb_xY_{0.99-x}Tb_{0.01}PO_4$ were prepared by common solid-state methods. Stock solutions of Yb^{3+} and Y^{3+}, both containing 1% of Tb^{3+}, were prepared by dissolving rare-earth (RE) oxides in concentrated hydrochloric acid. The purity of the oxides, as labelled by the suppliers, was 4N (Y_2O_3) or 5N (Tb_4O_7 and Yb_2O_3). A solution with the desired ratio of Y^{3+} to Yb^{3+} was obtained by combining appropriate amounts of the stock solutions. The rare earth ions in the mixed solution were subsequently precipitated by adding a solution with an excess of oxalic acid. The precipitate was washed thoroughly to eliminate chloride ions. Heating the compound to 1050 °C under an oxygen atmosphere converted the oxalates to oxides. The powder obtained was mixed with diammoniumphosphate (10 mol% excess) and fired again at 1350 °C under a 1:3 H_2:N_2 atmosphere. The white powder obtained was checked for phase purity with XRD and found to be single-phase zircon

$REPO_4$. In this way, samples of $Yb_xY_{0.99-x}PO_4$:Tb^{3+} 1% were prepared with x = 0, 0.05, 0.15, 0.25, 0.50, 0.75, and 0.99.

6.3.2 Optical measurements

VIS/NIR emission and excitation measurements were performed using a SPEX DM-3000F spectrofluorometer with a 450 W Xe-lamp as the excitation source. The excitation light was dispersed by a double-grating 0.220 m SPEX 1680-monochromator (1200 l/mm) blazed at 500 nm. The light emitted by the sample was focused on a fiber guiding the light to a monochromator (150 l/mm grating, Acton Research Scientific SpectraPro, blazed at 500 nm with 0.300 m focal length) and detected using a Princeton Instruments 300i CCD camera. Tb^{3+} $^5D_4 \rightarrow {}^7F_J$ emission was rejected by the use of appropriate filters. Emission spectra were not corrected for instrumental response. Therefore, the intensity in the NIR region of the spectra is underestimated by a factor of ~ 15.

Near IR emission spectra at low temperatures were recorded by J. F. Suyver in the group of prof. H. U. Güdel, Bern (Switzerland). The powders were excited with a multimode, standing wave Ti:sapphire laser (Spectra Physics 3900S), pumped by the second harmonic of a Nd:YVO_4 laser (Spectra Physics Millennia CS-FRU). The wavelength control of the Ti:sapphire laser was achieved by an inchworm driven (Burleigh PZ-501) birefringent filter and a wavemeter (Burleigh WA2100). Sample cooling was achieved using a quartz helium-gas flow tube. The luminescence of the sample was dispersed by a 0.85 m double monochromator (SPEX 1402) with gratings blazed at 500 nm (1200 lines/mm). The signal was detected with a cooled photomultiplier tube (Hamamatsu R3310) and a photon counting system (Stanford Research SR400).

Time-resolved measurements with an excitation wavelength of 489.6 nm were performed with the use of a Lamba Physic LPD3000 tunable dye laser filled with a Coumarine 307 dye solution. It was pumped by a Lambda Physic LPX100 excimer (XeCl) laser. The typical pulse width of this setup is $\sim$ 20 ns [29]. Time-resolved measurements with an excitation wavelength of 193 nm were performed using an excimer laser (ExciStar S-200, TuiLaser) filled with an argon/fluorine gas mixture as the excitation source. The pulse duration of this laser is typically 10 ns. Emission of 544 nm was detected using a Jobin Yvon Triax 550 spectrometer (1200 l/mm, blazed at 450 nm) equipped with a Hamamatsu R928 PMT and emission around 1000 nm was detected using a 780 nm cut-off filter in combination with a Si diode. The signal was monitored as a function of time using a Tektronix 2440 digital oscilloscope. The temperature of the samples was controlled between 10 K and room temperature with an Oxford Instruments liquid-helium flow cryostat (Optistat^{CF-V}) connected to an Oxford intelligent temperature controller (ITC4).

In some cases, saturation effects occurred at short time intervals after the excitation pulse. For comparison with simulations and analytical calculations of the time

dependence of the emission intensity, the maxima of the experimentally obtained decay curves were normalized and, if necessary, the simulated curves were multiplied by ~ 1.2 in order to correct for the short-time saturation. All measurements were performed at room temperature unless mentioned otherwise.

6.3.3 Monte Carlo simulations

For several Yb^{3+} concentrations in $Yb_xY_{1-x}PO_4$:Tb^{3+} 1% the time-resolved Tb^{3+} $^5D_4 \rightarrow {}^7F_J$ luminescence was computed with the use of conventional Monte Carlo techniques [30–32]. The following scheme was used for the simulations.

First, a discrete atom model was created using the YPO_4 unit cell as input [33]. The structure of YPO_4 is tetragonal with $a = b = 6.882$ Å and $c = 6.020$ Å and four RE ions per unit cell. The RE^{3+} site has D_{2d} symmetry [34]. The size of the simulation box was 5^3 unit cells (500 RE atoms) and periodic boundary conditions were imposed. This means that all interactions up to 15.05 Åare considered. Second, the RE^{3+} lattice sites were filled randomly with Yb^{3+} or Y^{3+} by a specified Yb-to-Y ratio. Substitution of one RE^{3+} ion by Tb^{3+} generated a particular configuration.

For each configuration (i.e., distribution around the Tb^{3+} ion) its single exponential decay signal $I(t)$ is given by

$$I(t) \;=\; \exp\big[-t(\gamma_{\text{tr}} \;+\; \gamma_{\text{r}})\big], \tag{6.11}$$

where t is time, γ_{r} is the radiative decay rate of the $^5D_4$ state of Tb^{3+} in YPO_4, and γ_{tr} is the energy-transfer rate. The signal measured in an experiment consists of luminescence from an ensemble of Tb^{3+} ions. Therefore, an ensemble-averaged signal is calculated in the Monte Carlo simulations,

$$\big\langle I(t)\big\rangle \;=\; \big\langle \exp\big[-t(\gamma_{\text{tr}} \;+\; \gamma_{\text{r}})\big]\big\rangle, \tag{6.12}$$

where $\langle\,\rangle$ denotes ensemble averaging over 10 000 configurations. With this number of configurations convergence was reached.

For a particular configuration the cooperative, accretive and phonon-assisted energy-transfer rates were calculated according to

$$\gamma_{\text{tr}} = c_{\text{a}} \sum_i \sum_{j>i} \frac{1}{r_{i\text{Tb}}^{2p} r_{\text{Tb}j}^{2p}} \qquad \text{cooperative,} \tag{6.13a}$$

$$= c_{\text{b}} \sum_i \sum_{j>i} \Big(\frac{1}{r_{i\text{Tb}}^{2p} r_{ij}^{2p}} \;+\; \frac{1}{r_{j\text{Tb}}^{2p} r_{ij}^{2p}} \Big) \qquad \text{accretive,} \tag{6.13b}$$

$$= c_{\text{c}} \sum_i \frac{1}{r_{i\text{Tb}}^{2p}} \qquad \text{phonon-assisted,} \tag{6.13c}$$

where summation indices i and j refer to all Yb^{3+} ions in the lattice. The distance between ion i and j is given by r_{ij}. The two parameters in equations (6.13) are

a proportionality constant c_i and the parameter p which determines the distance dependence of the interaction. For instance, for a dipole-dipole type of interaction $p = 3$, which converts equations (6.13a), (b), and (c) into equations (6.7), (6.8) and (6.10), respectively.

Two types of simulations were performed. In the first one the distance dependence was fixed at $p = 3$. In order to study a particular energy-transfer model i , c_i was obtained by subtracting the decay rate of the Tb^{3+} luminescence in YPO_4 (γ_r) from the decay rate of the Tb^{3+} luminescence in $YbPO_4$. This gives γ_{tr}. The lattice sums in equations (6.13) are the same for all Tb^{3+} ions in $YbPO_4$. Equations (6.13) are then solved, yielding c_i. When c_i and p are known, γ_{tr} can be calculated for any configuration. Ensemble-averaged decay curves were calculated for concentrations of Yb^{3+} ranging from 15 to 99%.

A second type of simulation was used to study the distance dependence of the energy-transfer processes. Here, in order to study a particular energy-transfer model i, the values of c_i and p were varied and ensemble-averaged decay curves were computed for Yb^{3+} concentrations of 99, 75, 50, and 25%. The function H, which gives the squared deviation on a log scale for the computed curves to the experimental data, was defined to compare the simulated curves with experiments,

$$H \;=\; \sum_{x} \sum_{y(x)} \big[\ln(I_{xy}) \;-\; \ln(S_{xy})\big]^2. \tag{6.14}$$

Here, x denotes the concentration of Yb^{3+} ions and y stands for a specific data point. I and S denote the experimental and the simulated signal. Starting from an initial value of c_i and p (with a computed set of decay curves and value for H), a new guess for c_i and p resulted in a new set of decay curves and a new value for H . If this value decreased for the new c_i and p, the new parameters were approved. This iterative process was continued until convergence was reached.

6.3.4 Analytical solutions

Decay curves for the cooperative model were also calculated analytically. The procedure was the same as for the first type of Monte Carlo simulations, except that the probability distribution of the Yb^{3+} ions was calculated. For a cooperative process this is relatively straightforward since Tb^{3+} serves two times as the donor of energy. Thus, the number of Yb^{3+} ions as a function of Tb-Yb distance determines the configuration. The probability for a particular configuration P_{conf} was calculated according to

$$P_{\text{conf}} \;=\; \prod_{sh} \frac{N_{sh}!}{(N_{sh} - n_{\text{Yb}})! n_{\text{Yb}}!} c_{\text{Yb}}^{n_{\text{Yb}}} (1 - c_{\text{Yb}})^{N_{sh} \,-\, n_{\text{Yb}}}. \tag{6.15}$$

In equation (6.15) the product runs over all shells (as defined by RE-RE peaks in a radial distribution function) surrounding the Tb^{3+} ion. Product elements are elements of a binomial distribution function. c_{Yb} is the fraction of Yb^{3+} ions, N_{sh} is the

number of RE sites in the shell and n_{Yb} is the number of Yb^{3+} ions in this shell for this particular configuration.

6.4 Results and Discussion

To investigate whether energy transfer from Tb^{3+} to Yb^{3+} occurs, an emission spectrum upon excitation in the Tb^{3+} $^5D_4$ level was recorded. Figure 6.3 shows the emission spectrum of $Yb_{0.25}Y_{0.74}Tb_{0.01}PO_4$ at room temperature upon Tb^{3+} $^7F_6 \rightarrow {}^5D_4$ excitation. In the region of 500-700 nm a series of lines is observed while in the 900-1100 nm region an emission band of much lower intensity appears (multiplied 50 times in figure 6.3). The lines in the visible part of the spectrum are due to Tb^{3+} $^5D_4 \rightarrow {}^7F_J$ multiplet emissions. They are similar to previous measurements on YPO_4 doped with Tb^{3+} [35]. Transitions to different ^7F_J terms with J ranging from 5 to 0 are clearly resolved in the spectrum. The Tb^{3+} $^5D_4 \rightarrow {}^7F_6$ emission line is absent because of the use of a 540 nm cut-off filter. This filter was used to prevent second order Tb^{3+} emissions in the wavelength region of 900-1100 nm, since these emissions would obscure the detection of Yb^{3+} emission lines. The features in this part of the spectrum are attributed to the Yb^{3+} $^2F_{5/2} \rightarrow {}^2F_{7/2}$ transitions. The comparatively large linewidth of the Yb^{3+} emission is probably due to the relatively long wavelengths involved, giving larger width on a wavelength scale for the same width on an energy scale, and the strong electron-phonon coupling of Yb^{3+} ions [36], giving pronounced phonon-induced line broadening.

Compared to the Tb^{3+} emission, the intensity of the Yb^{3+} luminescence is weak. This may be due to three reasons. First, the response of the grating and the detector are not optimal in the near-infrared (NIR) region, leading to a reduced signal of a factor of ~ 15. Second, concentration quenching (the migration of excitation energy over Yb^{3+} ions to quenching sites) reduces the luminescence quantum yield for a doping concentration of 25%. Third, only a small fraction of the Yb^{3+} ions are excited. Although with 25% Yb^{3+} doping concentration two or more Yb^{3+} ions are expected to be at close range to a Tb^{3+} ion, an energy-transfer process competes with radiative depopulation of the Tb^{3+} $^5D_4$ level. To maximize the luminescence output of the Yb^{3+} ions upon excitation in the Tb^{3+} $4f^8$ levels, one has to consider competition between the energy-transfer efficiency (increasing the Yb^{3+} emission intensity for higher Yb^{3+} concentration) and concentration quenching (decreasing the Yb^{3+} luminescence intensity for higher Yb^{3+} concentration).

Excitation spectra of $Tb^{3+}$and Yb^{3+} emissions in $Yb_{0.25}Y_{0.74}Tb_{0.01}PO_4$ were recorded to give convincing evidence for the presence of $Tb^{3+} \rightarrow Yb^{3+}$ energy transfer. Figure 6.4 shows the wavelength region where the Tb^{3+} $^7F_6 \rightarrow {}^5D_4$ transition is located [37, 38]. The solid line depicts the excitation spectrum of the Tb^{3+} $^5D_4 \rightarrow {}^7F_3$ emission. The dotted line shows the excitation spectrum of the Yb^{3+} $^2F_{5/2} \rightarrow {}^2F_{7/2}$ emission. In both spectra lines are located around 485-495 nm. For the spectrum monitoring the Tb^{3+} $^5D_4 \rightarrow {}^7F_3$ emission, the excitation lines are assigned to the well-

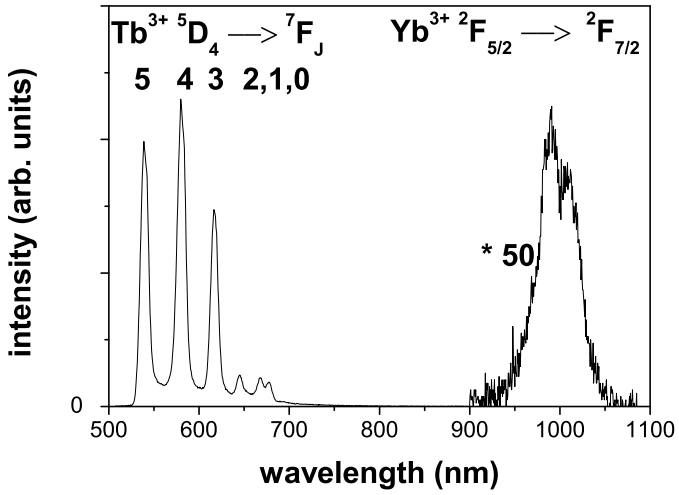

Figure 6.3: Visible and near-infrared emission spectrum of $Y_{0.74}Yb_{0.25}Tb_{0.01}PO_4$ upon Tb^{3+} $^7F_6 \rightarrow {}^5D_4$ excitation (489 nm). The spectral region between 900 and 1100 nm is amplified by a factor of 50.

known $^7F_6 \rightarrow {}^5D_4$ transitions. This absorption was also detected in previous experiments of YPO_4 doped with Tb^{3+} [35]. The excitation spectrum of the Yb^{3+} emission is very similar to the Tb^{3+} $^5D_4 \rightarrow {}^7F_3$ excitation spectrum. The observation of the Tb^{3+} $^7F_6 \rightarrow {}^5D_4$ lines in the excitation spectrum of Yb^{3+} shows that energy transfer from Tb^{3+} to Yb^{3+} is present.

Now that the occurrence of $Tb^{3+} \rightarrow Yb^{3+}$ energy transfer has been established, it is interesting to investigate the mechanism and efficiency of the energy-transfer process. The Dieke diagrams of Tb^{3+} and Yb^{3+} [37, 38] show that only a second-order energy-transfer process can occur between the Tb^{3+} $^5D_4 \rightarrow {}^7F_J$ and the Yb^{3+} $^2F_{5/2} \rightarrow {}^2F_{7/2}$ transitions. Resonant energy transfer from the $^5D_4$ state of Tb^{3+} to one Yb^{3+} ion is not possible since Yb^{3+} has only one excited multiplet ($^2F_{5/2}$) around 10 000 cm^{-1} and no transition from the Tb^{3+} $^5D_4$ level is situated at this energy. In addition, unwanted absorptions due to defect states, impurities or Yb^{3+} pair states are absent in both excitation spectra and therefore unsought resonant energy-transfer processes do not interfere. An alternative for an energy-transfer process involving two Yb^{3+} ions is mentioned in the literature as phonon-assisted energy transfer [20, 22, 23]. On the basis of emission and excitation spectra this competing process cannot be excluded. Below we will show that by analyzing transient luminescence curves phonon-assisted energy transfer can be ruled out.

In figure 6.5 the decay curves of the Tb^{3+} $^5D_4 \rightarrow {}^7F_4$ luminescence (544.0 nm) are

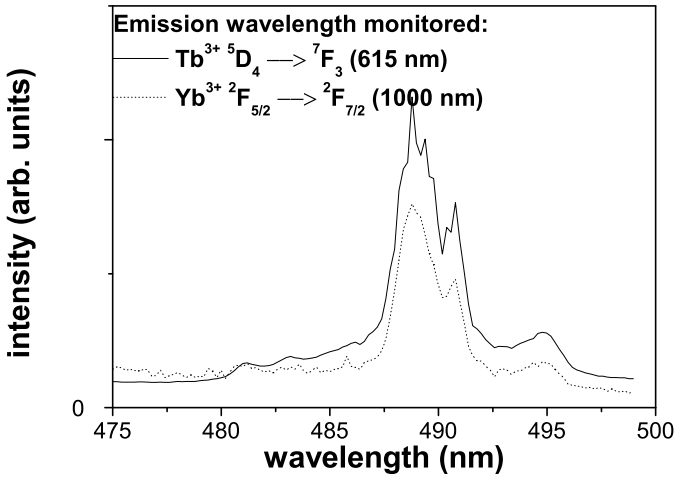

Figure 6.4: Excitation spectra of the Tb^{3+} $^5D_4 \rightarrow {}^7F_3$ emission (615 nm, solid line) and the Yb^{3+} $^2F_{5/2} \rightarrow {}^2F_{7/2}$ emission (1000 nm, dotted line) in $Y_{0.74}Yb_{0.25}Tb_{0.01}PO_4$.

plotted for Yb^{3+} concentrations of 0, 5, 15, 25, 50, 75, and 99%. The Tb^{3+} emission in YPO_4:Tb^{3+} 1% shows a nearly single-exponential decay as expected (only radiative decay). A single-exponential fit yields a decay time of 2.3 ms. A decay time between 2 and 3 ms is a typical value compared to Tb^{3+} $^5D_4$ emission in oxides where the site of Tb^{3+} lacks inversion symmetry [17,22,24,34]. When the Yb^{3+} concentration is increased, the decay curve decreases more rapidly and it becomes nonexponential. For $YbPO_4$:Tb^{3+} 1% the fastest decay is observed and the curve is again nearly single exponential. The faster decline as a function of Yb^{3+} concentration can be explained by the introduction of extra decay pathways due to the Yb^{3+}-doping: energy transfer from Tb^{3+} $^5D_4$ to Yb^{3+} enhances the Tb^{3+} $^5D_4$ decay rate. The presence of Yb^{3+} ions also explains the nonexponential behavior at intermediate doping concentrations and the single-exponential behavior for 99% Yb^{3+}. At intermediate doping concentrations the Yb^{3+} and the Y^{3+} ions are randomly distributed over the RE^{3+} lattice sites. Thus, the environment of every Tb^{3+} ion is different, leading to a variety of transfer rates. At an Yb^{3+} fraction of 99% the Tb^{3+} ions are surrounded by Yb^{3+} ions only, leading to a single decay component. Therefore, the 99% Yb^{3+} decay curve in figure 6.5 is again nearly single exponential. Fitting this curve with a single-exponential function yields a decay time of 0.25 ms.

Assuming that the radiative rate of the Tb^{3+} $^5D_4$ emission does not change when Y^{3+} is substituted for Yb^{3+}, the energy-transfer rate in $YbPO_4$ can be calculated by subtracting the Tb^{3+} $^5D_4$ radiative decay rate from the decay rate in $YbPO_4$. This

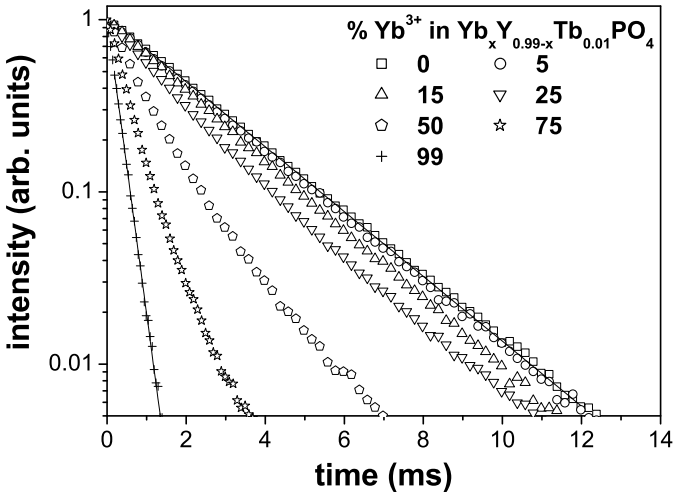

Figure 6.5: Time-resolved signals of the Tb^{3+} $^5D_4 \rightarrow {}^7F_4$ luminescence (excitation wavelength = 489.6 nm, emission wavelength = 544.0 nm) for $Yb_xY_{0.99-x}Tb_{0.01}PO_4$. Every tenth data point is shown. The different fractions x of Yb^{3+} in the $Yb_xY_{0.99-x}Tb_{0.01}PO_4$ samples are indicated in the figure. Solid lines are single-exponential fits.

results in an energy-transfer rate of 3.5×10^3 s^{-1} in $YbPO_4$:Tb^{3+} 1%. This is roughly an order of magnitude faster than the radiative decay rate of Tb^{3+} and indicates that the energy-transfer process is efficient.

Figure 6.6 shows the time-resolved Yb^{3+} luminescence for different Yb^{3+} concentrations upon excitation into the Tb^{3+} $^5D_4$ level. The Yb^{3+} luminescence shows a rise that is caused by energy transfer from Tb^{3+} to Yb^{3+}. As the Yb^{3+} concentration increases, the rise time becomes shorter. This is attributed to a faster depopulation of the Tb^{3+} donors due to the presence of more Yb^{3+} acceptors. For all samples the observed rise times are in good agreement with the decay times of the Tb^{3+} emission, confirming the feeding of the Yb^{3+} excited state by energy transfer from Tb^{3+} to Yb^{3+}. The inset shows the Yb^{3+} luminescence after excitation into the Yb-O charge-transfer (CT) band. Upon excitation in the CT state of Yb^{3+}, the $^2F_{5/2}$ state is populated directly and the lifetime of the $^2F_{5/2}$ emission can be measured without interference due to the feeding from Tb^{3+}. The Yb^{3+} luminescence of the $YbPO_4$:Tb^{3+} 1% sample shows a markedly faster decrease in intensity then the 5% doped sample: $\tau_{1/e} = 78$ μs in $YbPO_4$:Tb^{3+} 1% and 610 μs in YPO_4:Tb^{3+} 1% Yb^{3+} 5%. The short luminescence lifetime in the concentrated sample confirms the presence of strong concentration quenching. This explains the low relative intensity of the Yb^{3+} emis-

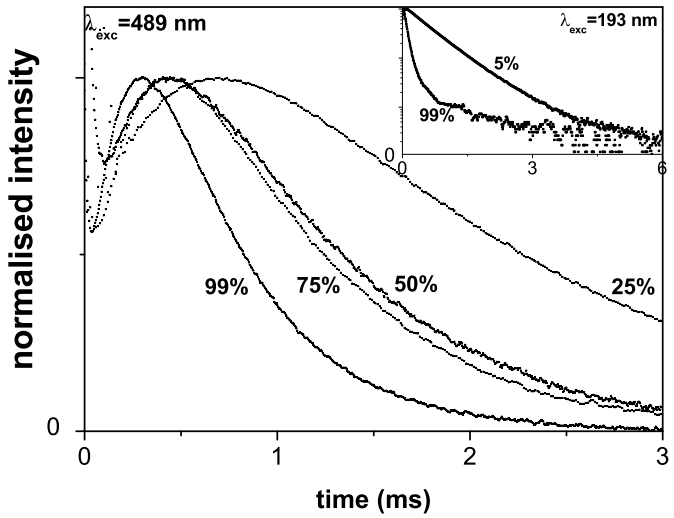

Figure 6.6: Decay curves (RT) of the Yb^{3+} $^2F_{5/2}\rightarrow{}^2F_{7/2}$ luminescence (detected with a Si diode) as a function of Yb^{3+} concentration in $Yb_xY_{0.99-x}Tb_{0.01}PO_4$. The Yb^{3+} concentrations are indicated in the figure. The Yb^{3+} luminescence monitored in the main figure is after excitation in the Tb^{3+} $^5D_4$ level (489 nm). The Yb^{3+} luminescence monitored in the inset is after excitation into the Yb-O charge-transfer band (193 nm).

sion in the luminescence spectra.

To distinguish between the three energy-transfer mechanisms (cooperative, accretive and phonon-assisted) the donor decay curves were compared to the decay behavior predicted by Monte Carlo simulations. Experiments and simulated results for the cooperative, the accretive and the phonon-assisted dipole-dipole ($p = 3$) models are shown in figure 6.7. To obtain the computed curves, the radiative decay rate and the energy-transfer rate in $YbPO_4$ (as determined from single-exponential fits to the decay curves of YPO_4 and $YbPO_4$ in figure 6.5) were used as input parameters. Therefore, at 99% Yb^{3+} concentration, the three simulated curves all match the experimental curve. However, the cooperative model matches the experiments for all Yb^{3+} concentrations while the accretive and phonon-assisted energy-transfer models deviate substantially. At all intermediate Yb^{3+} concentrations, the decay profiles of the phonon-assisted model and the accretive model fall much faster than the cooperative model. This is consistent with the distance dependence in equations (6.13). For intermediate Yb^{3+} concentrations, the phonon-assisted model yields a non-radiative decay channel for every Yb^{3+} ion present, resulting in a relatively fast

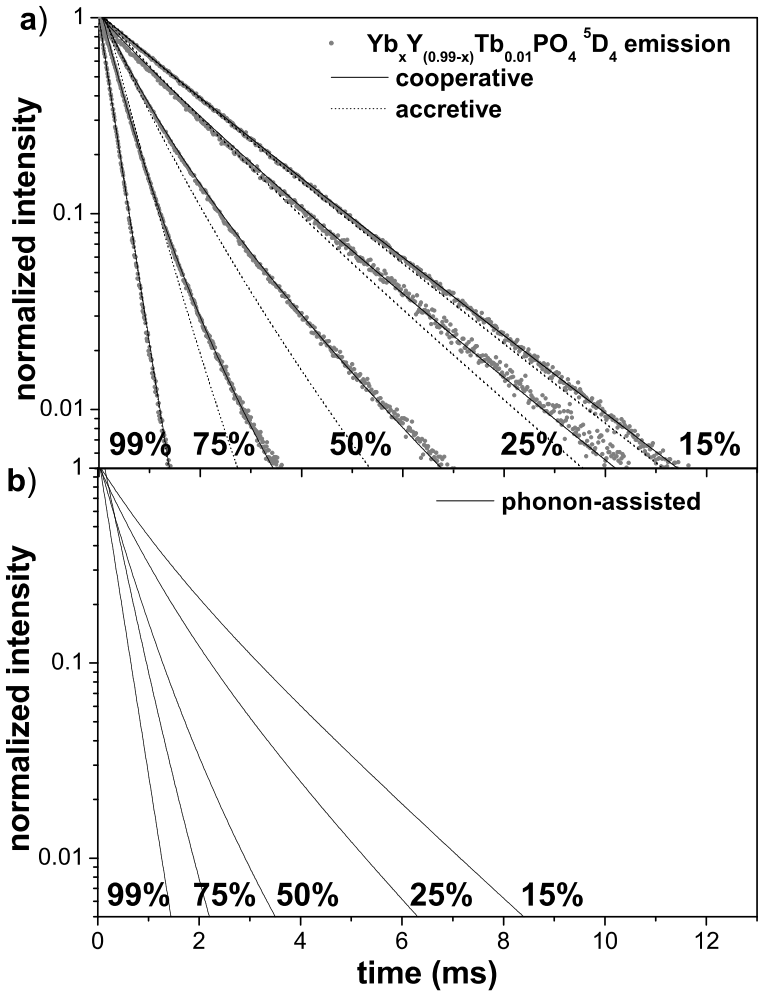

Figure 6.7: (a) Luminescence decay curves of the Tb^{3+} $^5D_4$ emission for various concentrations of Yb^{3+} (see figure 6.5) replotted with simulation results. The dots are the experimental results. The solid lines are simulated curves using a cooperative dipole-dipole model (equation 6.13a). Dotted lines are simulated curves using an accretive dipole-dipole model (equation 6.13b). (b) Simulated decay curves for the phonon-assisted dipole-dipole model (equation 6.13c). For both figures the Yb^{3+} concentrations are indicated in the figure. The single-exponential decay of the experimental data at 99% Yb^{3+} concentration is used to fit the parameter c_i) in equations (6.13).

increase of the decay rate as a function of Yb^{3+} concentration. The slowest increase of the decay rate as a function of the Yb^{3+} concentration is expected for second-order

mechanisms, since these mechanisms require two Yb^{3+} ions in close proximity to a Tb^{3+} ion. For every combination of two Yb^{3+} and one Tb^{3+}, the cooperative mechanism has one pathway where the accretive mechanism has two pathways. The relative importance of the pathways to the decay rate is not equal. The r^{-2p} distance dependence favors the shortest pathway, so that the accretive model falls faster than the cooperative model. The experimental results clearly show that energy transfer by a cooperative mechanism is the dominant process.

In our analysis the possibility of upconversion was neglected. This is justified since at doping concentrations higher than $\sim 10\%$ energy migration to the different Yb^{3+} sites will suppress the upconversion process: after energy transfer from Tb^{3+} to two Yb^{3+} ions the situation of two excited Yb^{3+} ions close to Tb^{3+} will be eliminated by fast energy migration over the Yb^{3+} ions.

The dipole-dipole nature of the energy-transfer mechanisms was tested by varying p (and c_i), i.e., by using the second type of Monte Carlo simulations described in section 6.3.3. For the cooperative model the minimum of H (equation 6.14) was reached for $p = 3.1$ and $c_a = 2.05 \times 10^9$ Å^{12}s^{-1}. This results in an energy-transfer rate to two Yb^{3+} ions at nearest-neighbor (NN) distance of 260 s^{-1}, similar to values for cooperative transfer rates reported by Basiev *et al.* [10]. The value obtained for p confirms the dipole-dipole nature of the energy-transfer mechanism. For the accretive and phonon-assisted model the value of H was much larger for any p between 2 and 5, thus ruling out those models.

We also investigated the relative contribution of the different models by fitting the decay curves ($I(t)$) at different Yb^{3+} concentrations simultaneously using

$$I(t) = (1-x-y)I_{\text{coop}}(t, c_a, p_a) + xI_{\text{accr}}(t, c_b, p_b) + yI_{\text{pa}}(t, c_c, p_c), \qquad (6.16)$$

in which x and y are the relative contribution of the accretive and phonon-assisted model. As we have fixed $p_a = 3$ for the cooperative model, our model includes seven fitting parameters ($c_a, c_b, c_c, p_b, p_c, x, y$) in which p_b and p_c could be either 3, 4, or 5. It turns out that this procedure yields $x < 10^{-3}$ and $y < 10^{-3}$, which clearly demonstrates that the cooperative mechanism is dominant.

Analytical calculations including up to eight shells (comparable to a box size of 3^3 in the Monte Carlo simulations) have been performed for the cooperative mechanism. To obtain information about the convergence distance of the energy-transfer process the transfer rate to two nearest-neighbor Yb^{3+} ions, as obtained by fitting to the decay curve of the Tb^{3+} luminescence in $YbPO_4$:Tb^{3+} 1%, is plotted as a function of included shells in figure 6.8. Here, the stars and triangles represent, respectively, the calculated and simulated energy-transfer rate to two nearest-neighbor Yb^{3+} ions when a particular number of shells is included in the calculation. The trend in the data is as expected: when few shells are included, the transfer rate to Yb-pairs is overestimated due to the neglect of the contribution to the transfer rate from longer distance Yb^{3+} ions. When more shells are included, the transfer rate levels off to the Monte Carlo result for 10^3 boxes (dashed horizontal line in figure 6.8). As is seen

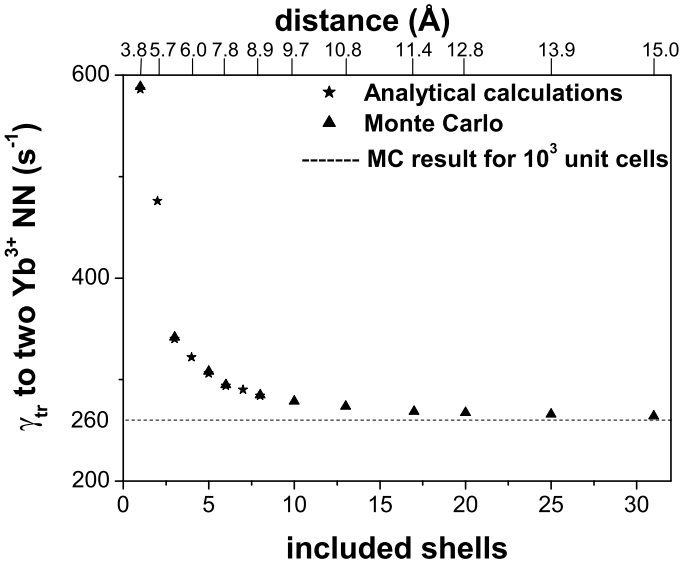

Figure 6.8: The cooperative transfer rate to two Yb^{3+} nearest neighbors (NN) as a function of the number of shells included in the simulations and calculations. The stars represent analytical calculations and the triangles depict the Monte Carlo simulations. The dashed line represents the value obtained from Monte Carlo simulations for a box size of 10^3 unit cells.

from the figure, about 90% of the transfer processes take place within a distance of eight shells (8.9 Å). A box size of 5^3 unit cells corresponds to 31 shells. At this point the energy-transfer rate has reached 265 s^{-1}, which is only 2% larger than the value for 10^3 unit cells (260 s^{-1}). The agreement between analytical calculation and simulation confirms the validity of the Monte Carlo methods.

From the luminescence decay curves in figure 6.5 the energy-transfer efficiency and the quantum efficiency can be determined. The energy-transfer efficiency $\eta_{\text{tr,x\%Yb}}$ is defined as the ratio of Tb^{3+} ions that depopulate by energy transfer to Yb^{3+} ions over the total number of Tb^{3+} ions excited. The definition for the total quantum efficiency, $\eta_{\text{x\%Yb}}$, is the ratio of the number of photons emitted (visible and infrared) to the number of photons absorbed, assuming that all excited Yb^{3+} ions decay radiatively. This assumption leads to an upper limit of the quantum efficiency. The actual quantum efficiency is lower due to concentration quenching. By dividing the integrated intensity of the decay curves of the $Yb_xY_{0.99-x}Tb_{0.01}PO_4$ samples to the integrated intensity of the YPO_4:Tb^{3+} 1% curve the transfer efficiency is obtained as

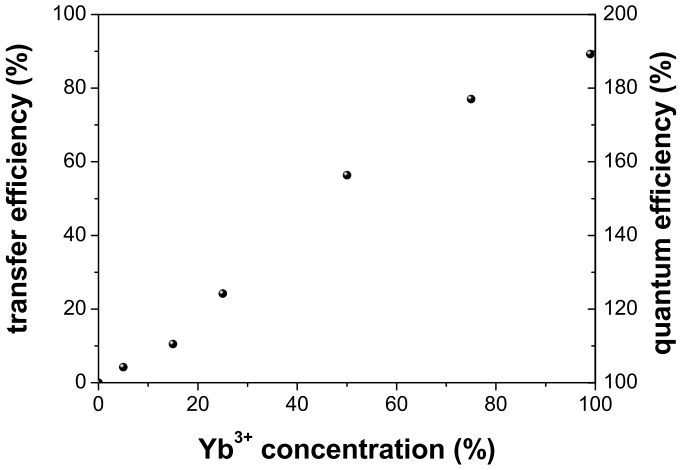

Figure 6.9: Transfer efficiency (equation 6.17) and quantum efficiency (equation 6.18) as a function of the Yb^{3+} concentration in $Yb_xY_{0.99-x}Tb_{0.01}PO_4$.

a function of the Yb^{3+} concentration,

$$\eta_{\text{tr,x\%Yb}} = 1 - \frac{\int I_{\text{x\%Yb}} \mathrm{d}t}{\int I_{\text{0\%Yb}} \mathrm{d}t}, \tag{6.17}$$

where I denotes intensity and x%Yb stands for the Yb^{3+} concentration. The relation between the transfer efficiency and the total quantum efficiency is linear and defined as

$$\eta_{\text{x\%Yb}} = \eta_{\text{rTb}}(1 - \eta_{\text{tr,x\%Yb}}) + 2\eta_{\text{tr,x\%Yb}}, \tag{6.18}$$

where the quantum efficiency for the Tb^{3+} ions, η_{rTb}, is set to 1.

In figure 6.9 the transfer efficiency and the quantum efficiency are plotted versus Yb^{3+} concentration. When the Yb^{3+} concentration is increased, the transfer efficiency shows an increase up to a maximum value of 88% in $YbPO_4$:Tb^{3+} 1%. For this sample the transfer efficiency may also be obtained using the fitted decay rates of YPO_4:Tb^{3+} 1% and $YbPO_4$:Tb^{3+} 1%, yielding the same value. For $YbPO_4$:Tb^{3+} 1% a quantum efficiency of 188% is obtained. This means that depopulation of the Tb^{3+} $^5D_4$ level proceeds 88 out of 100 times by excitation of two Yb^{3+} ions to the $^2F_{5/2}$ level. A quantum efficiency of 188% is close to the limit of 200% and comparable to the most efficient downconversion process known [1].

The relatively high energy-transfer rate may seem surprising since it involves a second-order energy-transfer process. The factors contributing to this high value are, first, the low probability of competitive processes: the excited state of the donor

has a long lifetime and first-order energy transfer is absent. Second, the cooperative transfer rate is high. According to equations (6.1)-(6.3) the atomic parameters that determine the cooperative energy-transfer rate are the transition-dipole moments of the acceptors, the transition-dipole moments of the donor, the energetic location of the virtual states and the spectral-overlap integral. The proximity (in energy) and the large transition dipole moments of the fully allowed Tb^{3+} $4f^8 \rightarrow 4f^7 5d$ transitions enhance the cooperative energy-transfer rate. Furthermore, the energetic positions of the Yb^{3+} energy levels compared to the Tb^{3+} $^5D_4$ excited state provide a good spectral overlap for second-order energy transfer.

Materials exploiting Tb-Yb cooperative quantum cutting may increase the efficiency of silicon-based solar cells by downconversion of the green-to-UV part of the solar spectrum to $\sim$ 1000 nm photons, with almost complete doubling of the number of photons. The weak IR emission of the presently studied materials (see figure 6.3) shows that, although the physics of the energy-transfer process allow for efficient quantum cutting, the experimentally obtained quantum efficiency in the IR is still low. In order to obtain a material with an actual quantum efficiency close to 200%, two drawbacks should be overcome. First, due to the high Yb^{3+} concentration needed for efficient downconversion, concentration quenching of the Yb^{3+} emission is a major issue. To overcome this problem, incorporation of ions with an excited state at slightly lower energy than the $^2F_{5/2}$ state of the Yb^{3+} ion (but still higher than the band gap of crystalline Si) may be used. These ions will function as traps for the energy in the $^2F_{5/2}$ state so that migration of excitation energy to quenching sites is suppressed. Another possibility is the use of one-dimensional systems in order to localize the energy migration and reduce concentration quenching [39–41].

The second obstacle is the low absorption cross section for green-to-UV light of Yb/YPO_4 doped with Tb^{3+}. The absorption cross section may be enhanced in two ways. First, a bulk material with a lower band gap may be used so that the host itself would absorb part of the solar spectrum, after which energy transfer to a Tb^{3+} ion should occur. Second, sensitizer ions could be used to absorb the desired part of the solar spectrum and transfer the excitation energy to the $^5D_4$ state of Tb^{3+} for the Tb-Yb downconversion process.

Lower temperatures

The temperature dependence of the energy-transfer rate provides insight in the role of phonons in the energy-transfer process. Phonons may alter the spectral overlap by temperature broadening of the transitions and may facilitate non-resonant energy transfer by bridging the energy difference. Furthermore, at low temperature sharp Yb-emission lines are expected contrary to the phonon-broadened emission bands observed at room temperature. Observation of these sharp lines at low temperature provides rigorous evidence that the emission bands observed in the 900-1100 nm spectral region at room temperature are caused by transitions on Yb^{3+}.

In figure 6.10 the energy-transfer rate of the Tb^{3+} $^5D_4 \rightarrow {}^7F_J$ to Yb^{3+} ions is plotted as a function of temperature. The points in this graph are obtained by subtraction of the Tb^{3+} $^5D_4$ radiative decay rate from the temperature dependent decay rates of the Tb^{3+} emission in $YbPO_4$:Tb^{3+} 1%. The radiative decay rate of the $^5D_4$ level of Tb^{3+} in YPO_4:Tb^{3+} 1% was found to be independent of temperature.

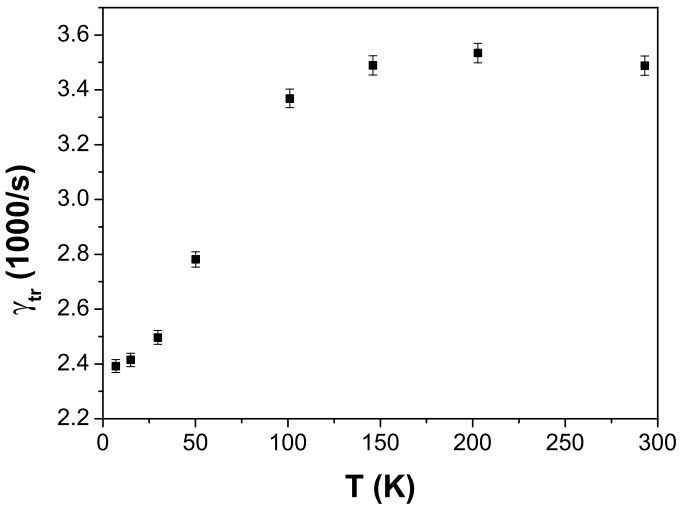

Figure 6.10: Energy-transfer rates for Tb^{3+} $^5D_4 \rightarrow {}^7F_J$ to Yb^{3+} $^2F_{7/2} \rightarrow {}^2F_{5/2}$ in $YbPO_4$:Tb^{3+} 1% as a function of temperature.

The overall trend in the graph is an increase of the energy-transfer rate with temperature from 2.4 $\times$ 10^3 s^{-1} at 10 K to 3.4 $\times$ 10^3 s^{-1} at room temperature. At the lowest temperatures (10 - 30 K) a small increase of the energy-transfer rate is observed. In the temperature range from 30 to 100 K a steeper increase is observed while for higher temperatures the energy-transfer rate levels off to a plateau starting at 150 K.

In figure 6.11 a low temperature (14 K) emission spectrum is plotted of the Yb^{3+} $^2F_{5/2} \rightarrow {}^2F_{7/2}$ emissions. In the figure, four peaks are assigned by their crystal field representations according to absorption measurements on $YbPO_4$ by Becker *et al.* [34]. The peak positions of the first two peaks (from the left) are in excellent agreement with the ones measured by Becker *et al.* The other peaks were not observed in the absorption measurements since these higher-energy $^2F_{7/2}$ Stark levels were not populated at the measuring temperature of 77 K. Compared to the calculated positions in Ref. [34] the peak positions are $\sim$ 20 cm^{-1} off.

Not only does figure 6.11 confirm the identity of Yb^{3+} as the emitter around 1000 nm, it also shows that at low temperatures the peaks are sharper than at room

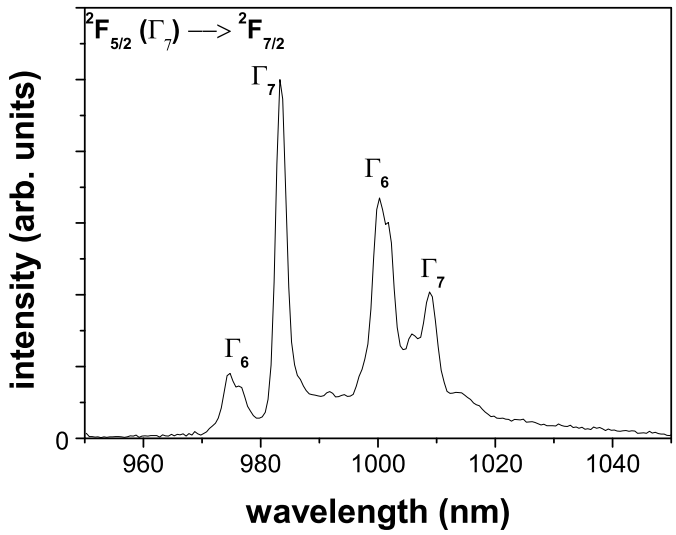

Figure 6.11: Low-temperature emission spectrum (14 K, λ_x = 488 nm) of the Yb^{3+} emissions in $Yb_{0.25}Y_{0.75}PO_4$:Tb^{3+} 1%.

temperature. Temperature broadening of the emissions of Yb^{3+} and the absorptions of Tb^{3+} may explain the observed increase of the energy-transfer rate with temperature by increasing the value of the spectral overlap integral. Another explanation is the thermal population of higher-energy Stark levels at elevated temperatures. Thermal population of these Stark levels would shift the Tb^{3+} emissions to higher energies and the Yb^{3+} absorptions to lower energies, which may improve the spectral overlap. Also phonon-assisted energy-transfer processes could play a role in the enhancement of the energy-transfer rate. The sharpest increase of the energy-transfer rate is observed around 50 K, which would imply an energy difference of ~ 35 cm^{-1} to be bridged by phonons.

6.5 Conclusion

In this paper experimental evidence is presented for cooperative energy transfer in $Yb_xY_{1-x}PO_4$:Tb^{3+}. Emission, excitation, and time-resolved luminescence measurements show the occurrence of energy transfer from the $^5D_4$ level of Tb^{3+} (around 20 000 cm^{-1}) to two Yb^{3+} ions, exciting both ions from the $^2F_{7/2}$ ground state to the $^2F_{5/2}$ excited state around 10 000 cm^{-1}. Monte Carlo simulations of the luminescence decay curves are a useful tool for the determination of the energy-transfer

mechanism. Under the assumption of cooperative dipole-dipole interaction, the simulated and the experimental luminescence decay curves are in excellent agreement for all Yb^{3+} concentrations. On the basis of the very poor agreement between simulation and experiment it is possible to exclude energy transfer via an accretive mechanism or a phonon-assisted energy-transfer process.

In (Y,Yb)PO_4:Tb^{3+} 1%, the cooperative energy-transfer rate to a pair of nearest-neighbor Yb^{3+} ions is 0.26 ms^{-1}. The corresponding efficiency of the quantum-cutting process is 88% in $YbPO_4$:Tb^{3+} 1%. This yields an upper limit for the quantum efficiency (VIS + IR) of 188%, but the actual quantum efficiency is strongly reduced by concentration quenching of the IR emission from Yb^{3+}. High concentrations of Yb^{3+} are needed for efficient cooperative energy transfer from Tb^{3+} to 2 Yb^{3+}. To develop a commercially interesting material, for example for photon doubling in silicon solar cells, solutions need to be found for concentration quenching of the Yb^{3+} $^2F_{5/2}\rightarrow{}^2F_{7/2}$ emission and also for the low absorption cross section of (Y,Yb)PO_4:Tb^{3+} 1% in the green-to-UV region.

A transfer efficiency of 88% is a surprisingly high number for a second-order energy-transfer process. A long lifetime of the excited state of the donor, the absence of first-order energy transfer, the energetically close location of allowed transitions on the donor and a good spectral overlap for second-order energy-transfer processes can explain this high efficiency. For other compounds which meet the these criteria, cooperative energy transfer may be used to obtain efficient quantum cutting as well.

References

[1] R. T. Wegh, H. Donker, K. D. Oskam, and A. Meijerink, Science **283**, 663 (1999).

[2] R. T. Wegh, E. V. D. van Loef, and A. Meijerink, Journal of Luminescence **90**, 111 (2000).

[3] T. Trupke, M. A. Green, and P. Wurfel, Journal of Applied Physics **92**, 1668 (2002).

[4] W. W. Piper, J. A. DeLuca, and F. S. Ham, Journal of Luminescence **8**, 344 (1974).

[5] J. L. Sommerdijk, A. Bril, and A. W. de Jager, Journal of Luminescence **9**, 288 (1974).

[6] R. Pappalardo, Journal of Luminescence **14**, 159 (1976).

[7] R. T. Wegh *et al.*, Physical Review B **56**, 13841 (1997).

[8] T. Forster, Annalen der Physik **2**, 55 (1948).

[9] D. L. Dexter, Physical Review **108**, 630 (1957).

[10] T. T. Basiev, M. E. Doroshenko, and V. V. Osiko, JETP Letters **71**, 8 (2000).

[11] T. T. Basiev *et al.*, Journal of Luminescence **94**, 349 (2001).

[12] I. T. Basieva, K. K. Pukhov, and T. T. Basiev, JETP Letters **74**, 539 (2001).

[13] L. D. Livanova, I. G. Saitkulov, and A. L. Stolov, Soviet physics - Solid state **11**, 750 (1969).

[14] J. Ostermayer, F. W. and L. G. Van Uitert, Physical Review B **[3]1**, 4208 (1970).

[15] B. M. Antipenko *et al.*, Optika i Spektroskopiya **35**, 540 (1973).

[16] F. Auzel, Journal of Luminescence **45**, 341 (1990).

[17] R. S. Brown, W. S. Brocklesby, W. L. Barnes, and J. E. Townsend, Journal of Luminescence **63**, 1 (1995).

[18] M. A. Noginov, P. Venkateswarlu, and M. Mahdi, Journal of the Optical Society of America B-Optical Physics **13**, 735 (1996).

[19] J. L. Adam, N. Duhamel-Henry, and J. Y. Allain, Journal of Non-Crystalline Solids **213 & 214**, 245 (1997).

[20] W. Strek, P. Deren, and A. Bednarkiewicz, Journal of Luminescence **87-9**, 999 (2000).

[21] G. M. Salley, R. Valiente, and H. U. Guedel, Journal of Luminescence **94**, 305 (2001).

[22] I. R. Martin *et al.*, Journal of Applied Physics **89**, 2520 (2001).

[23] W. Strek, A. Bednarkiewicz, and P. J. Deren, Journal of Luminescence **92**, 229 (2001).

[24] G. M. Salley, R. Valiente, and H. U. Gudel, Journal of Physics-Condensed Matter **14**, 5461 (2002).

[25] G. M. Salley, R. Valiente, and H. U. Gudel, Physical Review B **67**, 134111 (2003).

[26] T. Miyakawa and D. L. Dexter, Physical Review B **1**, 2961 (1970).

[27] D. L. Andrews and R. D. Jenkins, Journal of Chemical Physics **114**, 1089 (2001).

[28] B. Henderson and G. F. Imbusch, *Optical Spectroscopy of Inorganic Solids* (Clarendon Press, Oxford, 1989).

[29] C. de Mello Donega, A. Meijerink, and G. Blasse, Journal of Physics: Condensed Matter **4**, 8889 (1992).

[30] O. Barbosa-Garcia and C. W. Struck, Journal of Chemical Physics **100**, 4554 (1994).

[31] J. T. Vega-Duran *et al.*, Applied Physics Letters **76**, 2032 (2000).

[32] J. T. Vega-Duran *et al.*, Journal of Physics D: Applied Physics **34**, 3203 (2001).

[33] W. O. Milligan, D. F. Mullica, G. W. Beall, and L. A. Boatner, Inorganica Chimica Acta **60**, 39 (1982).

[34] P. C. Becker *et al.*, Journal of Chemical Physics **81**, 2872 (1984).

[35] R. C. Ropp, Journal of the Electrochemical Society **115**, 841 (1968).

[36] P. C. Becker *et al.*, Physical Review B **45**, 5027 (1992).

[37] G. H. Dieke, *Spectra and Energy Levels of Rare Earth Ions in Crystals* (Interscience, New York, 1968).

[38] G. H. Dieke and H. M. Crosswhite, Applied Optics **2**, 675 (1963).

[39] M. Buijs and G. Blasse, Journal of Luminescence **34**, 263 (1986).

[40] M. Buijs, J. I. Vree, and G. Blasse, Chemical Physics Letters **137**, 381 (1987).

[41] M. Buijs and G. Blasse, Journal of Luminescence **39**, 323 (1988).

Samenvatting

Deze samenvatting is een samenvatting voor leken. Voor mij zijn dit mensen die de natuur- en scheikunde die zij op de middelbare school hebben gehad grotendeels vergeten zijn, maar die wel nieuwsgierig zijn naar de 'werking van de natuur', of mensen die nou eindelijk wel eens willen weten wat hun (klein)zoon, vriend of neef nou in 's hemelsnaam de afgelopen vier jaar heeft uitgespookt.

Voordat ik deze samenvatting ben gaan schrijven heb ik mij afgevraagd: wat is er nou zo moeilijk aan het begrijpen van het werk dat ik gedaan heb? Misschien tot mijn schaamte moet ik toegeven dat het eigenlijk wel meevalt. De moeilijkheid zit hem vooral in het vele vakjargon en het combineren van een aantal op zichzelf simpele concepten. Hieronder heb ik een poging gedaan om met zo min mogelijk vakjargon de concepten één voor één te introduceren om vervolgens samen te vatten wat er in mijn proefschrift staat. In de hoop dat ik hierin geslaagd ben, nodig ik u uit om verder te lezen.

De volkswijsheid 'Opposites attract' is de essentie van de scheikunde. Volgens scheikundigen geldt deze uitspraak niet alleen voor mensen, maar ook voor hele kleine deeltjes: de positief geladen **protonen** en hun 'opposites', de negatief geladen **elektronen**. Protonen bevinden zich in de kern van een **atoom**, terwijl de elektronen in een vaste **baan** om de kern (op een vaste gemiddelde afstand van de kern) heen zwermen. De dagelijkse wereld die u en ik om ons heen ervaren is opgebouwd uit onvoorstelbaar veel atomen, waarbij de atomen bij elkaar blijven doordat elektronen aangetrokken worden door zowel de protonen van het 'eigen' atoom als de protonen van andere atomen.

Een elektron kan niet zomaar van baan veranderen. Als een elektron van baan verandert zodat het dichter bij de kern van het atoom komt, wordt er een vaste hoeveelheid **energie** uitgestraald. Als er sprake is van **luminescentie** wordt de energie uitgestraald in de vorm van **licht**. Licht is zichtbaar en kan dus bestaan uit alle kleuren van de regenboog. Luminescentie wordt gebruikt in apparaten die licht geven, zoals televisieschermen en tl-buizen. Op de binnenkant van het televisiescherm en de tl-buis zitten witte luminescerende poeders die energie kunnen omzetten in licht.

Het licht wordt uitgestraald als **golven** die zich vanaf het atoom door de ruimte

verspreiden, vergelijkbaar met wat er gebeurt als een steentje door een glad wateroppervlak wordt gegooid. Het atoom kan ook energie, bijvoorbeeld licht, **absorberen** in plaats van uitstralen. In dat geval komt het elektron terecht in een baan die verder van de positieve kern af ligt.

De **frequentie** van het golfpatroon (het aantal oscillaties per seconde) is een belangrijke eigenschap van het licht. Ten eerste bepaalt de frequentie de kleur van het licht. Zo is de frequentie van violet licht ongeveer 1.5 keer zo groot als de frequentie van rood licht. De andere kleuren zitten hier qua frequentie tussenin. Per definitie wordt de term licht gebruikt voor de frequenties die zichtbaar zijn met onze ogen, dus van violet tot rood. Dit is eigenlijk maar een heel beperkt deel van alle frequenties die atomen kunnen absorberen en uitstralen. Bijvoorbeeld: **ultraviolette** (UV) **straling** heeft een iets grotere frequentie dan blauw licht (tot zo'n 2 keer zo groot). Straling met een frequentie kleiner dan rood licht (tot zo'n 1000 keer kleiner) wordt infrarode straling genoemd (en alle zichtbare straling wordt licht genoemd).

Voor wetenschappers heeft de frequentie nog een extra betekenis: de frequentie geeft het energieverschil aan tussen de originele baan van het elektron en zijn nieuwe baan. Door de frequentie van straling te meten kan een rijkdom aan informatie worden verkregen. Niet alleen kan men de energieverschillen tussen de elektronenbanen meten, maar bovendien zijn deze energieverschillen vaak typerend voor het soort atoom en de manier waarop het atoom zijn energie kwijt raakt.

In de praktijk wordt de straling van vele miljarden atomen tegelijk gemeten en blijkt het atoom meerdere manieren te hebben om zijn energie kwijt te raken (het elektron heeft meerdere elektronenbanen om naar toe te gaan). Als een elektron naar een nieuwe baan gaat met een energieverschil dat precies gelijk is aan de energie die het atoom kwijt kan raken, gebeurt dit door uitstraling van straling met een relatief hoge frequentie. Als het elektron eerst naar een tussenliggende baan gaat, wordt straling met een lagere frequentie uitgestraald. Het atoom heeft dan nog wat energie over, wat het bijvoorbeeld kwijt kan raken in de vorm van warmte terwijl het elektron terug gaat naar de baan met de laagste energie.

Uit het bovenstaande blijkt dat niet alleen de frequentie van belang is, maar ook de hoeveelheid atomen die stralen met die frequentie. Het meten van hoeveel straling er vrij komt bij een bepaalde frequentie geeft informatie over de energieverschillen tussen de elektronenbanen en bovendien ook over welke **overgangen** (veranderingen van baan) de voorkeur hebben. Het meten van de hoeveelheid straling ten opzichte van de frequentie van de straling wordt **spectroscopie** genoemd en is een populaire methode om informatie over een (chemisch) materiaal te krijgen. Ook in dit proefschrift is hoofdzakelijk deze onderzoeksmethode gebruikt.

Het werk in dit proefschrift gaat over twee onderwerpen die veel met elkaar te maken hebben. De ene is **vacuümultraviolet** (VUV) spectroscopie en de andere is **kwantumknippen**. De naam van het eerste onderwerp, vacuümultraviolet spectroscopie, geeft aan dat hier sprake is van spectroscopie waarbij VUV straling geabsorbeerd wordt door de stoffen die bestudeerd worden. Deze soort straling heeft

een nog hogere frequentie dan UV straling en een 2 tot 8 keer hogere frequentie dan violet licht (en dus 2 tot 8 keer meer energie). Het wordt *vacuüm*ultraviolette straling genoemd omdat het sterk wordt geabsorbeerd door zuurstof. Er is dus een omgeving zonder zuurstof (bijvoorbeeld een vacuüm) voor nodig om dit soort straling te kunnen gebruiken.

Nu kunt u zich afvragen: als dit soort straling onzichtbaar is en men moet moeilijk doen om het te kunnen gebruiken, wat heeft het dan voor nut om met behulp van VUV straling onderzoek te doen? Ten eerste: de huidige tl-buizen bevatten een klein beetje kwik. Het kwik is onmisbaar in de tl-buis. Als men de tl-buis aanzet, verdampt het kwik en de damp zet de stroom uit het stopcontact om in UV straling. Dit wordt uitgestraald naar de witte poeders op de binnenkant van de tl-buis, die de UV straling omzetten in wit licht. Dit proces heeft twee nadelen. Om te beginnen is kwik schadelijk voor het milieu. Bovendien is kwik vloeibaar bij kamertemperatuur, zodat het ongeveer een seconde duurt voordat de tl-buis gaat werken als hij wordt aangezet. In die seconde wordt het kwik verwarmd zodat er voldoende verdampt. Hierdoor kan tl-licht niet gebruikt worden in toepassingen waarin een snelle respons vereist is, zoals in remlichten of kopieermachines. Kortom: als er een redelijk alternatief is voor kwik, dan verdient dat de voorkeur in toepassingen.

Een redelijk alternatief zou het onschadelijke gas Xenon (Xe) kunnen zijn. Xe zet de stroom niet om in UV straling maar in VUV straling. Zoals hierboven aangegeven heeft VUV straling veel energie en het moet bestudeerd worden hoe deze energie efficiënt kan worden omgezet in zichtbaar licht.

Een tweede reden om VUV straling voor onderzoek te gebruiken is dat men met behulp van deze straling veel kan leren. Als VUV straling wordt geabsorbeerd door een atoom, kan dit atoom na een klein beetje energieverlies (in de vorm van warmte) nog veel energie uitstralen. Hiermee kan dan informatie worden verkregen over elektronenbanen die relatief ver van de kern af liggen (in onze experimenten heeft de straling nog steeds een frequentie die tot 3 keer groter is dan die van violet licht). Dit soort spectroscopie wordt gepresenteerd in hoofdstuk 2. Hierin wordt luminescentie gemeten vanaf de 5d-baan (een hoog-energetische elektronenbaan) naar de 4f-banen (elektronenbanen met minder energie). Op experimenteel gebied is hieraan nieuw dat de frequentie van de straling met een zeer hoge resolutie is gemeten: hele kleine verschillen in de frequentie van de straling waren nog meetbaar. Deze nauwkeurige metingen leveren veel informatie over de 5d-baan en de 4f-banen op. De metingen zijn vergeleken met een theoretisch model dat de eigenschappen van elektronen in de verschillende elektronenbanen beschrijft. De voorspellingen van het model zijn in goede overeenstemming met de metingen.

De volgende drie hoofdstukken combineren VUV spectroscopie met kwantumknippen. Omdat de frequentie (oftewel de energie) van VUV straling zo groot is, is in principe het volgende mogelijk: een atoom absorbeert de VUV straling en geeft de helft van de energie af aan een ander atoom. Beide atomen hebben nu genoeg energie om ieder één keer licht uit te stralen. Als zij dit doen is er sprake van kwan-

tumknippen: één keer absorptie van straling met een hoge frequentie wordt gevolgd door twee keer emissie van straling met een lagere frequentie. Hierbij wordt gebruik gemaakt van een koppel van atomen: het eerste atoom absorbeert de straling, het tweede neemt een gedeelte van de energie over en beiden stralen licht uit.

In hoofdstuk 3 wordt het kwantumknip mechanisme van het op dit moment bekendste koppel, Gadolinium (Gd) in combinatie met Europium (Eu), nader onderzocht. Hiervan is bekend dat absorptie van VUV straling leidt tot emissie van 2 keer rood licht. Er is ook een model opgesteld van hoe de geabsorbeerde energie wordt verdeeld voordat het rode licht wordt uitgestraald. Uit dit model blijkt dat het een tijdje (ongeveer een duizendste van een seconde) duurt voordat er 2 keer rood licht kan worden uitgestraald. In dit proefschrift is de luminescentie als functie van de tijd gemeten en het signaal vergeleken met wat het model voorspelt. Er blijkt een goede overeenstemming tussen experiment en voorspelling te zijn. Ook geeft het model aan dat bij hele lage temperaturen de energieoverdracht niet meer werkt. Uit de temperatuurafhankelijke metingen in dit proefschrift blijkt dat de energieoverdracht stopt bij temperaturen lager dan -220 °C.

In hoofdstuk 4 wordt onderzocht waarom een, op het eerste gezicht, zeer geschikt koppel van atomen niet werkt. De namen van de kandidaat atomen zijn Europium en Praseodymium (Pr). Uit de experimenten in dit proefschrift blijkt dat na absorptie van de VUV straling door Pr het elektron ver genoeg van de kern af zit om te worden overgenomen door Eu. Dit wordt in wetenschappelijke termen een 'charge transfer' genoemd. Hierbij vindt een zo grote ladingsverschuiving plaats dat alle energie verloren gaat als warmte alvorens het elektron weer terugkeert naar Pr. In de praktijk is er dus geen luminescentie vanwege de charge transfer overgang.

In hoofdstuk 5 wordt een ander koppel van atomen geprobeerd: Praseodymium in combinatie met Mangaan (Mn). Het blijkt dat na absorptie van de VUV straling door Pr helemaal geen energie wordt overgedragen aan Mn. Dat is vreemd, omdat volgens gangbare theoretische modellen verwacht wordt dat er wel energieoverdracht plaats vindt. Een definitieve verklaring is nog niet gevonden.

In het 6^{e} en laatste hoofdstuk wordt kwantumknippen geprobeerd met drie in plaats van twee atomen. Hierbij absorbeert het eerste atoom (Terbium, Tb) het licht om vervolgens alle energie te verdelen over 2 Ytterbium (Yb) atomen. Dit is een nieuwe manier van kwantumknippen, omdat hierbij alle energie van 1 atoom wordt afgegeven aan 2 atomen tegelijk, terwijl in de hiervoor beschreven systemen 1 atoom de helft van zijn energie af gaf aan 1 ander atoom. Een 1-naar-2 overdracht heeft als consequentie dat de energieoverdracht minder kansrijk is. Het is dan ook verrassend dat uit de experimenten blijkt dat 88% van de Tb atomen ieder zijn energie afgeeft aan 2 Yb atomen. Door de tijdsafhankelijkheid van het energieoverdrachtsproces te meten en te vergelijken met voorspellingen op basis van theorie is ook nog het overdrachtsmechanisme opgehelderd.

Tot slot wil ik eindigen met de vraag: Wat kan men hiervan leren?
Ten eerste is er wetenschappelijke vooruitgang geboekt. In de meeste hoofdstukken

zijn wetenschappelijke puzzels opgelost, waardoor we de natuur ietsje beter begrijpen. Zo is in hoofdstuk 4 duidelijk geworden waarom Pr en Eu geen geschikt koppel zijn voor kwantumknippen en is in hoofdstuk 6 een nieuw mechanisme voor kwantumknippen in de praktijk aangetoond. Ook is duidelijk geworden dat het heel moeilijk is om efficiënte luminescerende materialen te maken na VUV bestraling. Het is jammer, maar de tl-buis met Xe gas zal de tl-buis met kwik waarschijnlijk niet vervangen. Wel zijn er andere onderzoeksmogelijkheden naar aanleiding van dit werk. Een wetenschappelijk interessante richting is het bestuderen van andere atomen onder VUV bestraling, want er zijn er nog een aantal die licht zouden kunnen geven maar die nog niet onderzocht zijn. Aan de andere kant zou kwantumknippen ook kunnen worden toegepast om zonnecellen efficiënter te maken. In dat geval dient het kwantumknippende materiaal het UV en zichtbare gedeelte van het zonlicht om te zetten in infrarood licht. Dit houdt in dat er nieuwe koppels van atomen onderzocht moeten worden die hiervoor geschikt zijn. De conclusie is dan ook: al is dit proefschrift klaar, de wetenschap is dat nog lang niet.

Publications

This thesis is based on the following publications:

1. *Time and temperature dependence of the emissions from the quantum cutting phosphor $LiGdF_4$:Eu^{3+}*, P. Vergeer and A. Meijerink. To be submitted. *Chapter 3*.

2. *A study on the downconversion efficiency for Pr^{3+} and Mn^{2+} pairs in fluorides*, P. Vergeer, A. M. Srivastava, C. R. Ronda and A. Meijerink. To be submitted. *Chapter 5*.

3. *Quenching of Pr^{3+} $^1S_0$ emission by Eu^{3+} and Yb^{3+}*, P. Vergeer, V. Babin and A. Meijerink. Journal of Luminescence **114** (2005), 267. *Chapter 4*.

4. *$4f^n{-}^15d{\rightarrow}4f^n$ emission of Ce^{3+}, Pr^{3+}, Nd^{3+}, Er^{3+}, and Tm^{3+} in $LiYF_4$ and YPO_4*, P. S. Peijzel, P. Vergeer, A. Meijerink, M. F. Reid, L. A. Boatner and G. W. Burdick. Physical Review B **71** (2005), 45115/1. *Chapter 2*.

5. *Quantum cutting by cooperative energy transfer in $Yb_xY_{1-x}PO_4$:Tb^{3+}*, P. Vergeer, T. J. H. Vlugt, M. H. F. Kox, M. den Hertog, J. P. J. M. van der Eerden and A. Meijerink. Physical Review B **71** (2005), 14119/1. *Chapter 6*.

Other publications:

1. *The role of Pb^{2+} as a sensitizer for Gd^{3+} - Eu^{3+} downconversion couple in fluorides*, V. Babin, K. Oskam, P. Vergeer and A. Meijerink. Radiation Measurements **38** (2004), 767.

2. *A real-space analysis of colloidal crystallization in a gravitational field at a flat bottom wall*, J. P. Hoogenboom, P. Vergeer and A. van Blaaderen. Journal of Chemical Physics **119** (2003), 3371.

3. *Stacking faults in colloidal crystals grown by sedimentation*, J. P. Hoogenboom, D. Derks, P. Vergeer and A. van Blaaderen. Journal of Chemical Physics **117** (2002), 11320.

4. *1,8-Bis(dimethylamino)naphthalene bis[6-fluoro-2-(trifluoromethyl)-4-quinolinol] acetonitrile solvate*, P. Vergeer, H. Kooijman, A. M. M. Schreurs, J. Kroon and E. Grech. Acta Crystallographica C **55** (1999), 1822.

Dankwoord

Het is een cliché maar toch wil ik het een keer gezegd hebben: wetenschap doe je niet alleen. Sterker nog, zonder regelmatig werkoverleg, college, discussie, theepauze, tafelvoetbal, schouderklopjes en andere sociale interactie zou dit proefschrift er nooit gekomen zijn. Dit proefschrift beschrijft vier jaar onderzoek waar een hoop mensen in meer of mindere mate aan hebben bijgedragen. Ik wil graag van deze gelegenheid gebruik maken om die mensen te bedanken.

Allereerst wil ik mijn promotor, Andries Meijerink, bedanken voor zijn begeleiding gedurende de afgelopen vier jaar. Niet alleen je goede ideeën op wetenschappelijk gebied maar vooral ook je inzicht in wetenschappelijk schrijven hebben de kwaliteit van dit proefschrift aanzienlijk verbeterd.

Cees Ronda wil ik graag bedanken voor zijn vertrouwen in mij gedurende de afgelopen jaren. Van de ECS in Philadelphia, via de zomerschool in Erice tot het afschrijven van dit proefschrift: ik heb altijd op je kunnen bouwen. Bovendien heb je ook vele interessante colleges gegeven op het raakvlak van fundamenteel onderzoek en toepassing, waarbij duidelijk werd dat iemand uit het bedrijfsleven een gezonde wetenschappelijke interesse kan hebben. Ook wil ik Harold de Wijn bedanken voor zijn mooie colleges over vaste stof fysica voor chemici. De kracht waarmee jij de concepten uit de vaste stof fysica weet over te brengen zonder het gebruik van te veel wiskunde is een voorbeeld voor veel docenten. Je bijdrage aan hoofdstuk 6 waardeer ik ook zeer.

Thijs Vlugt wil ik hartelijk bedanken voor de fijne samenwerking die we hebben gehad, resulterend in de Monte Carlo simulaties van hoofdstuk 6, een aantal zeer gezellige etentjes en goede Madeira wijnen. Also I would like to thank our 'Hamburg-guy', Vladimir Babin. His (literally) timeless efforts to upkeep the beamline at the DESY Synchrotron are much appreciated. Helen de Waard wordt bedankt voor de bepalingen van de Mn^{2+} concentratie in hoofdstuk 5.

Ook voel ik veel dankbaarheid jegens onze technicus en zonnetje van de vakgroep: Hans Ligthart. We hebben samen heel wat lol gehad en flink gestoeid met de apparatuur. Ook Stefan Zevenhuizen is voor mij belangrijk geweest. Hij heeft mij heel wat keren uit de brand geholpen als mijn computer om onverklaarbare redenen weer eens kuren had. Nico Kuipers, Jan van Eijk en Johan Keijzer wil ik bedanken voor het verzorgen van de cryogene vloeistoffen.

Gedurende mijn promotietraject hebben heel wat studenten met mij samengewerkt. Martien, Marianne en Esther zien hun projecten terug in dit proefschrift, maar ook het werk van Daan, Maurice en Piter is voor mij heel waardevol geweest. Ik wil jullie allemaal hartelijk bedanken voor jullie inzet. Van de overige studenten wil ik Mark bedanken voor zijn hulp bij LaTeX.

Ook hoofdstuk 2 is tot stand gekomen door een samenwerking. Paul Peijzel, ik wil je bedanken voor de mooie metingen die je hebt gedaan. Jouw praktische vaardigheden en theoretische kennis zijn voor mij een bron van inspiratie geweest. Prof. Gary Burdick (Andrews University, Berrien Springs, USA) visited our group for ten weeks and added simulations of the df spectra to the project. The simultaneous efforts on the experimental and the theoretical side were very stimulating and have resulted in a nice joined publication. I would like to thank you for sharing your extensive knowledge about the parameter model with us.

Uiteraard wil ik mijn 'oude' kamergenoot en goede vriend Floris bedanken. Vier jaar lang hebben wij meer dan een kamer gedeeld. Onze vele discussies, fietstochten en 'weekeinden' zal ik nooit vergeten. Floris, ik vind je een schitterende vent. Aneliya joined as a room mate in the last half year of my PhD project. Her straight forward personality and sense of humor added to the atmosphere.

Met al mijn (ex-)sectiegenoten heb ik heel wat lunchpauzes, voetbalpraat en werkbesprekingen meegemaakt. Harold, Bert, Sven, Victor, Jan, Monika, Jeroen, Rianne, Arjan, Shuai, Peter, Karin, Fiona, Celso, John, Daniel, Rolf, Dennis, Sander, Aarnoud, Alexander, François, Jessica, Laura, Marcel, Stephen en Zeger; allen hebben jullie bijgedragen tot de goede sfeer in de groep.

Daarnaast wil ik STW en de gebruikerscommissie bedanken voor het financieren van dit onderzoek en de interesse tijdens de voortgangsbesprekingen. Dr. Bruno Smets, dr. Simone Poort, dr. Arjan Vink en dr. Theo Barenbrug: bedankt voor jullie bijdragen.

Gelukkig zijn er ook nog een aantal dierbaren naast mijn werk, die ook de nodige invloed hebben gehad op het reilen en zeilen van de afgelopen (vier) jaren. Graag wil ik hier de goede band die ik heb met mijn naaste familie onderstrepen. Robert, Brassel of Ruppie, als jij in de buurt bent voel ik me altijd fijn. Ook mijn ouders zijn voor mij een grote steun. Ik ben graag bij jullie op bezoek, hoewel dit er de laatste tijd een beetje bij in is geschoten. Als laatste wil ik mijn vrouw (het voelt nog steeds een beetje onwennig), Marjolein Broos-Vergeer, bedanken voor alle steun die zij mij de afgelopen jaren heeft gegeven. Samen maken we de reis van het leven, soms door diepe dalen en gelukkig ook over grote hoogten. Het afronden van dit proefschrift behoort voor mij zeker tot de laatste categorie. Marjolein, ik vind het geweldig om ook dit samen met jou te kunnen delen.

Curriculum Vitae

The author of this thesis was born on December 17th 1976 in Leiden, The Netherlands. In May 1995 he obtained the VWO diploma at the "Rembrandt Scholengemeenschap" in Leiden. Subsequently, he spent one year of travelling and working in Australia and New Zealand. In September 1996 he started his study in Chemistry at the University of Utrecht. He received his Propaedeutic diploma (cum laude) in August 1997 and his Master of Science degree (cum laude) in August 2001. His MSc-project was conducted both at the Physical and Colloid Chemistry Group and the Soft Condensed Matter group of the University of Utrecht and at the FOM-Institute AMOLF, under supervision of dr. Jacob Hoogenboom and prof. dr. Alfons van Blaaderen. Besides his studies, he was active in the student association of the Faculty of Chemistry, PROTON, where he was a member of the board from September 1997 to September 1998.

From November 1st 2001 he was employed as a PhD student in the Condensed Matter and Interfaces group of the Debye Institute of the University of Utrecht, under the supervision of prof. dr. Andries Meijerink. The results of his PhD-project are described in this thesis and were published in scientific journals and presented as oral presentations at a number of international conferences.

Besides performing his research tasks, he supervised four Bachelor and two Master students, assisted a practical course on analytical Chemistry for first year Chemistry students and assisted a number of high school students with their "profielwerkstuk". Also, from April 2003 to May 2005 he was a member of the PhD committee of the Debye Institute, and from September 2004 to May 2005 he was Chairman of this committee.

His spare time is spent in speed cycling and sailing (summer), speed skating and skiing (winter), cooking, and ballroom and Latin dancing.